

University of Dundee

## DOCTOR OF PHILOSOPHY

### Optimising light-sheet microscopy for high resolution live imaging of the early development of chick embryos

Bango Da Cunha Correia, Ricardo F.

*Award date:*  
2018

[Link to publication](#)

#### **General rights**

Copyright and moral rights for the publications made accessible in the public portal are retained by the authors and/or other copyright owners and it is a condition of accessing publications that users recognise and abide by the legal requirements associated with these rights.

- Users may download and print one copy of any publication from the public portal for the purpose of private study or research.
- You may not further distribute the material or use it for any profit-making activity or commercial gain
- You may freely distribute the URL identifying the publication in the public portal

#### **Take down policy**

If you believe that this document breaches copyright please contact us providing details, and we will remove access to the work immediately and investigate your claim.

Optimising light-sheet  
microscopy for high resolution  
live imaging of the early  
development of chick embryos



University  
of Dundee

Ricardo F Bango Da Cunha Correia

Thesis presented for the degree of  
Doctor of Philosophy

University of Dundee

January 2018



# Contents

<u>Contents</u>	<u>i</u>
<u>List of Figures</u>	<u>iv</u>
<u>List of Tables</u>	<u>viii</u>
<u>List of Abbreviations</u>	<u>ix</u>
<u>Acknowledgements</u>	<u>xi</u>
<u>Declaration</u>	<u>xii</u>
<u>Statement</u>	<u>xiii</u>
<u>Abstract</u>	<u>xiv</u>
<u>1. Introduction</u>	<u>1</u>
1.1. Chick embryo - gastrulation	3
1.2. Light-sheet based fluorescence microscopy	6
1.2.1. Light-sheet resolution and generation	9
1.2.2. Light-sheet confocal detection	11
1.2.3. Light-sheet Bessel beam illumination	12
1.2.4. Light-sheet 2-photon	13
<u>2. Inherited DSLM system, embryo preparation and mounting, and images post-acquisition algorithms</u>	<u>16</u>
2.1. DSLM System	16
2.2. Chick embryo preparation for imaging	17

2.3. Dictyostelium Discodeum sample preparation	21
2.4. Beads and fluorescein solutions preparation	22
2.5. Beam reflected in mirror	22
2.6. The Richardson-Lucy deconvolution	23
2.7. Embryo segmentation	23
2.8. Intensity and useful contrast metrics	24
2.9. Images post-acquisition analysis algorithms	24
2.9.1. 3D stack: chick embryo 2D surface images	24
2.9.2. 3D stack: data transformation	25
2.9.3. Sample dual scan – merging images	25
2.9.4. Particle Image Velocimetry and tissue fate maps	26
<b><u>3. DSLM for imaging of chick embryos</u></b>	<b><u>27</u></b>
3.1. System overview	27
3.2. High speed DSLM	33
3.2.1. Results	36
3.3. Dual colour DSLM	45
3.3.1. Results	49
3.4. Discussion of results	50
<b><u>4. Cell ingresson events using confocal line detection principle</u></b>	<b><u>53</u></b>
4.1. CLDM implementation	53
4.1.1. Results	56
4.2. Epiblast cell ingresson	59
4.3. Vesicles formed as part of cell ingresson event	61
4.4. Discussion of results	66
<b><u>5. DSLM – Bessel beam and 2-photon illumination modes</u></b>	<b><u>68</u></b>

5.1. Bessel beam light-sheet DSLM	68
5.1.1. Results	75
5.2. 2-photon light-sheet DSLM	82
5.2.1. Results	86
5.3. Discussion of results	92
<b>6. Dual detection - illumination DSLM</b>	<b>95</b>
6.1. Dual detection - illumination DSLM set-up and software	97
6.1.1. Results	102
6.2. Discussion of results	105
<b>7. Conclusions</b>	<b>107</b>
<b>References</b>	<b>111</b>
<b>Appendices</b>	<b>121</b>
A.1 DSLM: Light-sheet software and image software	121
A.2 DSLM: Sample position compensation to maintain in focus	126
A.3 Bessel beam generated with an SLM	129

# List of Figures

FIGURE 1.1 ILLUSTRATION REPRESENTING EMBRYONIC DEVELOPMENT AFTER FERTILISATION.....	3
FIGURE 1.2 GASTRULATION IN CHICK EMBRYO, PRIMITIVE STREAK FORMATION AND EPIBLAST CELLS INGRESSION. ....	5
FIGURE 1.3 THE BASIC CONCEPT OF LIGHT-SHEET MICROSCOPY.....	8
FIGURE 1.4 LIGHT-SHEET AND CONFOCAL MICROSCOPY SECTION IMAGES AND INTENSITY PROFILE PLOT, MEASURED AT THE IMAGE PLANE (DASHED RED LINE).....	9
FIGURE 1.5 LIGHT-SHEET RESOLUTION, THICKNESS AND DEPTH OF FOCUS. ....	10
FIGURE 1.6 AN IDEAL BESSEL BEAM WAVE EQUATION AND AN ILLUSTRATION OF THE ZEROth ORDER BESSEL BEAM PROFILE. ....	12
FIGURE 1.7 1-PHOTON AND 2-PHOTON FLUORESCENCE EMISSION DIAGRAMS. ....	13
FIGURE 2.1 INHERITED DSLM MICROSCOPE MODEL.....	16
FIGURE 2.2 CHICK EMBRYO MOUNTING FOR LIGHT-SHEET LIVE IMAGING. ....	20
FIGURE 2.3 ILLUSTRATION OF EPIBLAST AND HYPOBLAST MOUNTING FOR IMAGING.....	21
FIGURE 2.4 3D STACK DATA TRANSFORMATION.....	25
FIGURE 2.5 ILLUSTRATION OF SAMPLE TOP AND BOTTOM HALVES ARE MERGED INTO ONE.....	26
FIGURE 3.1 BRIGHT FIELD AND FLUORESCENT IMAGES OF TWO DIFFERENT TRANSGENIC CHICK EMBRYOS ACQUIRED WITH A CONVENTIONAL LIGHT MICROSCOPE AT 2.5X MAGNIFICATION. F.....	27
FIGURE 3.2 .....	28
FIGURE 3.3 ILLUSTRATIONS OF A GAUSSIAN BEAM PROFILE AND A DSLM LIGHT-SHEET GENERATION. CHICK EMBRYO AT HH6 CROSS-SECTION IMAGES, WITH THE EMBRYO SURFACE BEING ADJUSTED INTO THE LIGHT-SHEET FOCUS. ....	31
FIGURE 3.4 IMAGE ACQUISITION, STORAGE AND PROCESSING WORKFLOW. ....	32
FIGURE 3.5 CHICK EMBRYO PARTIAL SURFACE WITH A LENGTH OF 4.2MM AND A WIDTH OF 1.7 MM. ....	33
FIGURE 3.6 CHICK EMBRYO SURFACE WITH A LENGTH OF 4.8 MM AND A WIDTH OF 3.2 MM. ....	34
FIGURE 3.7 OVERVIEW OF TWO DIFFERENT SCANNING MODES FROM THE PERSPECTIVE OF THE SAMPLE. ....	35
FIGURE 3.8 EMBRYO SINGLE AND DUAL SCAN MODES. ....	36
FIGURE 3.9 EMBRYO SINGLE AND DUAL SCANS, WITH 10X MAGNIFICATION DETECTION OBJECTIVE.....	37

FIGURE 3.10 PIV APPLIED TO TWO CHICK EMBRYO SURFACES.....	38
FIGURE 3.11 EMBRYO SURFACE IMAGES ACQUIRED IN SINGLE SCAN MODE AT 40X MAGNIFICATION. A) USING STEP BY STEP STAGE MOTION. B) USING CONTINUOUS STAGE MOTION. ....	39
FIGURE 3.12 CHICK EMBRYO HYPOBLAST DEVELOPMENT IMAGED FOR MORE THAN 11 HOURS.....	40
FIGURE 3.13 CHICK EMBRYO EPIBLAST DEVELOPMENT IMAGED FOR MORE THAN 10 HOURS. ....	41
FIGURE 3.14 CHICK EMBRYO HYPOBLAST SURFACE PIV (TOP) AND EXPANSION-CONTRACTION MAPS (BOTTOM). ....	43
FIGURE 3.15 CHICK EMBRYO EPIBLAST SURFACE PIV (TOP) AND EXPANSION-CONTRACTION MAPS (BOTTOM). ....	45
FIGURE 3.16 DUAL COLOUR DSLM SET-UP. ....	46
FIGURE 3.17 SCHEME OF THE ARRANGEMENT OF THE LENSES, DICHOIC MIRROR, FILTERS AND MIRRORS INSIDE THE OPTOSPLIT II BOX.....	48
FIGURE 3.18 LIVE IMAGES FROM DICTYOSTELIUM DISCODEUM ACQUIRED IN DUAL COLOUR SEQUENTIAL MODE. ....	49
FIGURE 3.19 LIVE DICTYOSTELIUM MYOSINII AND ACTIN FLUORESCENT IMAGE, RED AND GREEN, RESPECTIVELY. RGB HORIZONTAL AND VERTICAL PROFILES PLOTTED WITHIN YELLOW AND BLUE DASHED LINES.....	50
FIGURE 4.1 SYNCHRONISATION BETWEEN THE SCANNED GAUSSIAN LASER BEAM AND THE CAMERA CHIP A) 1 ROW OF PIXELS AND B) 5 ROWS OF PIXELS EXPOSURE AND READOUT AT A TIME, DURING THE LIGHT-SHEET GENERATION.....	55
FIGURE 4.2 CHICK EMBRYO AT HH1 SURFACE (TOP) AND CROSS-SECTION (BOTTOM) IMAGES ACQUIRED, AT 10X MAGNIFICATION, WITHOUT CLDM AND WITH CLDM - 5, 10, 15, 30 AND 60 LINES OF PIXELS SYNCHRONISED WITH THE LASER BEAM SCANNING.....	57
FIGURE 4.3 CHICK EMBRYO AT DEVELOPMENTAL STAGE HH6/HH7 CROSS-SECTION IMAGES AT 10X MAGNIFICATION ACQUIRED WITHOUT AND WITH CLDM, TOP AND BOTTOM IMAGES, RESPECTIVELY. ....	58
FIGURE 4.4 CROSS-SECTION IMAGES FROM CHICK EMBRYO, AT 40X MAGNIFICATION OBJECTIVE, ACQUIRED WITHOUT AND WITH CLDM.....	59
FIGURE 4.5 CHICK EMBRYO CROSS-SECTION IMAGES OF TWO CELL INGRESSION EVENTS, IN GREEN AND RED. A) CHICK EMBRYO CROSS-SECTION WITHOUT FALSE-COLOUR OVERLAY OF TRACKED CELLS THE CELLS.....	60
FIGURE 4.6 CELL INGRESSION EVENT IMAGED OVER 99 MINUTES. ....	61



FIGURE 4.7 CONCENTRATION OF VESICLES ON TOP OF THE PRIMITIVE STREAK, VISUALISED ON THE 3D STACK	
TRANSFORMED VOLUME. ....	62
FIGURE 4.8 VESICLE BEING FORMED AS A CONSEQUENCE OF CELL INGRESSION. ....	63
FIGURE 4.9 MODEL EXPLAINING THE VESICLE FORMATION AND ORIGIN. ....	63
FIGURE 4.10 EMBRYO SURFACE AND CROSS-SECTION IMAGES DURING VESICLE FORMATION FROM EPIBLAST	
CELL.....	64
FIGURE 4.11 HH4 CHICK EMBRYO, ROSETTE GIVING RISE TO A CELL INSTEAD OF FINISHING WITH A CELL	
INGRESSION. ....	65
FIGURE 5.1 DSLM WITH GAUSSIAN AND BESSEL BEAM ILLUMINATION PATHS. ....	70
FIGURE 5.2 GAUSSIAN AND BESSEL BEAM MAXIMUM INTENSITY PROJECTIONS (MIP) OF Z STACKS TAKEN	
INSIDE A VOLUME OF BEADS, PREPARED ACCORDING TO SECTION 2.4 OF THIS DOCUMENT, (LEFT)	
AND THE BEAMS RESPECTIVE CROSS-SECTION PROFILES (RIGHT) ACQUIRED AFTER USING A MIRROR	
PLACED AT THE ILLUMINATION OBJECTIVE FOCUS. ....	73
FIGURE 5.3 GAUSSIAN, BESSEL AND BESSEL CLDM LIGHT-SHEET IMAGES (TOP) ACQUIRED AFTER USING A	
MIRROR PLACED AT THE ILLUMINATION OBJECTIVE FOCUS AND THEIR RESPECTIVE INTENSITY PROFILE	
GRAPHS (BOTTOM). ....	73
FIGURE 5.4 CHICK EMBRYO SURFACE IMAGED AT 10X MAGNIFICATION OBJECTIVE USING GAUSSIAN AND	
BESSEL LIGHT-SHEET ILLUMINATIONS, WITH AND WITHOUT CLDM, AND SURFACE SEGMENTATION	
RESULTS. ....	76
FIGURE 5.5 HH3 EMBRYO CROSS-SECTION IMAGES ACQUIRED WITH GAUSSIAN AND BESSEL ILLUMINATION	
MODES, THEIR SEGMENTATION RESULTS AND THE INTENSITY AND USEFUL CONTRAST PLOTS. ....	78
FIGURE 5.6 CROSS-SECTION IMAGES FROM A HH10 DEVELOPMENTAL STAGE EMBRYO. ....	79
FIGURE 5.7 CROSS-SECTION IMAGES FROM TWO DISTINCT REGIONS, REGION I AND REGION II, INSIDE OF A	
HH10 DEVELOPMENTAL STAGE CHICK EMBRYO .....	81
FIGURE 5.8 DSLM SET-UP, INCORPORATING TWO ILLUMINATION PATHWAYS: 1-PHOTON AND 2-PHOTON	
ILLUMINATION MODES.....	82
FIGURE 5.9 1-PHOTON AND 2-PHOTON EXCITATION BEAM PROFILES IN FLUORESCEIN SOLUTION AND	
VOLUME OF BEADS (PREPARED ACCORDING TO SECTION 2.4 OF THIS DOCUMENT), AND THEIR	
RESPECTIVE LIGHT-SHEETS ILLUMINATING A MEDIUM FILLED WITH PLASTIC BEADS (0.2 $\mu$ M). ....	85

FIGURE 5.10 CHICK EMBRYO AT DEVELOPMENTAL STAGE HH1 IMAGED WITH 1-PHOTON AND 2-PHOTON ILLUMINATION MODES, AND THEIR RESPECTIVE INTENSITY AND USEFUL CONTRAST PLOTS. ....	87
FIGURE 5.11 CHICK EMBRYO AT DEVELOPMENTAL STAGE HH4 IMAGED WITH 1-PHOTON AND 2-PHOTON ILLUMINATION MODES, AND THEIR RESPECTIVE INTENSITY AND USEFUL CONTRAST PLOTS. ....	88
FIGURE 5.12 CHICK EMBRYO AT DEVELOPMENTAL STAGE HH12 HEART CROSS-SECTION IMAGES, ACQUIRED WITH 1-PHOTON AND 2-PHOTON ILLUMINATION MODES, A) AND B), RESPECTIVELY.....	91
FIGURE 5.13 CHICK EMBRYO AT DEVELOPMENTAL STAGE HH12 NOTOCHORD CROSS-SECTION IMAGES, ACQUIRED WITH 1-PHOTON AND 2-PHOTON ILLUMINATION MODES, A) AND B) RESPECTIVELY. ....	91
FIGURE 6.1 SHADOWING EFFECT MINIMISATION WITH 2DI-DSLM. ....	96
FIGURE 6.2 2DI-DSLM MICROSCOPE OPTICAL SET-UP. ....	97
FIGURE 6.3 ILLUSTRATION OF THE 2DI-DSLM ARMS HOLDING: TUBE LENS, MIRRORS AND OBJECTIVES. ....	99
FIGURE 6.4 2DI-DSLM DEVICES TRIGGERED BY SOFTWARE, 3D STAGE AND SCANNER, AND DEVICES TRIGGERED BY HARDWARE TTL CONNECTIONS, CAMERA1 AND CAMERA2. ....	101
FIGURE 6.5 MICROSCOPE SCANNER, CAMERAS AND STAGE OPERATION DURING IMAGE ACQUISITION MODES: SIMULTANEOUS AND SEQUENTIAL, ILLUSTRATIONS A AND B RESPECTIVELY. ....	101
FIGURE 6.6 PLASTIC BEADS (PREPARED ACCORDING TO SECTION 2.4 OF THIS DOCUMENT), 0.5 $\mu$ M, CROSS-SECTION IMAGES ACQUIRED WITH 2DI-DSLM IN SIMULTANEOUS AND SEQUENTIAL MODES, A) AND B) IMAGES, RESPECTIVELY. ....	102
FIGURE 6.7 2DI-DSLM CHICK EMBRYO AT DEVELOPMENTAL STAGE HH3 SURFACE IMAGES ACQUIRED IN SEQUENTIAL ACQUISITION MODE. ....	104
FIGURE 6.8 2DI-DSLM CHICK EMBRYO AT DEVELOPMENTAL STAGE HH3 CROSS-SECTION IMAGES, ACQUIRED IN SEQUENTIAL ACQUISITION MODE. ....	105

## List of Tables

TABLE 3-1 PARTS AND DEVICES USED ON DSLM SET-UP. $\lambda$ – WAVELENGTH, F – FOCAL LENGTH, NA – NUMERICAL APERTURE, WD – WORKING DISTANCE, CW – CONTINUOUS WAVE.....	30
TABLE 4-1 CELL INGRESSION AND EMERGING EVENTS OBSERVED IN 48 CELLULAR ROSETTES, COUNTED IN 4 EMBRYOS. V, STANDS FOR A CONFIRMATION OF VESICLE PRESENCE IN THE PROCESS. NV, STANDS FOR A CONFIRMATION OF NO VESICLE PRESENCE IN THE PROCESS. ....	66
TABLE 5-1 DEVICES AND PARTS USED IN DSLM BESSEL PATHWAY, FROM FIGURE 5.1. $\lambda$ – WAVELENGTH, F – FOCAL LENGTH. ....	72
TABLE 5-2 EMBRYOS SURFACE SEGMENTATION ERRORS MANUALLY COUNTED. OS – OVER-SEGMENTATION, US – UNDER-SEGMENTATION. NA – NOT APPLICABLE. ....	76
TABLE 5-3 DEVICES AND PARTS USED IN DSLM 2-PHOTON ILLUMINATION PATHWAY, FROM FIGURE 5.8. $\lambda$ – WAVELENGTH, F – FOCAL LENGTH. ....	83
TABLE 5-4 EMBRYOS ON DEVELOPMENTAL STAGES HH1 AND HH4 SURFACE SEGMENTATION ERRORS MANUALLY COUNTED. OS – OVER-SEGMENTATION, US – UNDER-SEGMENTATION. ....	89
TABLE 6-1 DEVICES AND PARTS USED IN THE 2DI-DSLM SET-UP ILLUSTRATED IN FIGURE 6.2. ....	98

## List of Abbreviations

2D	2 Dimensional
3D	3 Dimensional
4D	4 Dimensional
AOTF	Acousto Optic Tuneable Filter
CLDM	Confocal Line Detection Mode
cm	Centimetre
DSL	Digitally Scanned laser beam Light-sheet Microscopy
EMT	Epithelial to Mesenchymal Transition
fs	Femtosecond
f- $\theta$	f-theta
FWHM	Full Width at Half Maximum
GB	Gigabytes
GFP	Green Fluorescent Protein
HH	Hamburger Hamilton developmental stage
LSFM	Light-Sheet based Fluorescence Microscopy
MHz	Megahertz
mm	Millimetre
ms	Milliseconds
nm	Nanometre
PIV	Particle Image Velocimetry
PSF	Point Spread Function
sCMOS	scientific Complementary Metal-Oxide Semiconductor
SLM	Spatial Light Modulator
SPIM	Single or Selective Plane Illumination Microscope
TB	Terabyte

TTL	Transistor-Transistor Logic
μl	Microlitre
μm	Micrometre
μsec	Microsecond

## Acknowledgements

I would like to thank Prof Kees Weijer and Dr Mike MacDonald for supervising this work, and for the opportunity they gave me to work on this project.

I want to thank Dr Antti Karjalainen, who developed the algorithms to post-process the acquired data and for his friendship during this project.

I wish to thank Dr Manli Chuai for training and teaching me how to culture and mount the embryos to perform my experiments.

I want to thank Ms Gail Singer for preparing the dictyostelium samples for me and for all her support.

I would like to thank Dr Eirini Maniou and Dr Greg Sobczyk for the excellent working environment and for all their support during the project.

I wish to thank Mr Sascha Reidt for the work we performed together on implementing Bessel beam illumination and 2-photon illumination modes.

I would like to thank my family and friends for their support.

Finally, to my wife, Joana, my daughter, Martha, and my son, Pedro, there are not enough “thank you” and words to say how grateful I am to have you in my life and for your unconditional support during this PhD project. This thesis is dedicated to you.

## Declaration

I hereby declare that this thesis is my own work and it presents my original research. It has not been submitted anywhere for any award. Whenever contributions of others are involved, every effort is made to state it clearly and references to the literature are provided.

Signed \_\_\_\_\_

Date \_\_\_\_\_

**Ricardo Filipe Bango Da Cunha Correia**

## Statement

I certify that the work reported in this thesis has been performed by Ricardo Filipe Bango da Cunha Correia and that the conditions of the relevant Ordinance and Regulations of the University of Dundee have been full filled and that he is qualified to submit the accompanying thesis in the application for the degree of Doctor of Philosophy.

Signed \_\_\_\_\_

Date 21/11/2017

**Professor Cornelis Jan Weijer, FRSE**



## Abstract

Live imaging plays a key role in the study of biological processes ranging from the sub-cellular to organism scale, and all the scales between. This requires the development and use of ever evolving innovative microscopies.

The thesis project presented in the following pages describes the further development and use of light-sheet based fluorescence microscopy (LSFM) designed and optimised for imaging the early stages of development of chick embryos. The hardware and software of this microscope were optimised for improvements in performance in data acquisition speed, allowing the complete live 3D sectioning of 4 mm large chick embryos in 2-3 minutes time intervals for periods of up to 20 hours whilst maintaining high spatial resolution. This improved imaging of almost the complete embryo allows the visualisation of the largescale epiblast and hypoblast tissue flows that occur during gastrulation, while providing enough spatial and temporal resolution to be able to detect the detailed behaviours of up to 400 000 cells. Furthermore, the microscope was enhanced to be able to measure at least two fluorophores simultaneously by incorporation of an Optosplit spectral image splitter. This allowed the analysis of two fluorophores in the sample, showing for instance the action and role of two specific proteins or a specific protein and a labelled structure such as the cell membrane, simultaneously.

Further changes on the microscope were implemented in the camera operation included the use of confocal line detection, which greatly reduced background signals and increased image contrast. This improvement allowed the detection of membranous vesicles at the apical side of the epiblast in the space between the embryo and the vitelline membrane. These vesicles were especially prominent in the region where the mesendoderm precursor cells ingress. Confocal line detection allowed closer observation of vesicles formation process,

suggesting that the vesicles were released from the apical side of the cells. This led to the hypothesis that when the cells ingress into a future mesendoderm they release these vesicles by an apical abscission process. It remains to be determined whether this is necessary for ingression and what the precise role of these vesicles in the ingression process is. Some of these questions could be resolved with deeper imaging inside the embryo, allowing the ingression process and migration of cells inside the embryo to be followed in more detail. Therefore, efforts were made to improve the imaging resolution deeper in the tissue.

The Gaussian light-sheet focus images the first 1-2 cells layers from the embryo's surface with acceptable contrast and resolution. Both focus range and penetration depth can, in principle, be increased through beam shaping techniques. Hence, a Bessel beam light-sheet was generated to investigate if it would result in improved penetration depth. The Gaussian beam was modulated into a Bessel beam using a spatial light modulator and the Bessel light-sheet illumination was combined with the confocal line detection mode of the camera. The images acquired were then deconvolved, greatly enhancing image sharpness, although at the cost of a considerably increased image processing time. Embryo surface cellular segmentation analysis showed that the deconvolved Bessel confocal and the Gaussian confocal images were the best illumination modes for Bessel and Gaussian light-sheets, respectively. Overall, embryo surface cellular segmentation was found to be better performed in Gaussian confocal images, showing less segmentation errors when compared to any of the Bessel beam illumination modes or to the Gaussian illumination without confocal line detection mode. However, the image quality deeper into the tissue was not significantly improved with any of the Bessel illumination modes. The main advantage was an extended focus that allows better imaging of curved tissue surfaces that dominate later embryonic development when the embryo starts to fold considerably.

2-photon Gaussian light-sheet illumination readily improved image sharpness at a slightly increased penetration depth. In the case of 2-photon Gaussian light-sheet illumination the main concern is caused by the high photo-damage that results in the physical degradation and death of the embryos in less than 3 hours of live imaging.

Finally, a new microscope was built to investigate whether redundant information provided by combined dual illumination and dual detection light-sheet microscopy can improve image contrast and provide better structural information of the chick embryo. The expectation is that dual illumination will not compromise the sample structure, instead it will optimise the 3D data information and posterior reconstruction, thus minimising the illumination degradation in depth. The microscope has been designed and its construction and validation have started. First proof of principle, chick embryo images have been acquired which highlight the requirement for a meticulous alignment of the microscope optical set-up. Continued work with this microscope is necessary, to reach its optimal operational state.

# 1. Introduction

Gastrulation is a key event in embryonic development of most animals. Gastrulation results in the genesis and spatial arrangement of the three germ layers: ectoderm, giving rise to the skin and nervous system; mesoderm, giving rise to the muscles and skeleton; and endoderm, giving rise to the epithelia lining, the digestive tract and contributing to associated glands. In mammals, reptiles and birds, gastrulation is triggered by the formation of the primitive streak, a furrow located in the middle of the epiblast in the early embryo, which is the site of ingression of the mesendoderm precursors. Subsequently, future endoderm and mesoderm cells move towards the streak, where they undergo an epithelial to mesenchymal transition (EMT)<sup>1</sup> and migrate away to form specific mesodermal and endodermal structures. These cell and tissue movements in the embryo are orchestrated by chemical and mechanical cellular signals<sup>1-3</sup>. Gastrulation is a key developmental process and perturbation of gastrulation will generally cause grave and detrimental consequences, compromising the embryo's development. However, the key mechanisms that control and integrate the cell and tissue movements during gastrulation are still poorly understood. The model system used is the chick embryo, which displays strong similarities to human embryos in its early development, especially gastrulation.

To study the embryonic cell-cell chemical and mechanical signalling, live images of the gastrulation process in chick embryos were collected for tens of hours. Light-Sheet based Fluorescence Microscopy (LSFM) was used to characterise and monitor all relevant cell behaviours in chick embryo development for prolonged periods of time in a quantitative manner, whilst maintaining the best resolution and lowest photo-damage<sup>4-6</sup>. The PhD project presented in the following pages is a consequence of the

demanding quest for improving LSFM images contrast and sharpness and to increase the microscope's penetration depth and depth of focus. These microscope improvements are quite challenging considering the chick embryo's low transparency, millimetric size, thickness and structural complexity. The work developed during the project led to the implementation of different light-sheet microscope set-up configurations, aimed especially on improving the image contrast, microscope depth of focus and penetration depth. These improvements allow to understand the mechanism of gastrulation on chick embryos looking at the 3D tissue dynamics, with focus to cell-cell behaviour.

The following chapters describe the worked performed during this PhD project. Chapter two describes the inherited microscope and the methods used during this project. Chapter three describes the new version of the microscope built four months after the beginning of this PhD project. This microscope increased acquisition speed, the sample dual scan imaging implementation and dual colour imaging with only one camera. Chapter four describes the implementation of camera confocal line detection mode into the DSLM microscope to improve image contrast obtained by minimising the contribution of scattered light. The fifth chapter is dedicated to the modulation of the Gaussian beam into a Bessel beam to improve the microscope imaging penetration depth and extend the focal depth, as well as the implementation of 2-photon excitation to increase penetration depth with enhanced image contrast. The fifth chapter resulted from a collaboration with Sascha Reidt, another PhD student from the University of Dundee, who contributed his knowledge of modulating Gaussian beams into Bessel beams and his development of the Deconvolution code. For the 2-photon excitation implementation into the DSLM microscope Sascha contributed, equally, on building the 2-photon illumination pathway and performing experiments on chick

embryo. The sixth chapter explores the capabilities of a dual illumination and detection DSLM microscope, built and designed to image the chick embryo. The project's final remarks and conclusions are given in the seventh chapter. The appendix provides extra descriptions and information about the DSLM microscope software and Bessel beam formed with an SLM.

## 1.1. Chick embryo - gastrulation

The chick embryo as a model system has advantages including being readily accessible, since the embryo develops outside the mother environment. Furthermore, the embryos can be removed from the egg and cultured *in vitro* up to three days under conditions that are optimised for live imaging.

After fertilisation the zygote develops on top of the yolk inside the oviduct, and before egg laying the embryo undergoes a series of rapid cleavages (Figure 1.1), forming around 50,000 cells<sup>1</sup>. The early embryo is essentially disk shaped and is composed of three regions (Figure 1.1): the outer extra-embryonic region, the area opaca; the embryonic region, the area pellucida; and a crescent shaped region sitting between area opaca and area pellucida in the posterior part of the embryo, the posterior marginal zone.

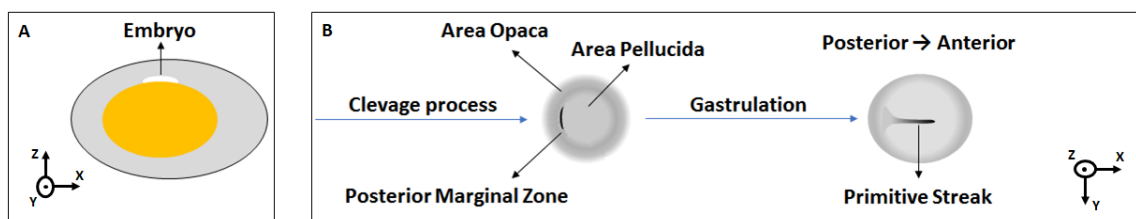


**Figure 1.1 Illustration representing embryonic development after fertilisation. A)** Inside the oviduct, the embryo sits on the top of the yolk inside the egg and the cleavage process starts. **B)** From the cleavage process three regions become evident: area opaca (extra-embryonic tissue), area pellucida (embryonic tissue) and the posterior marginal zone (slightly thickened region with small cells). Gastrulation begins upon egg laying and the primitive streak starts to form from posterior site towards the anterior end of the embryo.

Upon egg laying the embryo is a bi-layered tissue, comprising epiblast and hypoblast. The epiblast, or top layer, is made up of a one cell thick layer of epithelial cells. The bottom layer is the hypoblast and is formed from the fusion of randomly ingressing cells from the early epiblast cells and cells that migrate out from the deeper layers of the marginal zone (later giving rise to the endoblast)<sup>7</sup>. The epiblast and the yolk are protected from the egg liquid, namely albumen, by a thin membrane, the vitelline membrane<sup>8</sup>.

During the primary hypoblast formation there is an extensive cellular movement individually and in small clusters from epiblast to hypoblast. These cellular movements, depositing the primary hypoblast cells, are characterised by cellular polyingression from the epiblast, and cellular migration from the posterior marginal zone<sup>9</sup>. The hypoblast varies in appearance from scattered single cells to a sheet of cells. The hypoblast epithelialisation progresses antero-laterally by formation of intercellular contacts<sup>10</sup>. The hypoblast is a transient layer and plays an important role during primitive streak formation by secreting essential factors that are involved in the control of the primitive streak correct position and orientation during gastrulation<sup>11</sup>. For instance, a 90° angle rotation of the hypoblast relative to the epiblast results in a bent streak<sup>12</sup>. This is thought to occur through Wnt signalling by the secretion of specific inhibitors by the hypoblast that inhibit cell fate and behaviour of the cells on the overlying epiblast<sup>7,11</sup>. Hypoblast removal, before streak formation, gives rise to ectopic streaks<sup>11</sup>.

Gastrulation begins with the formation of the primitive streak (Figure 1.2) from mesoderm and endoderm precursors located in the epiblast at the posterior side of the embryo's. The primitive streak defines the organism's left and right symmetry, as well as establishing the embryo's main body midline.

Before the primitive streak formation and even before it becomes visible on the posterior site of the embryo at Hamburger Hamilton developmental stage 2 (HH2<sup>13</sup>) bilateral symmetric spiral shape flows takeover, driving the cellular movements of the epiblast which will be followed by the primitive streak formation and elongation towards the anterior site of the embryo. These movements are called the “Polonaise” pattern<sup>14</sup>. Some argue that these characteristic movements happening on the epiblast during gastrulation are explained by locally based cell-cell interactions, without the need for cells to send long distance signals to orchestrate and originate these dynamics and tissue movements<sup>15</sup>.

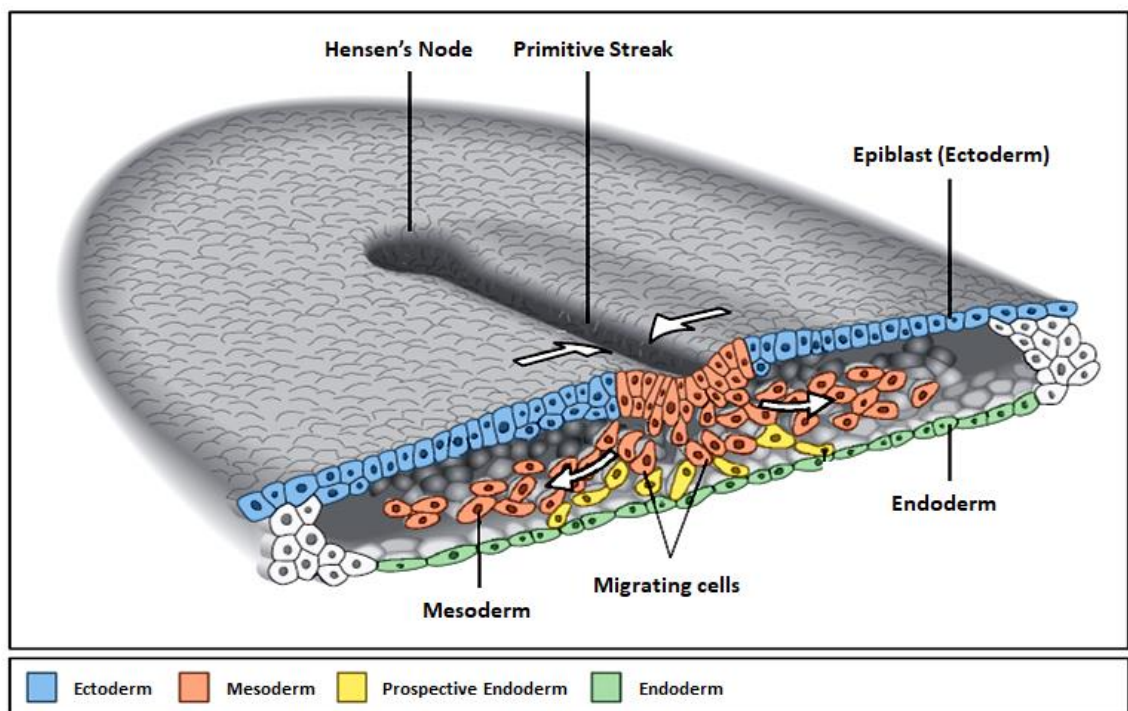


**Figure 1.2 Gastrulation in chick embryo, primitive streak formation and epiblast cells ingression.** When the primitive streak starts to form a cluster of cells is evident on the anterior tip of the streak. During gastrulation and primitive streak formation epiblast cells ingress, forming the future mesoderm and endoderm cell layers. This image is adapted from Wolpert *et al*<sup>8</sup>.

Primitive streak formation is a bi-phasic process<sup>3</sup>. The first phase results from the contraction of the tissue's mesodermal precursors in the posterior site of the embryo into a roughly triangular shape. This is followed by a second phase resulting in



an axial extension of the mesendoderm tissue along the embryo's posterior-anterior axis towards the anterior resulting in the formation of the primitive streak. The cellular processes driving these shape changes are apical contractions followed by cellular ingression of mesoderm precursors and directed cell-cell intercalations<sup>3</sup>.

When the primitive streak starts to form, the epiblast cells close to the streak start to move inwards the streak furrow and then the cells undergo an EMT process, then forming and laying at the future mesendoderm layers, Figure 1.2. The movement of cells from the epiblast towards the embryo deeper layers is denominated by cell ingression<sup>3,16</sup>. It has been observed that the formation of cellular rosettes was an important process enabling the ingression of cells inwards the streak furrow towards the embryo deeper layers<sup>17</sup>. The streak elongation is bidirectional and after reaching approximately 50% over the epiblast the mesendoderm layers are formed by the cells which have undergone EMT and are located inside the embryo deeper layers. Once the streak is about 70% extended over the epiblast at the anterior tip of the primitive streak a distinct morphological entity with a condensed cluster of cells become visible, the Hensen's node<sup>8</sup>, the organiser region of the chick embryo. The Hensen's node moves toward the posterior site of the embryo, in a process known as regression and as it continues the notochord is formed. Additionally, while the regression goes on the embryo development starts from head to tail<sup>1</sup>.

## 1.2. Light-sheet based fluorescence microscopy

In fluorescence microscopy the biological samples are labelled with fluorophores, a chemical compound responsible for the fluorescence effect, i.e. after

receiving light with a certain wavelength the fluorophore emits light with longer wavelength. Fluorophores are targeted to specific structures inside the sample. In this PhD project transgenic embryos were used, in which the cell membranes were labelled through expression of a membrane targeted GFP<sup>3</sup>. Embryos were imaged from early stages of development, starting within a few hours of development after egg laying, to the fully extended streak stage at developmental stage HH4. This required 10 to 15 hours of live imaging. At HH4 the primitive streak is completely extended and Hensen's node starts to form. This is then followed by regression of the node, while epiblast cells continue to ingress. Currently, few fluorescent imaging techniques are available to collect *in vivo* images which cause low photo-damage to the samples while still delivering high spatiotemporal sub-cellular resolution. The microscopy technique which is rapidly becoming most prominent in this area is LSFM<sup>18,19</sup>.

LSFM is a powerful imaging technique with excellent performance in long term live imaging of biological samples, while providing images with sub-cellular resolution and high spatiotemporal resolution<sup>19-29</sup>. This allows the link between tissue dynamics on the millimetre scale and cellular dynamics at the micrometre scale. There are also differences and advantages associated with using LSFM when compared to other existing microscopic techniques. For instance, in conventional microscopy the illumination and detection axes are coincident, and in confocal microscopy, due to the pinhole in front of the detector, the imaged volume, in focus, is significantly smaller than the illuminated volume. This causes photodamage and photobleaching due to unnecessary illumination. LSFM, in contrast to conventional microscopy, has orthogonal illumination and detection axes (Figure 1.3).

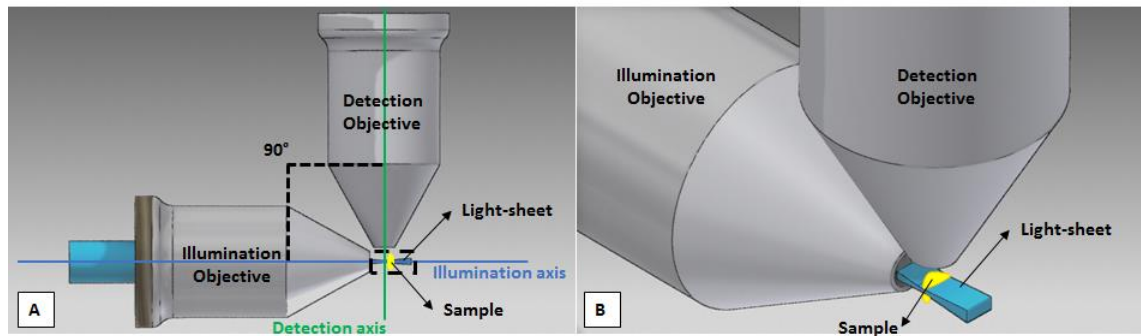


**Figure 1.3 The basic concept of light-sheet microscopy.** **A)** The two orthogonal axes for illumination and detection, with their respective objectives. **B)** The sample is sectioned by the light-sheet and the resulting fluorescence is collected by the detection objective.

In contrast to confocal microscopy, the region imaged by the LSFM corresponds to the illuminated volume. The sample is illuminated by a thin slice of light, the light-sheet, sectioning the sample. To image all the sample the images are acquired section-by-section, preserving the health of the sample, thus providing low photodamage and photobleaching<sup>4,5</sup> as only the fluorophores confined to the illuminated section are excited while the others are not illuminated. The low photodamage comes from the illumination intensity sent and absorbed by the sample in contrast to confocal microscopy, as is illustrated by the intensity plot in Figure 1.4. Therefore, with LSFM, the *in vivo* samples can be imaged for longer periods of time, from tens of hours up to days<sup>30</sup>. LSFM is a high-speed image acquisition technique since the image plane is illuminated at once, in comparison to confocal microscopy where the image plane is acquired by scanning a single point over the image plane, or spinning-disk confocal microscopy with several discrete points imaged at a time progressively covering all the image plane<sup>26</sup>, Figure 1.4. LSFM surpasses confocal microscopy for live imaging, due to its high-speed image acquisition and low photodamage.

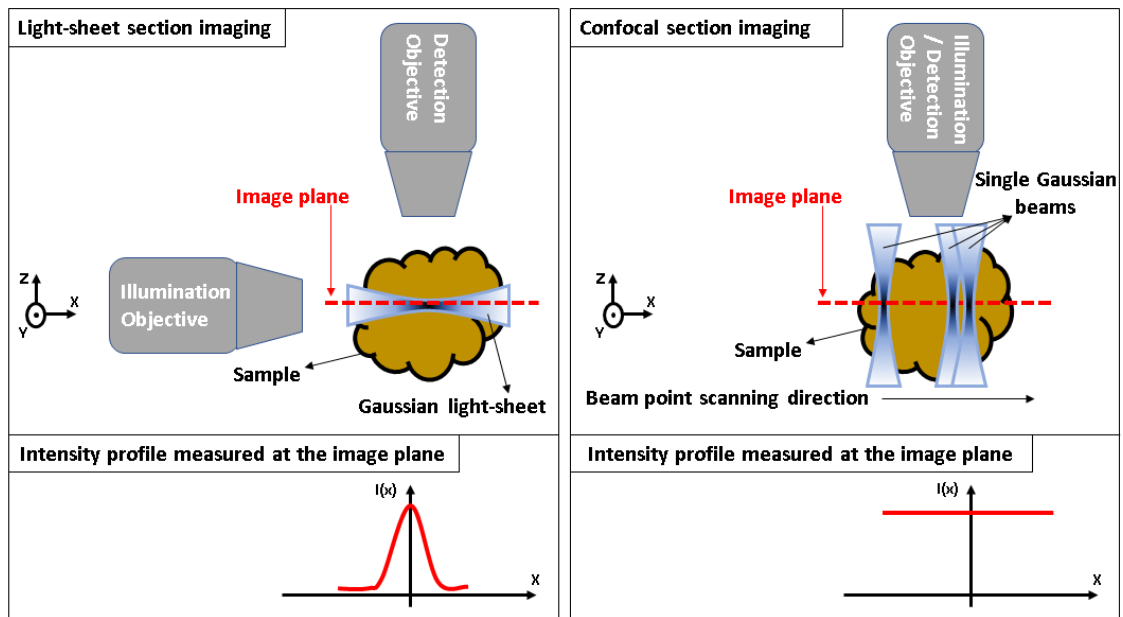


**Figure 1.4** Light-sheet and confocal microscopy section images and Intensity profile plot, measured at the image plane (dashed red line). With LSFM, a light-sheet sections the sample forming the section image. With confocal microscopy, few illumination beams are sent through the sample to create the section image.

### 1.2.1. Light-sheet resolution and generation

In LSFM, the lateral resolution is comparable to confocal and widefield microscopes<sup>4,26,31</sup>. The thickness of the light-sheet determines the axial resolution, and is mainly dependent on the characteristics of the illumination beam<sup>4,26,31</sup>. The light-sheet thickness, resolution and depth of focus are illustrated in Figure 1.5. Additionally, measuring the Gaussian beam point spread function (PSF) at the illumination focus plane allows the calculation of the Full Width at Half Maximum (FWHM) and consequently the illumination beam thickness, Figure 1.5. The microscope resolution is maximised when the back aperture of the illumination objective is filled by the beam, since the beam waist is minimised. This led to a minimised depth of focus, thus the beam spreads rapidly after the focus. If the illumination objective back aperture is not filled the axial resolution decreases, by increasing the beam waist. Then the depth of focus increases as well, Figure 1.5. Hence, there is always a trade-off between axial resolution and depth of focus to establish.

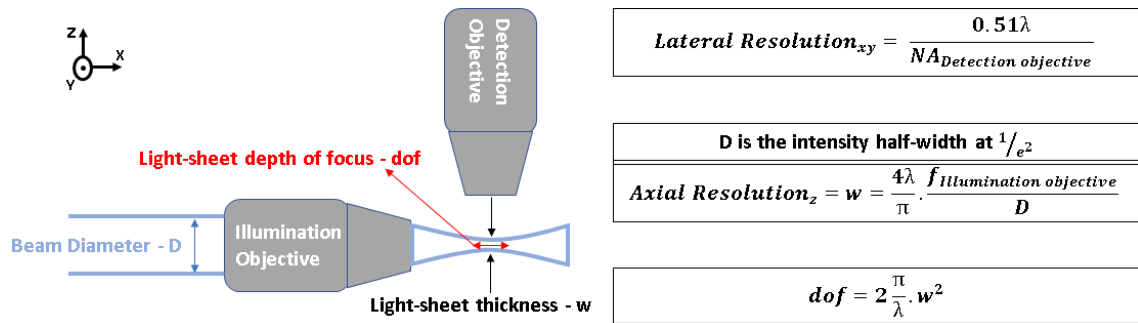


**Figure 1.5 Light-sheet resolution, thickness and depth of focus.**  $\lambda$  is the beam wavelength,  $NA_{\text{Detection objective}}$  is the numerical aperture of the detection objective and  $f_{\text{illumination objective}}$  is the focal distance of the illumination objective.

Nowadays a considerable number of distinct light-sheet based microscope setups are available for a broad range of biological samples<sup>32–36</sup>. With prominent results in live imaging of: chick embryo primitive streak formation<sup>3</sup>; *C. Elegans* embryonic and neuronal development<sup>30</sup>; *Drosophila* embryogenesis and heart tubes<sup>31,32</sup>; Zebrafish beating heart and embryonic development<sup>40,41</sup>; and mouse brain activity<sup>39</sup>. In LSM two modes are used to generate the light-sheet. In Single or Selective Plane Illumination Microscopy (SPIM)<sup>42</sup> the light-sheet is generated by a cylindrical lens. In Digital Scanned laser Light-sheet Microscopy (DSLM) the light-sheet is generated by scanning a laser beam<sup>40</sup>. The advantage of having a DSLM light-sheet instead of a SPIM light-sheet is that a DSLM light-sheet is dynamic and incoherent<sup>4,5</sup>. Using XY galvo-mirrors to form the light-sheet gives immediate control of the light-sheet extension and orientation both of which are always adjustable. Coherent light increases the presence of artifacts rising from scatter and absorption in relation to the complexity of the sample<sup>5</sup>. DSLM incoherent light minimises artifacts, enhancing image quality. Image quality, for both SPIM and DSLM, is further improved through sample rotation and/or by increasing the number of illumination and detection axes covering the three dimensional structure of the sample<sup>18,19,29,43</sup>. The choice of whether to build a SPIM or

a DSLM microscope relies mostly on the required image quality, the cost and complexity of the microscope and the sample structural complexity.

### 1.2.2. Light-sheet confocal detection

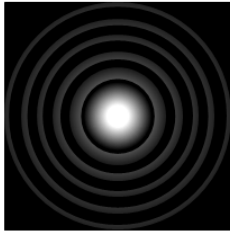
Light interacting with matter can suffer from some of the following effects: reflection, refraction, absorption and scattering. In the case of a specular surfaces, like mirrors and glass, the reflection and refraction of the incident beam light are governed by Snell's Law<sup>44</sup>. For diffuse and rough surfaces, the light incident and reflected angles are governed by Lambert's cosine law<sup>45</sup>. In LSFM the images are more affected by light absorption and scattering. For absorption light interaction mode, the illumination beam absorbed by the sample is necessary to produce the fluorescent signal, which allows the observer to follow specific structures inside the sample. The scattering effect, results from the interaction of the light with the sample and structures located inside of it due to refractive index variations. These structures will deviate the light as it travels through the sample. As a result, complex structures have more scattering agents than a quasi-transparent sample. The scattered light will increase the image's background signal, therefore affecting the image's contrast.

Like other light microscopy techniques using a Gaussian laser beam, results from LSFM are affected by scatter and limited penetration depth<sup>4,5</sup>. Scatter is unavoidable, although its contribution is minimised with a confocal detection performed by using a slit on the detection pathway of the microscope, collecting the signal only from the focus and minimising the background signal. The slit can be physically implemented on the microscope<sup>46</sup> and it can be implemented as a post-acquisition line masking over the acquired images<sup>47</sup>. Additionally, and more recently, the confocal line detection has been implemented through using the camera electronic

slit<sup>48</sup>. Using this camera confocal line detection manner has led to an increased image contrast<sup>49,50</sup>.

### 1.2.3. Light-sheet Bessel beam illumination

Recent studies have shown that beam shaping techniques resulting in the modulation of Gaussian beams into Bessel beams reduce the influence of scattering and improve penetration depth<sup>51–53</sup>. An ideal Bessel beam wave equation<sup>54,55</sup>, satisfying the Helmholtz equation, and an illustration of the zeroth order Bessel beam profile are exhibited in Figure 1.6.

Ideal Bessel beam wave equation	Zeroth order Bessel beam profile
<div style="border: 1px solid black; padding: 5px; margin-bottom: 10px; text-align: center;"> <math display="block">E(r, \phi, z) = A_0 e^{ik_z z} J_n(k_r r) e^{\pm in\phi}</math> </div> <ul style="list-style-type: none"> <li>• <math>k_z</math> and <math>k_r</math> are the longitudinal and radial wavevectors</li> <li><math>k = \sqrt{k_z^2 + k_r^2} = \frac{2\pi}{\lambda}</math>, <math>\lambda</math> is the illumination beam wavelength</li> <li>• <math>r, \phi</math> and <math>z</math> are the radial, azimuthal and longitudinal components</li> <li>• <math>J_n</math> is an n-th order Bessel function of the first kind</li> </ul>	

**Figure 1.6** An ideal Bessel beam wave equation and an illustration of the zeroth order Bessel beam profile.

Bessel beams have gone beyond the penetration depth limits of Gaussian beams<sup>56</sup>, mostly due to their extended focus<sup>51</sup> and intrinsic non-diffracting<sup>54</sup> properties. Bessel beams are formed by a conical phase front and normally described as obstruction diffracting light from its characteristics higher order rings, Figure 1.6, to fill the gap after the obstruction. An increased number of obstacles will ultimately still distort the beam profile. Hence, the effectiveness of non-diffracting beams is likely to be strongly dependent on the sample's structural complexity.

The ideal Bessel beam has infinite transverse extent and energy, thus it is practically impossible to experimentally produce a Bessel beam. However, a quasi-

Bessel beam can be generated in several ways. Some methods rely on using an annulus aperture<sup>54,55</sup>, an axicon<sup>57,58</sup> or a Spatial Light Modulator (SLM)<sup>51,56</sup>. The annulus and the axicon produce an immediate quasi-Bessel beam, with the beam characteristics of depth of focus and extension being dictated by the two optical parts specificities. For instance, a quasi-Bessel beam with the longest depth of focus and extension is achieved with the smallest annulus diameter or axicon cone angle. The SLM is as more versatile technique, since the device can be programmed with a diversity of mathematical functions to generate Bessel beams and other beams<sup>51</sup>. To modulate the Gaussian beam into a Bessel beam the SLM displays a conical phase mask. The SLM resulting modulated beam can be computed analytically or iteratively through using the Gerchberg-Saxton algorithm<sup>59</sup>.

#### 1.2.4. Light-sheet 2-photon

Image contrast and penetration depth for Gaussian laser beams can be improved with 2-photon excitation<sup>6,26,38,60,61</sup>. The 2-photon illumination is another well documented technique used to increase penetration depth and image contrast<sup>38,62</sup> in optical microscopy. In theory, in 1-photon excitation a single photon with a wavelength  $\lambda$  and intensity  $I_0$  produces one fluorescent photon, Figure 1.7 A.

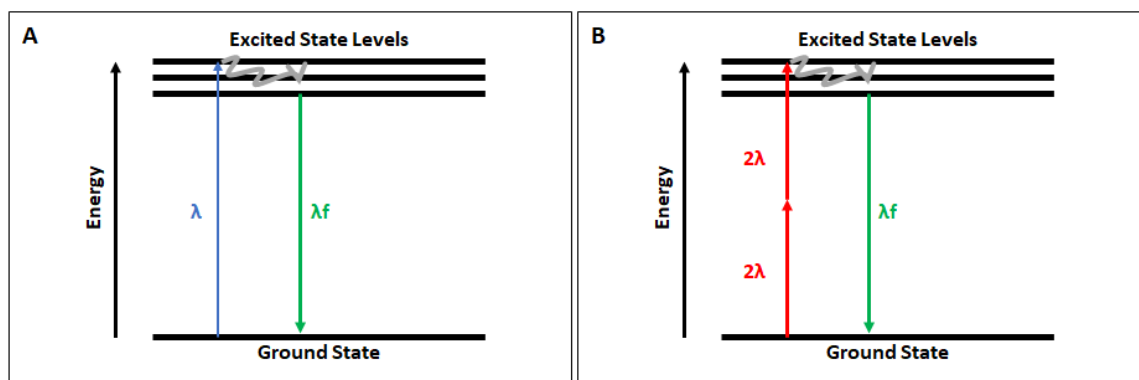


**Figure 1.7 1-photon and 2-photon fluorescence emission diagrams. A)** 1-photon of high energy with wavelength  $\lambda$  excites an electron from the ground state to higher vibrational and excited energy states and upon system relaxation with the electron returning to the ground state, it emits another photon



with higher wavelength  $\lambda$  producing fluorescence. **B)** In 2-photon fluorescence production in contrast to 1-photon the electron is excited by two consecutive photons, i.e. each photon has a wavelength of  $2\lambda$ . The time lapse between the two photons should be small enough to excite the electron before it returns to the ground state eventually producing fluorescence.

In 2-photon excitation, in theory, one photon with a wavelength of  $2\lambda$  hits an electron in ground state and before the electron returns to the ground state another photon with the same wavelength of the previous photon,  $2\lambda$ , hits the electron again sending it to higher excitation energy levels and one fluorescent photon is produced upon the return of the electron to the ground state, Figure 1.7 B. With both photons being produced by the same source with intensity  $I$ , this leads to the fluorescent signal produced scaling as  $I^2$ .

The 2-photon excitation increased penetration depth comes from the longer wavelength of the excitation light compared to 1-photon excitation. In the case of GFP the wavelength should be around the near infrared range, 920-960 nm, because long wavelengths are less affected by scattering. The high contrast comes from the 2-photon quadratic dependence since the higher fluence of photons occurs at the beam focus, i.e. all the fluorophores inside of the depth of focus will be “quadratically” enhanced establishing a stronger distinction between the in focus and out of focus regions where the beam divergence will occur quadratically, lowering substantially the chances of getting 2-photon excitation, reducing chances of out of focus background influence in the acquired images.

The generation of a 2-photon effect requires high intensity illumination of the sample (a high flux of photons), increasing the probability of getting an adequately strong fluorescent signal. It is possible to generate the 2-photon excitation with a continuous wave laser, although the fluorescent signal gained is lower by a factor of 59 000 times at the same average power with a pulse length of 220 fs and a repetition rate of 76 MHz<sup>63</sup>. As a consequence, the high energy densities produced can

compromise the sample preservation for live imaging since it increases photobleaching due to high probability of photochemical degradation in the long-lived triplet state<sup>64</sup>.

## 2. Inherited DSLM system, embryo preparation and mounting, and images post-acquisition algorithms

This chapter describes the DSLM model system prior to this PhD project, the protocol followed to prepare and mount the chick embryos for live imaging and the algorithms used for post-acquisition image processing.

### 2.1. DSLM System

On arrival at Prof Kees Weijer Lab, a DSLM model system was in place and available to use<sup>3</sup>. The microscope set-up configuration incorporated periscopes to send the laser beam into the scanner and from the scanner to the tube lens and illumination objective pair positioned on the same axis, as shown in Figure 2.1. The detection objective, the second tube lens and the camera were also positioned in the same axis, although orthogonally to the illumination objective axis Figure 2.1.

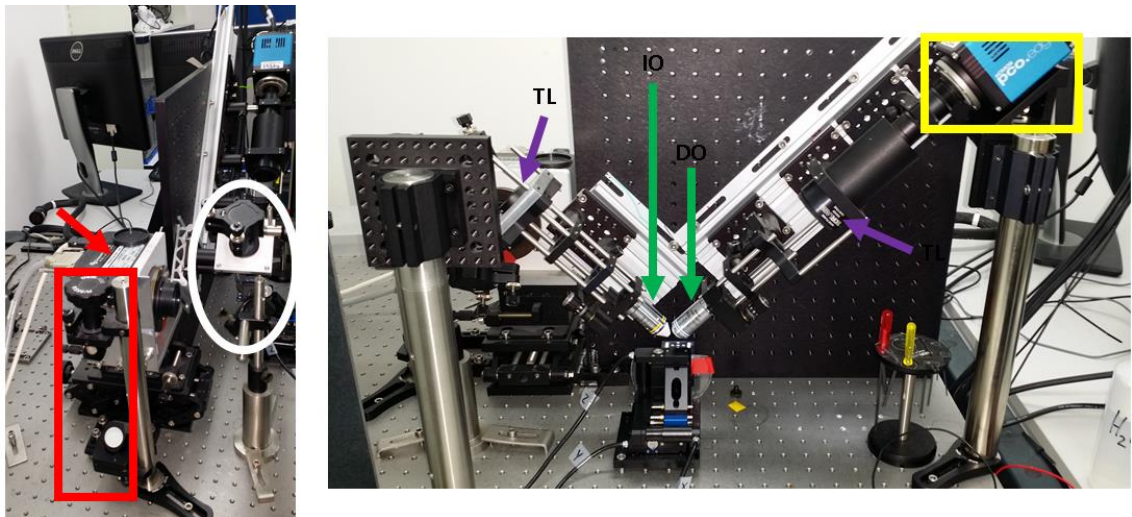


**Figure 2.1 Inherited DSLM microscope model.** On the left hand side image the red rectangle indicates the periscope which sends the laser beam through the scanner, pointed out by the red arrow. The white ellipse shows the periscope which sends the light-sheet through the tube lens, TL, and illumination objective, IO pair. On the right hand side image the TLs are indicated by purple arrows. The IO and detection objective, DO, are indicated by the green arrows. The microscope camera is shown in a yellow square.

With periscopes the microscope alignment was complex and the system instability was evidenced by camera vibrations noticed when image acquisitions was performed at 40x magnification.

Four months after starting this PhD project, the Lab was moved to a different location and the system rebuilt in a more stable configuration, using the same devices and removing the periscopes. The new DSLM configuration set-up is outlined in chapter 3.

## 2.2. Chick embryo preparation for imaging

The chick embryo culture, incubation and posterior mounting on the chamber for live imaging was performed following the protocol outlined by *Rozbicki et al*<sup>65</sup>. The reagents used to culture and mount the embryos for live imaging were:

- Sterile bacteriological petri dishes, 3 cm and 10 cm diameters;
- 30 mm filter paper disks, Whatman grade 1;
- Bacto Agar (BD 214010);
- Heavy Silicon Oil (polydimethylsiloxo-co-methylphenyl siloxane), density 1.066g/ml, viscosity 125cSt, (Aldrich 378488);
- Light Silicon Oil, density 0.93g/ml viscosity 10cSt (Aldrich 378321);
- Sodium chloride;
- Distilled water;
- 70% ethanol;
- Sterile distilled water;
- Fertilised GFP chicken eggs.

Prior to incubation, and after arriving from the Roslin Institute in Edinburgh, the embryos they were stored at 16° Celsius. Then the eggs were incubated at 38° Celsius for a time ranging from 1 hour up to 1 day, depending on the embryo developmental stage required for live imaging. After culturing, the embryos were incubated again until the start of the experiment. Before culturing the embryos, the petri dishes in which they will be kept developing until the mounting procedure for live imaging were prepared as follows:

- 1–** Prepare 0.6% Bacto agar in 121 mM NaCl. Warm the solution until it becomes transparent with no residual agar on the bottom of the reservoir. Cool to 48° Celsius and mix with 50 ml thin albumen collected with a syringe from fertilised eggs. Bed 3 ml of the mixture onto culture plates and allow to gel at room temperature. Plates can be kept several days at 4° Celsius;
- 2–** Prepare circular rings of Whatman filter paper by cutting out a central disk 25mmdiameter and sterilise the rings.

Once the dishes are ready, the embryos can be removed from the egg using the following procedure:

- 1–** Break the eggs into a clean 10 cm petri dish, keeping the vitelline membrane around the yolk intact;
- 2–** Orient the yolk such that the embryo sits on top;
- 3–** Clean the surface of the vitelline membrane with sterile tissue;
- 4–** Place the filter paper ring on top of the vitelline membrane centring the embryo in the hole of the filter paper ring;
- 5–** Cut the vitelline membrane around the outer edges of the filter paper with small scissors and gently lift the embryo off the yolk with fine forceps;

**6–** Place the embryos with the epiblast side down on the agar albumen filled culture dish and place under a microscope to check if the embryo structure is not compromised, Figure 2.2 B;

**7–** Remove excess yolk with fine tweezers.

The embryo is mounted on the sample holder plate, as shown in Figure 2.2 C, and placed inside the chamber, in order to proceed with embryo live imaging as follows:

**1–** Sterilise the sample holder plate with 70% ethanol and rinse with sterile distilled water (Figure 2.2 A);

**2–** Fill the central depression of the culture plate with 30  $\mu$ l of heavy Silicon oil;

**3–** Remove the filter paper mounted embryo from the petri dish and place it hypoblast side down over the central depression of the sample holder plate (Figure 2.2 D);

**4–** Place the black rubber O ring in the groove of the culture plate and press down gently with the help of two forceps (Figure 2.2 E). Cutting the O rings facilitates their mounting in the groove of the culture plate;

**5–** Remove the filter paper ring outside the embryo by tearing the vitelline membrane with fine forceps;

**6–** Place the sample holder plate in a sterile 3 cm petri dish and fill it with 3 ml of thin albumen and remove any yolk extruding from underneath the vitelline membrane into the four escape ports;

**7–** For observation in the light-sheet microscope the culture plate is mounted at the bottom of an observation chamber (microscope coverslip box, 7 cm  $\times$  3 cm  $\times$  1.8 cm (Figure 2.2 F). To immobilise the sample holder an agar mould is made fitting the sample holder plate. The mould is prepared in advance by placing an unused sample holder plate in the centre of the observation

chamber and filling it with 2 ml 1% agar in saline. After the agar is solidified the empty sample holder plate is taken out and replaced with the sample holder plate containing the mounted embryo (Figure 2.2 G);

**8**– Fill the box with 10 ml thin albumen containing 10  $\mu$ l of Penicillin Streptomycin to prevent bacterial contamination;

**9**– Mount preparation under the light-sheet microscope and cover the albumen with 2 ml light silicon oil to prevent evaporation.

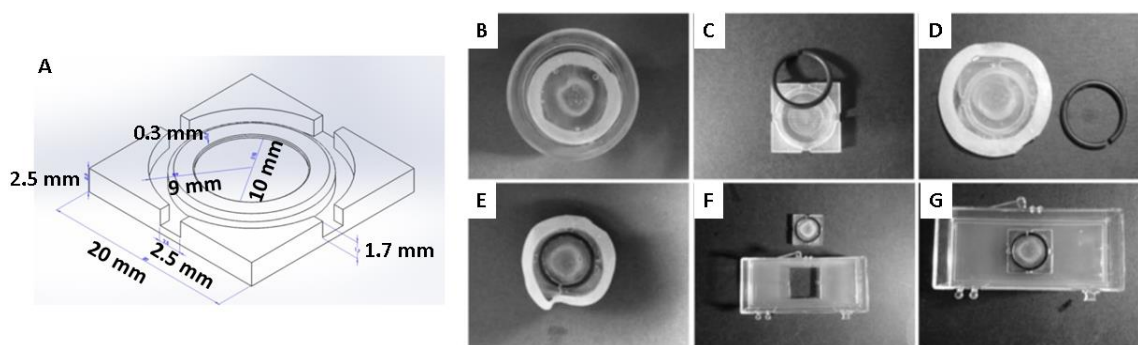


**Figure 2.2 Chick embryo mounting for light-sheet live imaging.** **A)** Sample holder plate, with its crucial dimensions. **B)** Embryo cultured inside of the petri dish, with epiblast facing the petri dish. **C)** The plastic sample holder plate and a black O ring. **D)** Embryo with filter paper on top of the sample holder plate with a cutted black O ring. **E)** Embryo placed in the centre of the sample holder plate and the black O ring used to immobilise it. **F)** Embryo mounted and immobilised on top of the sample holder plate. A mould made of agar is placed inside of a rectangular chamber. **G)** The sample holder plate is placed inside of the rectangular chamber, on the agar mould. The chamber is filled with 10 ml of albumen and 10  $\mu$ l of Pen/Strep.

To mount the embryo for epiblast or hypoblast live imaging the only difference lies on mounting the embryo with the epiblast or the hypoblast, respectively, facing the illumination and detection objectives (Figure 2.3). The chick embryo's epiblast and hypoblast cannot be imaged simultaneously with a single illumination beam at cellular resolution, due to the limited penetration depth of the light in the early embryonic chick tissue. In addition, it is not possible to observe both sides simultaneously, considering two separate illumination beams, due to the manner in which the embryos are mounted in the imaging chamber<sup>65</sup>, Figure 2.3. Nevertheless, a direct comparison between epiblast and hypoblast cellular behaviour and tissue flow is possible, by

looking at two chick embryos developing in the same temporal window. In one chick embryo the epiblast is imaged, whilst the hypoblast is imaged on the second chick embryo.

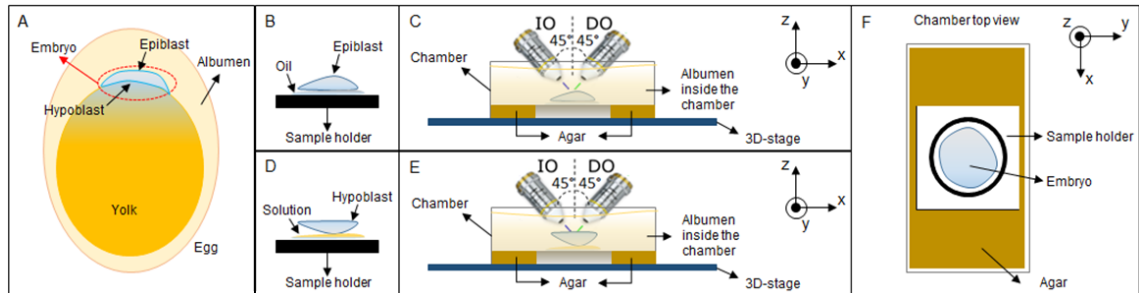


**Figure 2.3 Illustration of epiblast and hypoblast mounting for imaging.** **A)** Chick embryo inside the egg. The embryo sits on the top of the yolk and the epiblast is surrounded by albumen, while the hypoblast faces the yolk. **B)** Mounting the embryo in the sample holder to image the epiblast, the hypoblast is in contact with the Oil - Poly(dimethylsiloxane-co-methyl-phenylsiloxane) minimising the movements of the embryo inside of the chamber. **C)** The Illumination Objective (IO) and the Detection Objective (DO) bisecting the epiblast at a 45° angle. The sample holder is inside the chamber. The chamber is filled with 10 ml of albumen. **D)** To image the hypoblast the embryo is turned up-side-down. The epiblast is now in contact with an agar-albumen solution minimising movement of the embryo inside the chamber. **E)** The IO and the DO bisecting the embryos hypoblast at a 45° angle. The sample holder is inside the chamber, filled with 10 ml of albumen. **F)** Top view of the chamber. The sample holder is surrounded by agar to maintain the same position during the image acquisition.

**Note:** Dr Manli Chuai prepared the embryos presented in chapter 3. She also prepared the embryos in developmental stages HH1, HH3 and HH5 used in chapter 5, for the Gaussian vs Bessel beams analysis. The other embryos imaged and shown in this document were prepared by the researcher PhD candidate.

### 2.3. Dictyostelium Discodeum sample preparation

Ms Gail Singer, a previous member of Prof Kees Weijer Lab, prepared the Dictyostelium sample used for dual colour imaging, in chapter 3.



## 2.4. Beads and fluorescein solutions preparation

A solution of 1% agar was prepared and warmed to boiling point, then 5 ml of this solution was mixed with 5  $\mu$ l of 0.2 or 0.5  $\mu$ m beads. A centrifuge was used to mix up and spread the beads in the 5 ml of agar. The beads are provided by Molecular Probes FluoSpheres<sup>®</sup> and are fluorescent microspheres, emitting fluorescence in the yellow-green wavelengths, 505/515 nm, cat number F8811 and F8813, for 0.2 and 0.5  $\mu$ m size spheres. Then the mixture is placed inside a rectangular chamber (Figure 2.2 F and G) and cooled to room temperature to form a solid looking like rubber. This immobilises the beads to image them with the light-sheet microscope. Since the objectives used in the DSLM microscope are water immersion objectives, described in chapter 3 of this document, the rectangular chamber is filled with 10 ml of distilled water.

The fluorescein solution is prepared in the same manner as the bead solution. Using 1  $\mu$ l of fluorescein instead of 5  $\mu$ l beads to mix with 1% agar. Fluorescein was provided by Sigma-Aldrich, cat number 46955.

## 2.5. Beam reflected in mirror

To look at the profile of the illumination beam and the light-sheet a mirror is used. The mirror is placed inside the chamber used to mount the chick embryos and the chamber is filled with distilled water, since the objectives in use are specifically for water dipping imaging. Then, the chamber is placed on top of the 3D stage and the stage is moved up and down to observe the illumination beam and light-sheet profile at different z positions. This allows to find the illumination beam and respective light-sheet focus position.

## 2.6. The Richardson-Lucy deconvolution

The deconvolution code used for the Bessel images was performed using a version of the built-in Matlab function, adapted for Graphics Processing Unit (GPU) processing. The code is based on Lucy-Richardson deconvolution algorithm<sup>66,67</sup>. In the basic imaging deconvolution process an image can be improved using the measured optical system beam PSF and the acquired image.

Before performing the image deconvolution it is necessary to rotate the 3D acquired data to be orthogonally positioned in relation to the light-sheet, since all the cross-section images acquired with the microscope have the light-sheet being formed in parallel to it. The 3D stack volume is rotated to have the cross-section images orthogonally placed in relation to the light-sheet. Hence, the measured and smoothed 2D PSF can be used to deconvolve the cross-section images. The 2D PSF is measured from an image of the light-sheet acquired using a mirror in place of the sample, and takes the form of a Bessel-Gaussian profile. The rotated 3D stack is re-sliced orthogonally to the light-sheet, and each slice is sent to the GPU for 2D deconvolution in 10 iteration steps. This procedure allows a fast deconvolution without exceeding the memory limits on the GPU. Once the complete rotated 3D stack is deconvolved the stack is orthogonally rotated back to its original position.

This is a time consuming process with, for instance, a single 3D stack of  $2160 \times 640 \times 2173$  8-bit voxels taking 30 minutes to be deconvolved.

## 2.7. Embryo segmentation

The embryo cellular segmentation was performed using ImageJ *Find Maxima* function. Upon running the algorithm over a selected image, ImageJ outputs a figure

with the segmented regions considering watershed principle<sup>68</sup>. In present project, the code is used to segment cells at the chick embryo's epiblast.

## 2.8. Intensity and useful contrast metrics

In this document two metrics were used as a function of depth, the intensity and the useful contrast<sup>38</sup>. The former is calculated through measuring the total intensity signal at different depth levels, normalised to the maximum intensity measured. The latter is plotted through calculating the ratio between the intensity in the frequency range corresponding to structures between 2.5-10  $\mu\text{m}$  over the intensity in the frequency range corresponding to the total signal measured.

## 2.9. Images post-acquisition analysis algorithms

The codes used to show the embryo 2D surface projection, 3D stack data transformation, the Particle Images Velocimetry and the tissue contraction-expansion fate maps were all created and developed by previous members of Prof Kees Weijer Lab<sup>3</sup>. These codes were all implemented as post acquisition procedures for the DSLM *in vivo* chick embryo experiments, for data primary analysis and observation. No further changes were made in these codes during this PhD project.

### 2.9.1. 3D stack: chick embryo 2D surface images

All the embryo surface images presented in this document were calculated using a surface finding algorithm developed by previous members of the Prof Kees Weijer Lab<sup>3</sup>. The algorithm processes each 3D stack volume acquired with the microscope and projects the embryo surface into a 2D plane. The algorithm searches

along each 3D volume for a z slice with the maximum intensity value, by summing the individual pixel values in that z slice. The computer then places in a new 3D matrix nine z slices: the slice with the maximum intensity; the four z-slices before; and the four z slices after the z slice with maximum intensity. The new 3D volume is normalised, ranging 0 to 1 values. Then, the algorithm computes for each 3D matrix z pixels column the values exceeding a certain threshold value, only one pixel is selected by column. The threshold value is defined as a multiple of the mean intensity. Thus, the pixels in the 3D volume with the intensity above the threshold are outlined in a 2D plane, resulting in the embryo surface image.

### 2.9.2. 3D stack: data transformation

The 3D stack data transformation algorithm is used to orientate the acquired 3D stack with the cross-section images in 45° angle to vertical cross-sections (Figure 2.4).

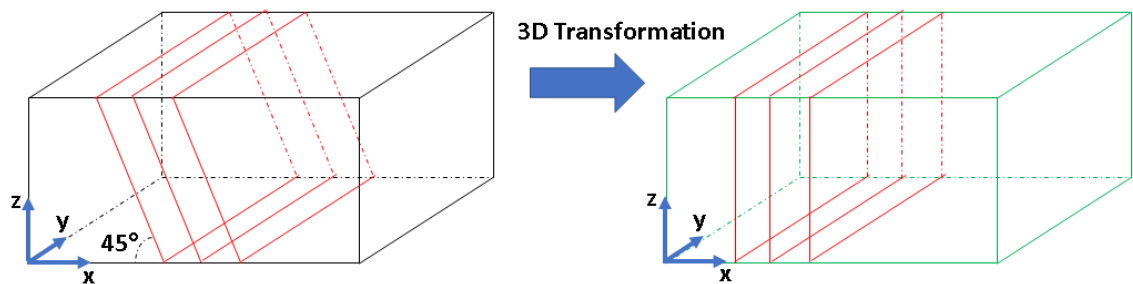
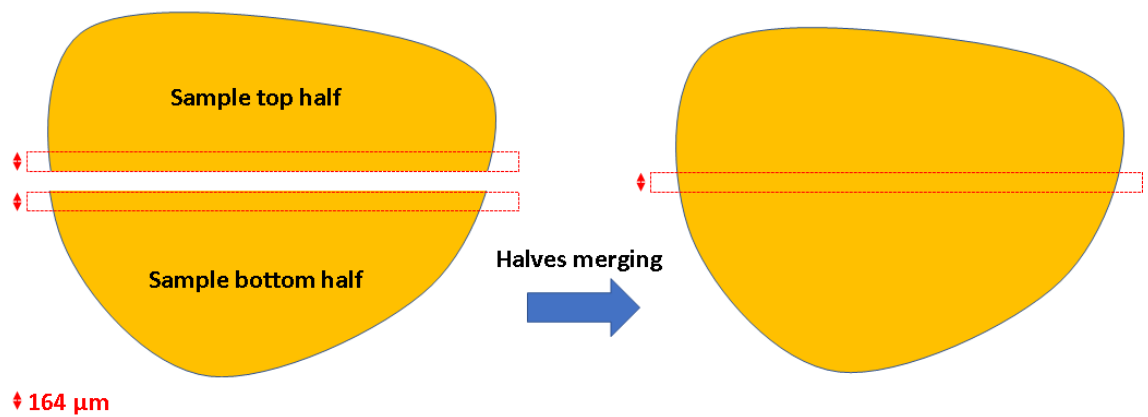


Figure 2.4 3D stack data transformation.

### 2.9.3. Sample dual scan – merging images

Other post-acquisition code used during this PhD project was the code to merge the embryo surface two-halves into one. The code was available at Prof Kees Weijer Lab. The code stitches two halves together, considering each half individual 2D surface projection followed by calculating the most optimal merging of the same

region imaged in both halves. This region is confined to 252 pixels or 164  $\mu\text{m}$  at 10x magnification (Figure 2.5).



**Figure 2.5** Illustration of sample top and bottom halves are merged into one.

#### 2.9.4. Particle Image Velocimetry and tissue fate maps

These two algorithms are implemented using Matlab. The codes were written by previous members<sup>3</sup> of Prof Kees Weijer Lab. The codes are used immediately after completing a 3D image acquisition, and the results provide information relative to the embryo tissue flows, in case of Particle Image Velocimetry (PIV), and highlight the tissue contraction and expansion regions. Both codes are used between consecutive images of a time lapse sequence showing pixel movements during image acquisition.

### 3. DSLM for imaging of chick embryos

LSFM is a versatile technique since both illumination and detection axes are orthogonal to each other. Therefore, the microscope can be built around the sample conserving the 90° angle between the two axes.

#### 3.1. System overview

The DSLM microscope was designed to image large fragile flat samples such as chick embryos, which need to be kept horizontal to develop normally. Due to its complexity, the embryo cannot be inserted in capillaries, a simplified mounting procedure often used for smaller samples such as zebrafish<sup>41</sup> and *Drosophila*<sup>69</sup> embryos, since normal chick embryonic development is compromised.

The chick embryos are horizontally cultured and mounted on a specially designed chamber for imaging<sup>65</sup>. The embryos can be cultured inside an incubator at 38° Celsius for up to three days, after which they stop developing. The membrane GFP is expressed under the control of a promoter that is active throughout development. The strength of the membrane fluorescent signal varies considerably from embryo to embryo (Figure 3.1), independent of the embryo's developmental stage. The reasons for this are not yet completely clear.

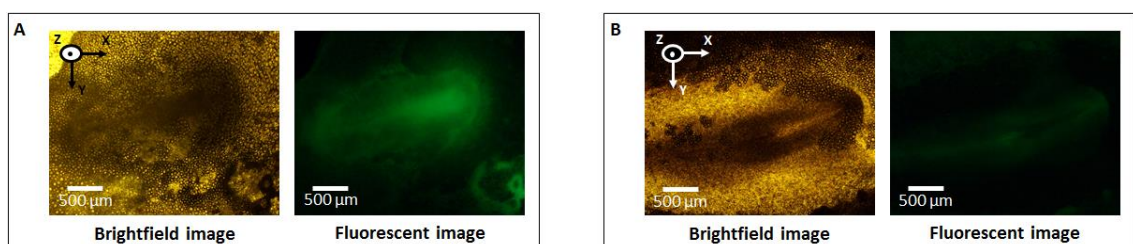


**Figure 3.1** Bright field and fluorescent images of two different transgenic chick embryos acquired with a conventional light microscope at 2.5x magnification. Fluorescent images were acquired with the same laser intensity power and exposure time. **A)** Embryo at HH5 and **B)** embryo at HH6 stages of development.

Since the samples are kept horizontally orientated the light-sheet slices the sample at a  $45^\circ$  angle (Figure 3.2). The detection objectives used on the system provide 10x or 40x magnification,  $NA = 0.3$  and  $0.8$  respectively. Another 10x magnification objective is used as illumination objective.

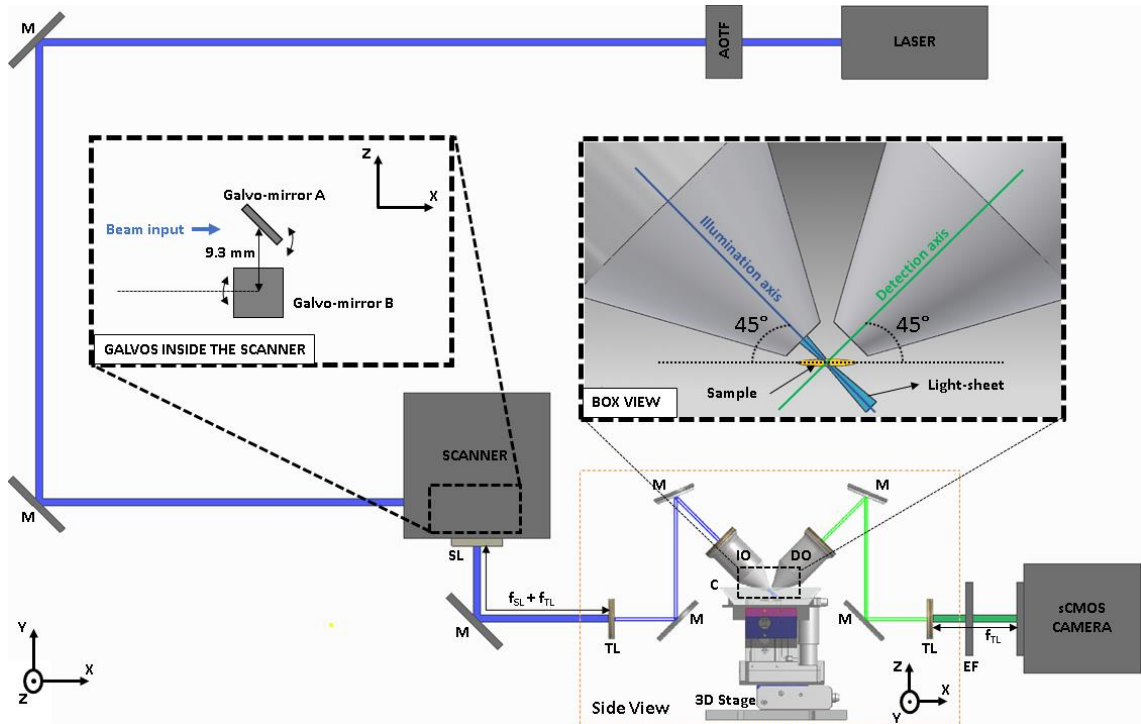


**Figure 3.2 DSLM set-up, with objectives oriented at  $45^\circ$  angle towards the sample surface.** System top view, with sample holder, illumination and detection objectives in side view. The laser is monochromatic 488 nm; the AOTF working as a shutter can control up to 8 wavelengths simultaneously; M – Mirror; Scanner (composed by two galvo-mirrors) generates the light-sheet; SL – Scan Lens. On the side view: TL – Tube Lens; M – Mirror; IO – Illumination Objective; C – Chamber holding the embryo; DO – Detection Objective; 3D stage to position and move the sample; EF – Emission Filter. In the expanded box view, the sample is illuminated by the light-sheet at a  $45^\circ$  angle. In the Scanner expanded box “GALVOS INSIDE THE SCANNER”, visible the operation of the two galvo-mirrors, A and B can be seen. Galvo-mirror A scans the beam along X axis and Galvo-mirror B scans the beam along Z axis. The  $f_{SL}$  is the focus Scan Lens length, 60 mm, and  $f_{TL}$  is the focus Tube Lens length, 200 mm. The distance between each TL and the corresponding IO/DO is 200 mm.

The illumination Gaussian beam has approximately  $2.2 \mu\text{m}$  FWHM, and thus a depth of focus of around  $45 \mu\text{m}$ . To maintain the embryo at  $38^\circ$  Celsius, the optimal development temperature, the chamber that holds the embryo is heated by a metallic plate on the stage.

During image acquisition the embryo is moved to specific positions, on a stage in a step by step motion. After each step a light-sheet is generated, and an image is

acquired. This process is repeated until the region of interest is covered. The 3 axes stage, or 3D stage, has a maximum velocity of 3 mm/s and a positioning resolution of 17 nm. The scanner used to generate the light-sheets has two galvo-mirrors (see "GALVOS INSIDE THE SCANNER" box in Figure 3.2), this allows the beam to be scanned along the X axis using galvo-mirror A, whilst galvo-mirror B is used to align the illumination sheet to the focal plane of the detection objective. The perpendicular distance between the two galvo-mirrors rotation axes is 9.3 mm. Coupled and screwed into the scanner box there is a f- $\theta$  scan lens with focal length of 60 mm. The rear edge of the scan lens housing is placed approximately 25 mm, or the lens aperture stop distance<sup>70</sup>, from the centre of the galvo-mirror B. The f- $\theta$  scan lens generates a flat image plane, imaged through the tube lens and illumination objective into the sample. The scanner triggers the camera and controls its exposure time through a hardware Transistor-Transistor Logic (TTL) connection. The scientific Complementary Metal-Oxide Semiconductor (sCMOS) camera has a maximum frame rate of 100 frames per second at full frame size. The camera exposes while the light-sheet is being generated. The camera in turn controls the Acousto Optic Tuneable Filter (AOTF) through a hardware connection to let the laser beam pass to the scanner. The AOTF is used in conjunction with a frequency synthesiser capable of controlling up to 8 wavelengths ranging 400-650 nm. The AOTF works as a shutter for the laser beam. When the camera is not exposing, the AOTF deviates the laser beam from the scanner, avoiding unnecessary illumination, and therefore preserving the sample. The laser source is monochromatic with a wavelength of 488nm, to excite the membrane targeted GFP expressed in the transgenic chick embryos. All the devices and parts used on the DSLM set-up are presented in Table 3-1. To ensure that all the hardware TTL connections



work properly and at correct timings an Oscilloscope was used. The Oscilloscope was provided by Pico Technology, with part number PicoScope 2206B.

Furthermore, two independent computers control the microscope: one computer controls the light-sheet generation and sample positioning in 3D coordinates; while the second computer controls the image acquisition and storage. A custom software written in a C++ language is used in both computers.

**Table 3-1 Parts and devices used on DSLM set-up.**  $\lambda$  – Wavelength, F – Focal Length, NA – Numerical Aperture, WD – Working Distance, CW – Continuous Wave.

Devices / Parts	Company	Part Number	Specification
Laser	JDSU	FCD488-020	$\lambda = 488 \text{ nm}$ , CW
AOTF	Gooch & Housego	TF525-250-6-3-GH18A	$\lambda$ : 400 - 650 nm
AOTF Frequency Synthesiser	Gooch & Housego	MSD040-150-0.2ADM-A5H-8x1	Control up to 8 channels or 8 wavelengths
Mirrors	Thorlabs	PF10-03-P01	Protected Silver Mirror
Scanner	Cambridge Technology	ProSeries Scan Head 7 61707PSXY2T-S4	$\lambda$ : 532 - 10600 nm
Scan Lens	Sill Optics	S4LFT0061/65	F = 60 mm $\lambda$ : 450 - 650 nm
Tube Lenses	Thorlabs	TTL200	F = 200 mm $\lambda$ : 350 - 700 nm
Objective 10x	Nikon	N10XW-PF	NA = 0.3 / WD = 3.5 mm
Objective 40x	Nikon	N40X-NIR	NA = 0.8 / WD = 3.5 mm
Emission Filter	Semrock	FF03-525/50-25	Band pass filter: 525/50 nm
sCMOS Camera	PCO	5.5 Edge	Pixel: 6.5 $\mu\text{m}$ * 6.5 $\mu\text{m}$ Chip: 2560 * 2160 pixels Full frame acquisition rate: 100 frames/second
3D Stage	Physik Instrumente	M-111K028	Max Velocity = 3 mm/s Resolution = 17 nm 3 Axes mounted -> XYZ

Chick embryos possess an undulated surface. The undulation is only minimal immediately after egg laying but increases with developmental time, introducing challenges in maintaining image sharpness as parts of the embryo can move out of the light-sheet focus and/or the detection focus. Hence, an algorithm to adjust the embryo

position, keeping its surface always in focus, is implemented in the microscope software. The light-sheet focus is positioned at the middle of the acquired image frame on the detection plane, for optimal sectioning of the surface of the chick embryo (Figure 3.3 C). A mismatch between the light-sheet focus and the embryo's surface result in a position adjustment requirement. This mismatch is translated into a new stage position, to correctly adjust and place the embryo's surface back into the light-sheet and detection focus.

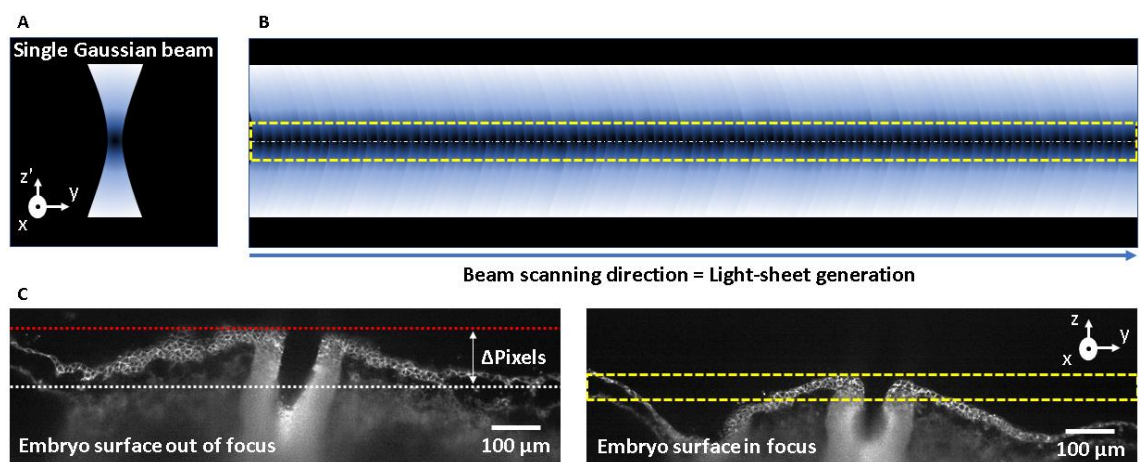


**Figure 3.3 Illustrations of a Gaussian beam profile and a DSLM light-sheet generation. Chick embryo at HH6 cross-section images, with the embryo surface being adjusted into the light-sheet focus. A)** Illustration of a Gaussian beam profile, with its depth of focus highlighted by the dark central region of the beam. **B)** Illustration of a light-sheet formation through the scanning of the Gaussian beam shown in figure A. The yellow dashed rectangle indicates the light-sheet focus range. The dashed white line indicates the light-sheet focus midline. **C)** Embryo's surface (dashed red line) does not match the light-sheet focus midline (dashed white line). The left-hand image shows the surface of the embryo out of focus. The mismatch in number of pixel lines,  $\Delta\text{Pixels}$ , between the dashed red and dashed white lines result in the necessary adjustment to place the embryo's surface inside the light-sheet focus. On the right-hand image, after embryo's surface adjustment only part of its surface will be in focus, inside the dashed yellow rectangle, due to embryo's curvature. Z, from cross-section image (right) on C, is at  $45^\circ$  angle to  $Z'$ , from illustration on A.

A large set of consecutive images taken at a  $45^\circ$  angle is acquired with regular spacing and transformed into a 3D stack (Figure 3.4 B). Each frame has  $2560 \times 400$  pixels. After egg laying the chick embryo resembles a disc with a diameter of approximately 4 mm, with approximately 400 000 cells. Covering the 4 mm with images acquired at regular  $2 \mu\text{m}$  intervals results in a 3D stack with 2000 frames,

typically acquired at 12-14 frames per second. A single 3D stack, of 2000 images, is equivalent to 2 Gigabytes (GB) of data. To keep the embryo cross-section images constantly in focus, the embryo's surface coordinates are adjusted after a complete 3D stack acquisition. This ensures that for the next 3D stack the embryo surface will remain in focus. A series of 3D stacks is acquired consecutively, spaced by 2-3 minutes, for approximately twenty hours, resulting in 500–600 volumes and approximately 1 Terabyte (TB) of data. Then a video from this 4 dimensional (4D) data is produced (Figure 3.4 C). From the volumetric data, the 2D embryo surface is extracted by a dedicated surface finding algorithm, showing the embryonic cell behaviours in the epiblast of the embryo during gastrulation. The temporal resolution of 2-3 minutes is sufficient to investigate gastrulation at tissue level as well as relevant cellular behaviours such as cell shape change, division, ingression and cell rearrangements such as cell-cell intercalation<sup>3</sup>.

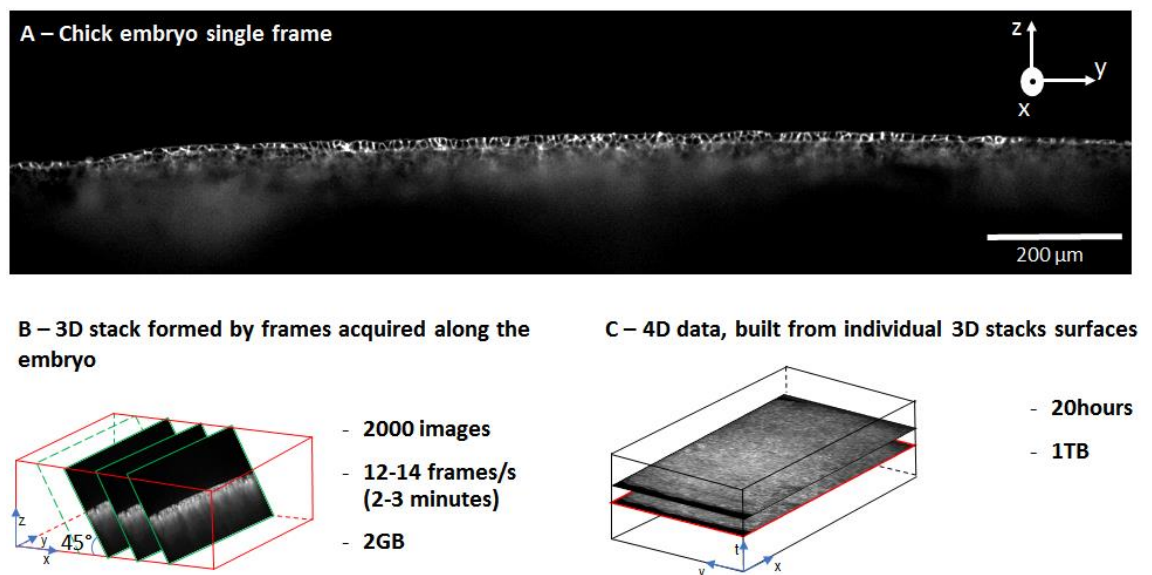


**Figure 3.4 Image acquisition, storage and processing workflow.** **A)** Example of a raw cross-section image acquired with the DSLM. Using a 10x magnification objective. **B)** 3D stack result from the acquisition of individual cross-section images acquired along the region of interest. 2000 images acquired at 12-14 frames per second result in 2GB of data. **C)** After 20 hours of imaging the chick embryo around 500 – 600 3D stacks are originated, approximately 1TB.

The imaged embryo surface has the width of the camera chip which is 2560 pixels. Each pixel is  $6.5 \mu\text{m} * 6.5 \mu\text{m}$ , resulting in a field of view of approximately 1.7 mm with a 10x magnification objective. Since after egg laying the embryo looks like a disk with around 4 mm diameter, only approximately half of the embryo is imaged (Figure 3.5).



**Figure 3.5 Chick embryo partial surface with a length of 4.2mm and a width of 1.7 mm.** Image acquired with 10x magnification detection objective. The mid-region of the chick embryo surface before the beginning of the primitive streak formation.

By scanning the embryo twice, it is possible to image 90-95% of the embryo surface. Doing this at 12-14 frames per second leads to a reduced temporal resolution of approximately 6 minutes. This time is too long to observe processes such as cell division and cell ingressions in detail, resulting in considerable loss of information, for important cellular behaviours.

### 3.2. High speed DSLM

To maintain the temporal resolution of 3 minutes and increase the embryo imaged area it is necessary to speed up the microscope acquisition frame rate. The sCMOS camera in use has a maximum frame rate of 100 frames per second at full resolution of the camera chip,  $2560 * 2160$  pixels. As mentioned previously, a single frame covers a small portion of the camera chip,  $2560 * 400$  pixels, allowing the frame

rate increment above 100 frames per second. Through the implementation of new acquisition protocols resulting in software changes it was possible to speed up the microscope frame rate and scan the embryo twice. Covering around 90-95 % of the embryo surface, Figure 3.6, in less than 3 minutes.



**Figure 3.6 Chick embryo surface with a length of 4.8 mm and a width of 3.2 mm.** Most of the embryo region was covered through scanning the embryo twice and merging the two surface images.

The step by step motion of the stage turns out to be a relatively slow process. To make a single step between two defined and measured positions the code takes approximately 45 milliseconds (ms), on top of the time required for the acquisition of a single frame. A minimum rate of 24 frames per second is required to image 90-95% of the embryo, covering 4mm of extension. Therefore, to speed up microscope data acquisition the step by step motion was abandoned and replaced with a continuous stage movement for data acquisition of a single 3D stack (Figure 3.7). Originally a scan command was issued after every step to generate the light-sheet, which then triggered



the camera to take an image. In the new configuration, the scanner executes an internal programme generating the required number of light-sheets equal to the number of frames to be taken per 3D stack in the required time. When the first light-sheet is about to be generated, the scanner triggers the stage to start the continuous movement. No changes in the operation of the camera and AOTF were required.

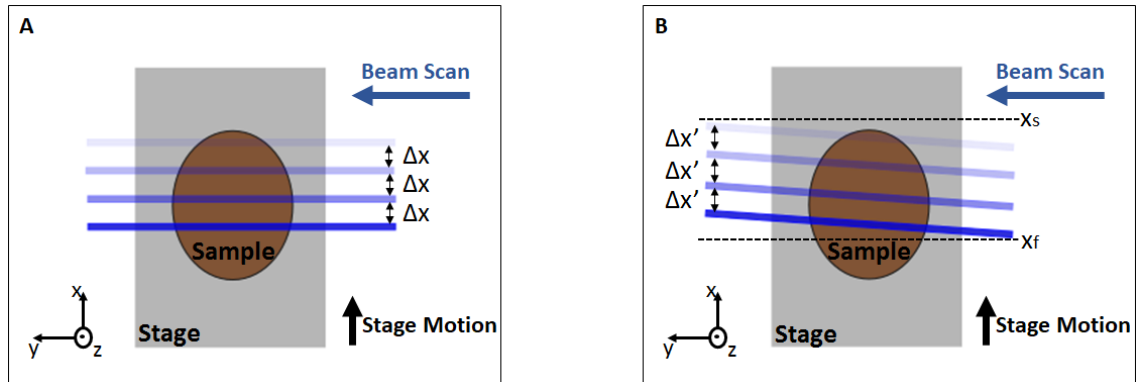


**Figure 3.7 Overview of two different scanning modes from the perspective of the sample.** The blue lines indicate the position of individual light-sheet generation and image acquisition. **A)** Stage moves in step by step motion and images are acquired with the stage stopped,  $\Delta x$  is the step size. **B)** Stage in continuous movement between start position ( $X_s$ ) and finishing position ( $X_f$ ) at constant velocity. With images being acquired at equally spaced positions  $\Delta x'$ . The lines are tilted due to stage continuous movement, to differentiate between having the stage completely stopped, illustration A, and in motion, illustration B, during light-sheet generation.

Questions to consider were: will the images be equally spaced? Will the images be distorted due to stage continuous movement?

The first question is easy to answer by imposing a strict synchronisation between the stage and scanner. With the stage moving the embryo at a constant velocity it was ensured that the light-sheets are formed at the required frequencies and timing by setting the appropriate scanner parameters. Remembering that, for the DSLM system in use, either in stepping or continuous motion modes, the light-sheet formation rate is equal to the image acquisition frame rate. Because, as was stated previously the light-sheet generation time is equal to the camera exposure time. The high speed of the laser beam scanning to form the light-sheet relative to the

continuous stage movement at constant velocity ensures that all cells are captured. Since cells have an average diameter of  $10 \mu\text{m}^3$  the same cell is imaged in two to three consecutive images. If the stage moves at  $0.4 \mu\text{m}/\text{ms}$ , 4 mm of tissue is imaged in 10 seconds, with frames acquired at 100 frames per second. In the experiments performed, normally, 4 mm of embryo's surface was imaged in approximately 60 seconds using a velocity of approximately  $0.07 \mu\text{m}/\text{ms}$ , i.e the stage moves even slower than suggested above. Thus, a frame rate of 24 frames per second works well, giving a reasonable frame temporal spacing such that no distortion should be noticed during image acquisition. With higher frame rates the embryo is scanned twice, imaging complementary sites of the embryo (Figure 3.8). After acquisition the two halves are merged, Figure 3.6.

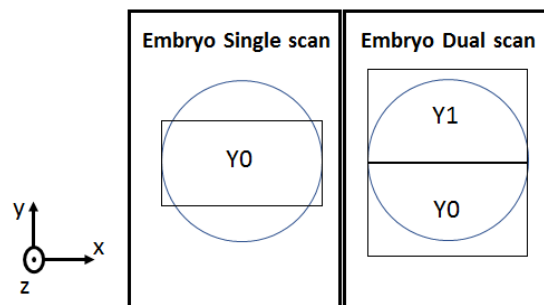


**Figure 3.8 Embryo single and dual scan modes.** In single scan, the acquisition process occurs for the same y position, Y0. In dual scan, the acquisition process occurs sequentially for two different y positions, Y0 and Y1. After the two 3D stacks are acquired they are merged. In the diagram, the blue circle represents the embryo and the black rectangles represent the field of view, in dual scan the field of view is doubled.

### 3.2.1. Results

With Dual scan 90-95% of the embryo is imaged every 2-3 minutes during early stages of development. As a result, most of the primitive streak can be imaged and the tissue cellular dynamics are measured in a broader area (Figure 3.9).

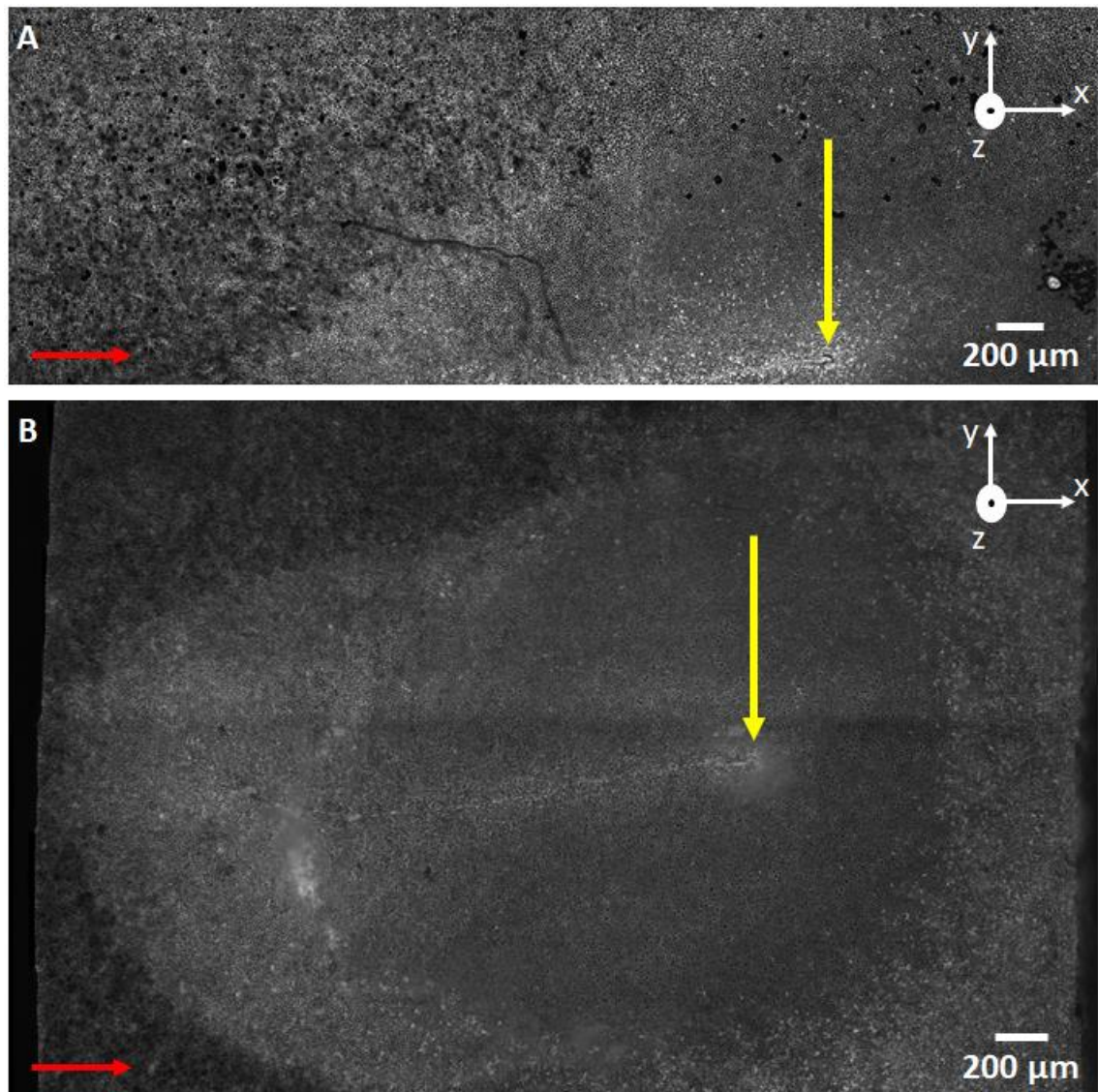


**Figure 3.9 Embryo single and dual scans, with 10x magnification detection objective. A)** Embryo single scan, the streak is partially visible. **B)** Embryo dual scan, the streak is completely visible. The red arrow indicates the Posterior → Anterior direction and the yellow arrow indicates the anterior tip of the primitive streak, the Hensen's node.

For a first analysis, the differences between single and dual scan are visible after applying Image Velocimetry (PIV) algorithm<sup>3</sup> to both data sets. For the primitive streak images presented in Figure 3.10 the tissue flow movements shown by the green arrows are only partially visible in a portion of the embryo using single scan (Figure 3.10 A) but are much better illustrated over a broader region using dual scan (Figure 3.10 B).



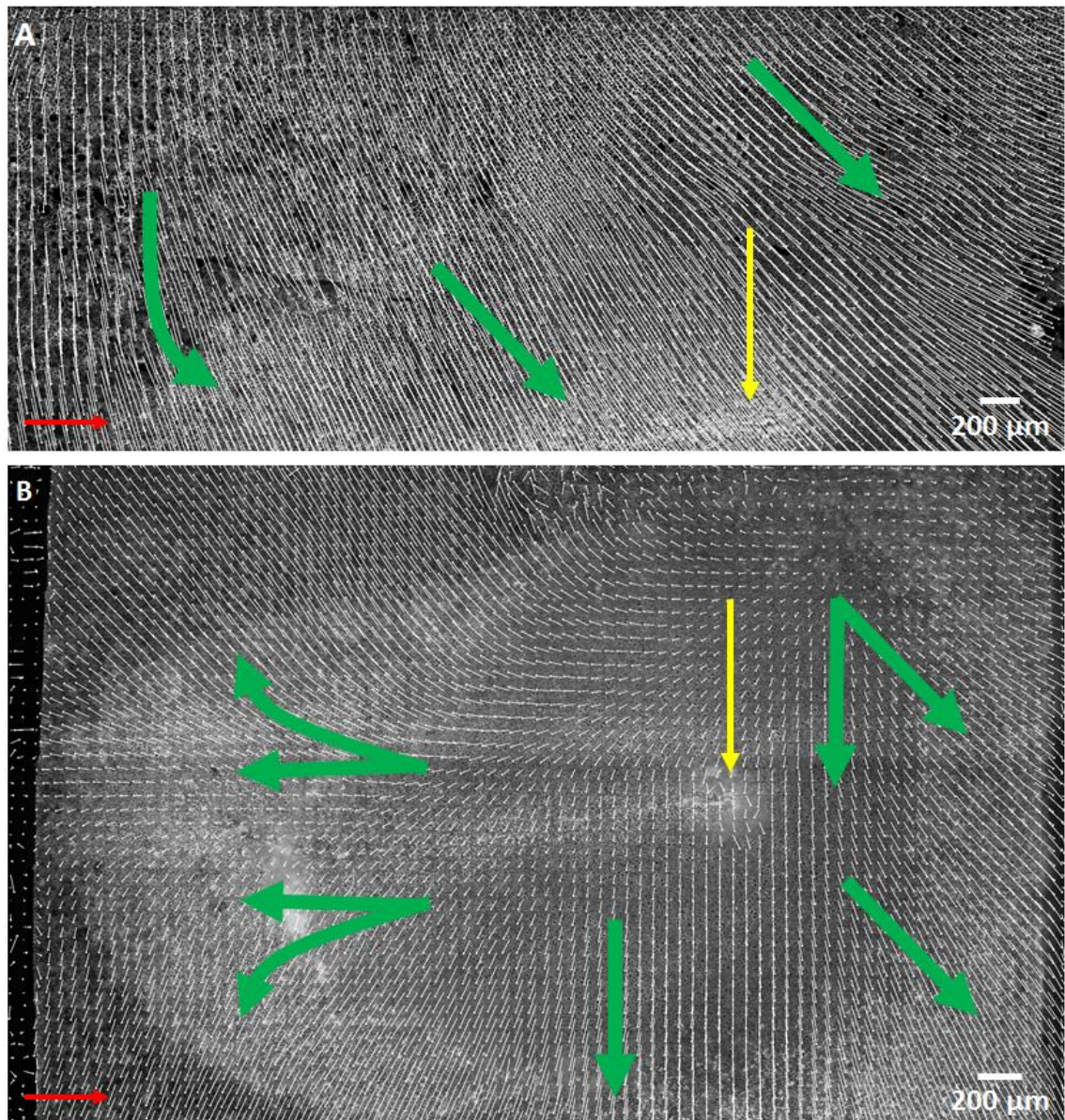


**Figure 3.10 PIV applied to two chick embryo surfaces.** The red arrow indicates the Posterior → Anterior direction and the yellow arrow indicates the position of the anterior tip on the primitive streak, the Hensen's node. The green arrows indicate the tissue flow directions. **A)** Image acquired through single scanning mode. The tissue flows indicate an expansion of the embryo towards the bottom side of the field of view. **B)** The image was acquired in dual scanning mode generating two independent 3D stacks, merged upon acquisition. The tissue flow indicates a more symmetrical expansion in the posterior site of the embryo, to the bottom and top sites of the field of view. Accompanied by a strong expansion quasi-unidirectional on the anterior site.

Using single scanning mode and a 40x magnification detection objective to image the same chick embryo with the stage step by step motion and the stage continuous motion modes, no differences are noticed in the embryo surface images as presented in Figure 3.11.



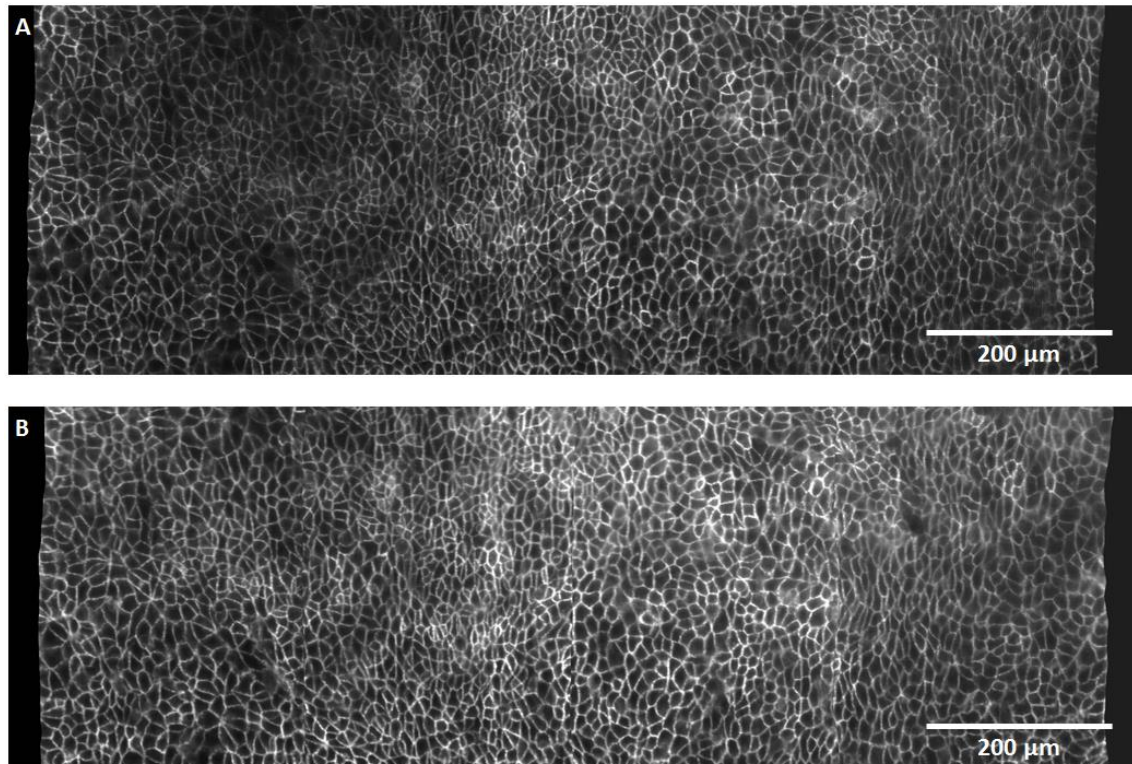


**Figure 3.11 Embryo surface images acquired in single scan mode at 40x magnification. A) Using step by step stage motion. B) Using continuous stage motion.**

The chick embryo hypoblast development was imaged during early gastrulation. The primitive streak triggers gastrulation and the streak reaches its maximum extension 16 hours<sup>8</sup> after egg laying. This is the embryo developmental time window. Currently there are no long live recordings of the hypoblast development in early chick embryos at cellular resolution.

When the embryos were mounted with the hypoblast facing the light-sheet, most of the embryos did not survive more than a few hours in culture before detaching from the vitelline membrane and collapsing, whether the hypoblast faced either albumen or an appropriate phosphate buffer. A permanent contact between hypoblast and yolk inside the egg is very different than having hypoblast in contact to albumen or buffer, resulting in crucial developmental changes like shrinking of the embryo.

The hypoblast images presented in the following page were acquired using stage continuous motion and embryo dual scan modes. The hypoblast surface is followed at cellular resolution, covering almost all tissue as shown in Figure 3.12.

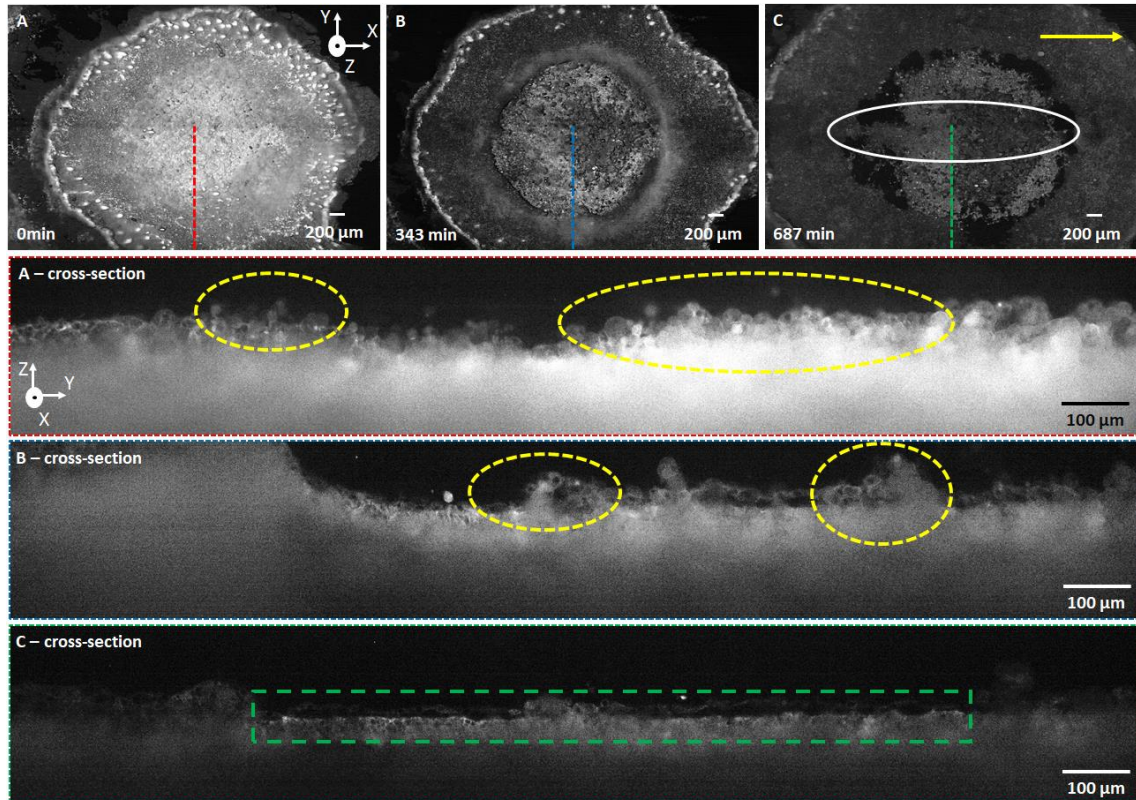


**Figure 3.12 Chick embryo hypoblast development imaged for more than 11 hours.** Images acquired in continuous motion and embryo dual scanning modes. Images **A)**, **B)** and **C)** represent the hypoblast surface development from the beginning of gastrulation at 0 minutes, 343 minutes and 687 minutes, respectively. The red, blue and green dashed lines indicate the region from which **A)**, **B)** and **C)** - cross-section images were acquired. The white ellipse in **C)** indicates the region at which a streak formation would be active. The yellow arrow shows the Posterior → Anterior direction. The dashed yellow ellipses in **A)** and **B)** are surrounding regions with agglomerates of cell clusters made of round cells. The dashed green rectangle in **C)** - cross-section confines a region of a flat layer of small cells.

The hypoblast surface, Figure 3.12, looks considerably less sharp than the epiblast, Figure 3.13.



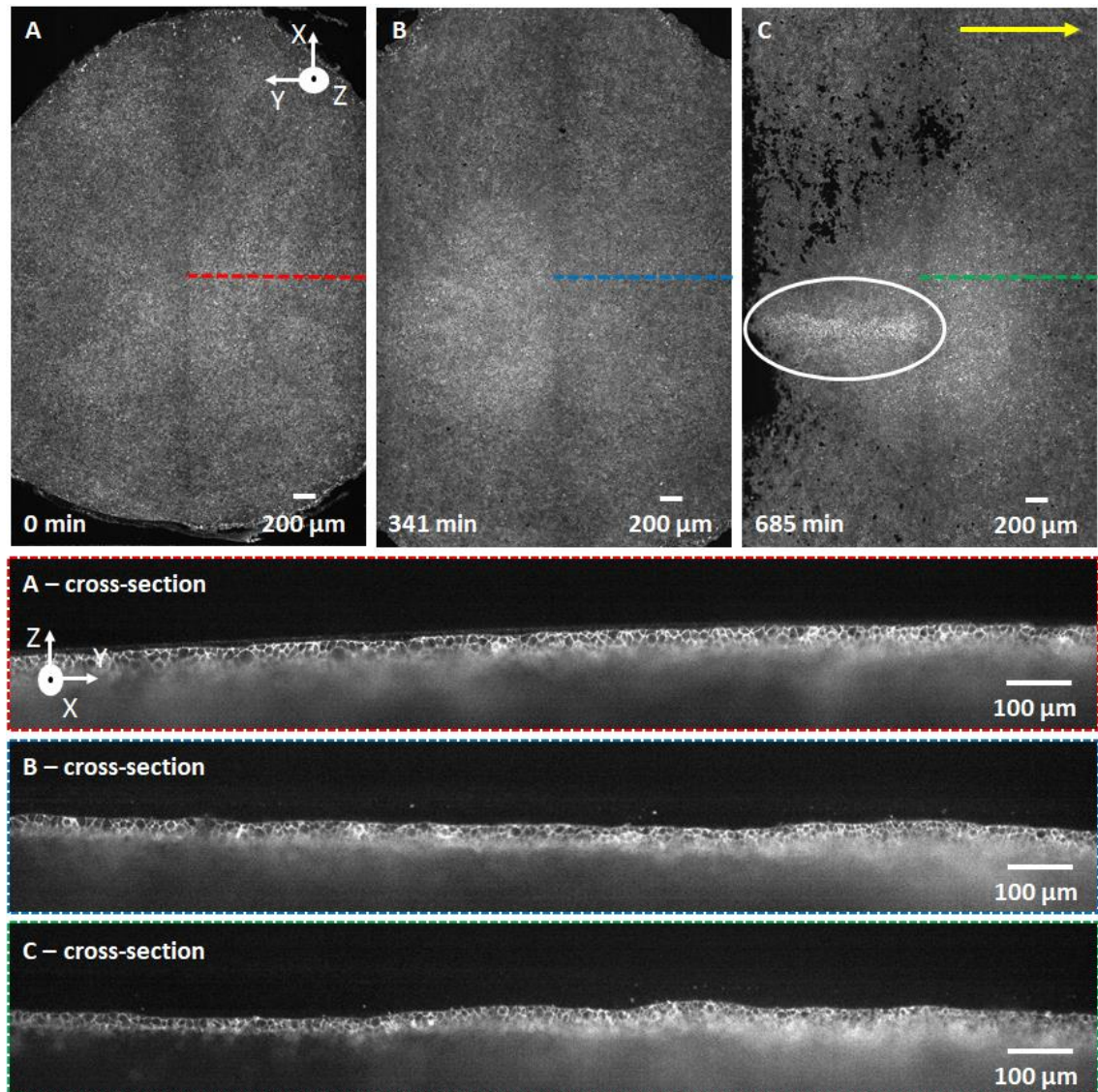


**Figure 3.13 Chick embryo epiblast development imaged for more than 10 hours.** Images acquired in continuous motion and embryo dual scanning modes. Images **A)**, **B)** and **C)** represent the epiblast surface development since the beginning of gastrulation at 0 minutes, 341 minutes and 685 minutes, respectively. The red, blue and green dashed lines indicate the region from which **A)**, **B)** and **C)** - cross-section images were acquired. The white ellipse indicates the streak region. The yellow arrow indicates the Posterior → Anterior direction.

The hypoblast is initially formed by scattered clusters of round cells<sup>10</sup> as can be seen in the cross-section images of Figure 3.12, dashed yellow ellipses in A – and B – cross-section images. Over time the cells start to organise and the initial agglomerates of cell clusters gradually disappear and then a flat layer of cells<sup>9</sup> starts to take shape, as indicated by the region inside the dashed green rectangle from Figure 3.12 C – cross-section image. Looking at the tissue perspective, in the mid region of the hypoblast

surface a central circular region appears evident<sup>71</sup> (Figure 3.12 B and C). This central circular region looks nebular and turbulent. The white ellipse from Figure 3.12 C indicates the embryo middle region where the primitive streak should be located.

As stated in the previous chapter, the hypoblast and epiblast cannot be imaged simultaneously using the same embryo, due to the mounting of the embryo to be imaged by the DSLM, and additionally due to the limited penetration depth provided by Gaussian light-sheet and the embryo structural complexity. Hence, looking at the same embryonic developmental time window as the one for hypoblast, the epiblast was imaged using another embryo mounted with the hypoblast face up (Figure 3.13).

Using visual comparison of the hypoblast and epiblast developments shown in Figures 3.12 and 3.13, respectively, the epiblast appears to have a smoother surface with a clearer organisation and positioning of its cells.

To perform a primary examination of tissue flow and dynamics of the results presented in Figures 3.12 and 3.13 a post-acquisition analysis of the data was performed using PIV and Contraction-expansion fate map algorithms<sup>3</sup>. The resulting calculations are presented in Figures 3.14 and 3.15, for hypoblast and epiblast, respectively.

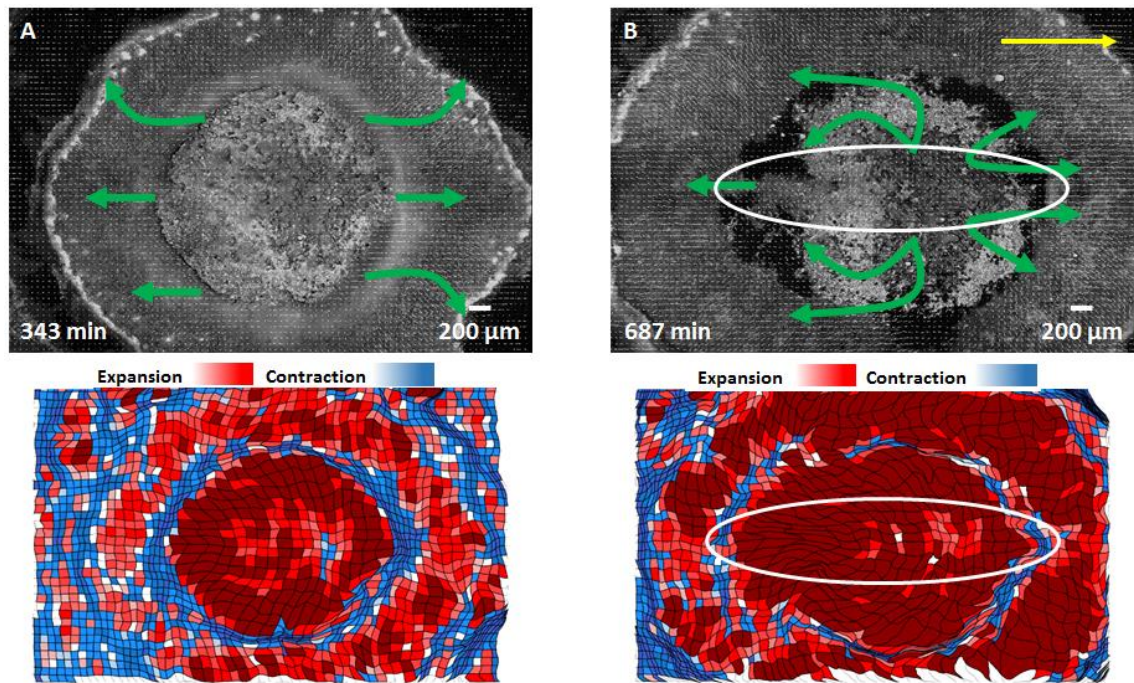


**Figure 3.14 Chick embryo hypoblast surface PIV (top) and expansion-contraction maps (bottom).** Embryo's hypoblast surface images after 343 minutes **A**) and 687 minutes **B**) of live imaging. The white ellipse indicates the region at which streak formation would have occurred. The green arrows show tissue flow directions while the yellow arrow indicates the Posterior → Anterior direction.

With the PIV and Contraction-expansion fate maps the results were visually and directly compared and correlated for both epiblast and hypoblast surfaces. Although the images come from two different embryos the images are recorded at the same developmental time window. A search of the literature did not show results for chick embryo early stage development hypoblast live imaging in order to establish other comparisons, only observations made with electron microscopy images<sup>9,10,71,72</sup>. Consequently, the next statements rely only on personal observations. For both epiblast and hypoblast surfaces, the PIV images show a clear expansion of the two embryos in all directions. In the hypoblast surface the Contraction-expansion fate maps reveal strong expansion of the tissue in its central region and a circular shaped contraction on the boundary between the central unclear nebular region and the surrounding region. If, as suggested earlier, at chick embryo early developmental

stages during EMT the future mesendoderm cells will move to the sides at deeper layers below the epiblast (Figure 1.2) it appears that this tissue expansion is justified by the displacement made by these cells onto and into the hypoblast. In the epiblast the characteristic vortex flow<sup>3</sup> (red arrows in Figure 3.15) is seen well before primitive streak formation can be visually detected. The epiblast Contraction-expansion maps show a strong contraction of the tissue in the primitive streak furrow (white ellipse in Figure 3.15) and at its anterior end and an expansion of the tissue in all the regions surrounding the streak.



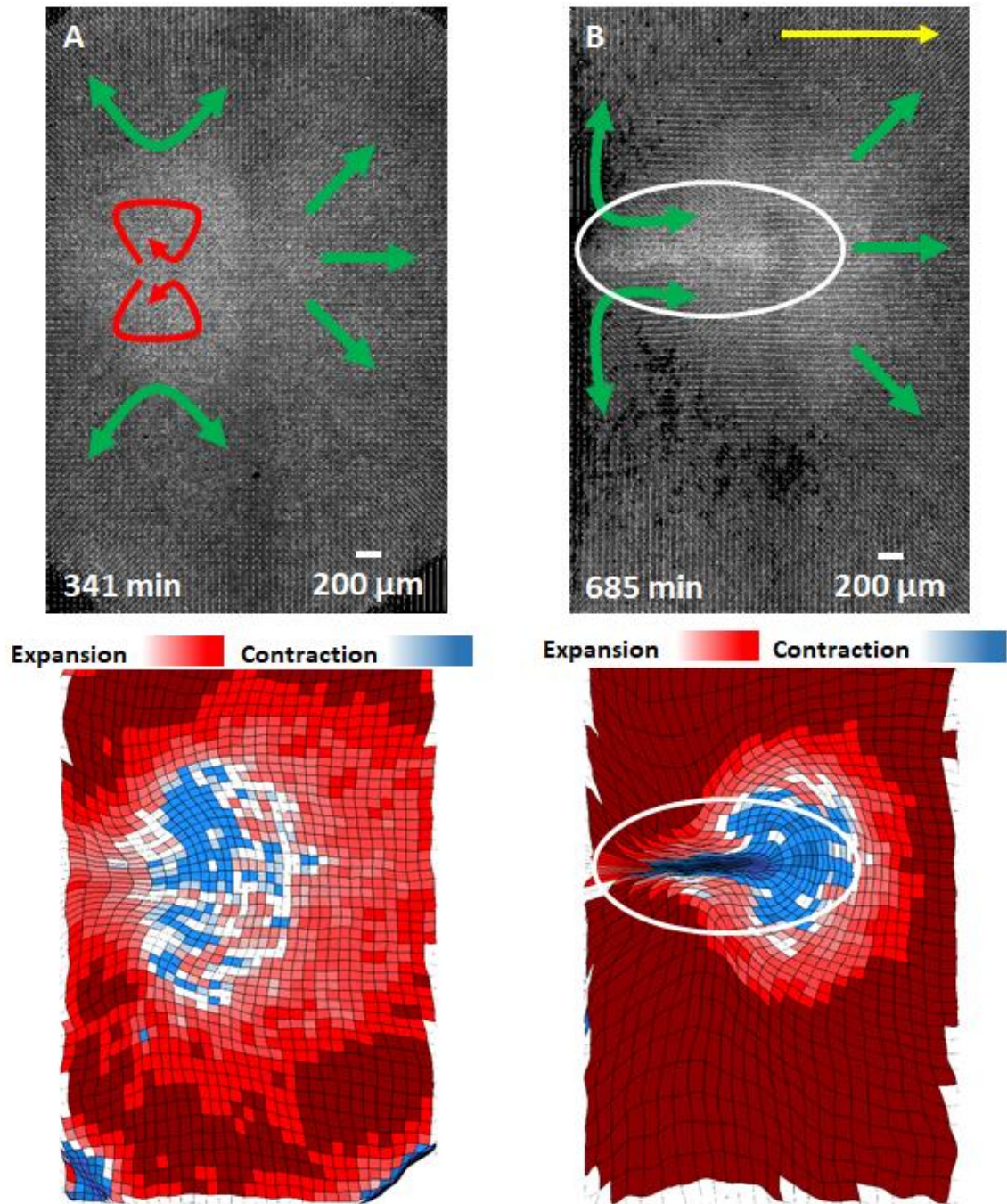


**Figure 3.15 Chick embryo epiblast surface PIV (top) and expansion-contraction maps (bottom).** Embryo epiblast surface images after 341 minutes **A)** and 685 minutes **B)** of live imaging. The white ellipse shows the primitive streak position. The red arrows indicate the epiblast characteristic flow prior to primitive streak formation. The green arrows show tissue flow directions, while the yellow arrow shows the Posterior → Anterior direction.

### 3.3. Dual colour DSLM

Biological systems are very complex, and the activity of some proteins might directly or indirectly affect the activity of other proteins. The observation of the



interaction of two or more proteins is a key factor for understanding their co-localisation and the existence of any correlation between them<sup>73,74</sup>. It will be highly advantageous to perform live imaging of specific protein dynamics in the context of the embryonic development, during crucial events such as gastrulation. This could take the form of monitoring the role of a protein A, which directly contributes to an increased or decreased action of a protein B, when cells are ingressing towards the streak furrow. Such an approach requires dual colour imaging.

The necessary changes in the microscopy system to perform dual colour images were made in both the optical set-up and the software. The set-up (Figure 3.16) was modified by: replacing the monochromatic laser with an air-cooled Krypton:Argon tuneable laser, provided by Melles Griot, model 643-RYB-A02, outputting three excitation wavelengths (488nm, 568nm and 647nm); and introducing a device called Optosplit II<sup>75</sup>, provided by Cairn Research, to orientate and split two emission wavelengths in parallel towards a single camera chip<sup>76</sup>.

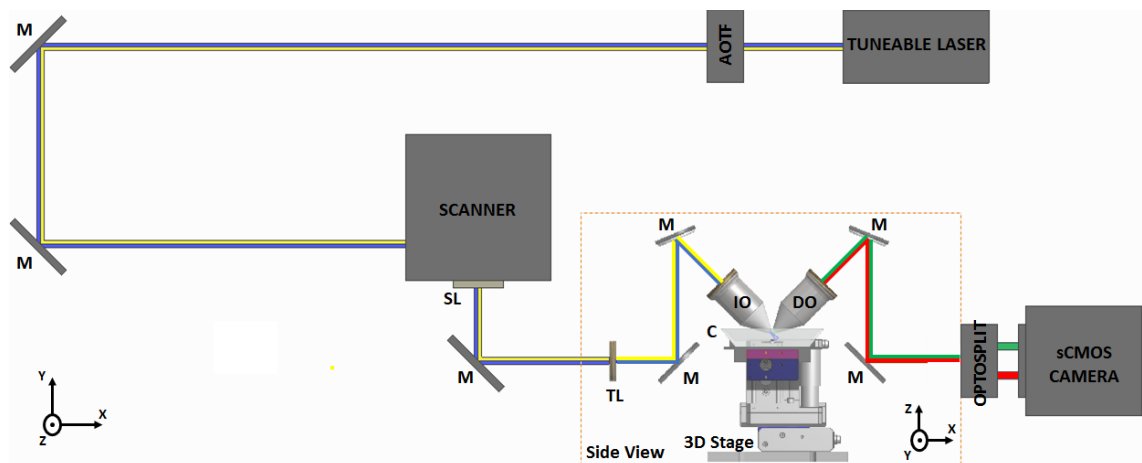


**Figure 3.16 Dual colour DSLM set-up.** Top and side views of the system. The laser is tuneable with three wavelengths: 488 nm, 568 nm and 647 nm; the AOTF working as a shutter can control the three wavelengths; M – Mirror; Scanner (composed of two galvo-mirrors) generates the light-sheet; SL – Scan Lens. On the side view: TL – Tube Lens; M – Mirror; C – Chamber; IO – Illumination Objective; DO – Detection Objective; 3D stage to position and move the sample; Optosplit, split the two emission wavelengths in parallel towards the sCMOS camera.

The Optosplit II optical set-up is schematically presented in Figure 3.17. This device is composed of: two anti-reflective achromatic doublet lenses; a dichroic mirror from chroma T565LPXR to split the wavelengths, wavelengths longer than 565 nm travel across the dichroic whilst wavelengths shorter than that are reflected; two filters from Chroma to block the unwanted wavelengths, a long pass filter with part number HQ615 for the wavelengths  $> 615\text{nm}$ , and a band pass filter for the wavelengths ranging 500-550 nm with a part number HQ525/50 M; and three mirrors, two dielectrically coated and one silver coated, to orientate the selected wavelengths to be output in parallel onto the camera chip. The device has a focussing ring available that allows the images to be focussed onto the camera chip.

Optical set-up configurations designed to split two different colour fluorescent signals imaged in the same camera chip have high chances of suffering chromatic distortions<sup>77</sup>. Even considering the images were collected from the exact same position in the sample, alternating between the two illumination wavelengths, chromatic distortion in the lenses affects the images perfect alignment and match, even for devices like the Optosplit II which incorporates two achromatic doublet lenses to correct it<sup>77</sup>.

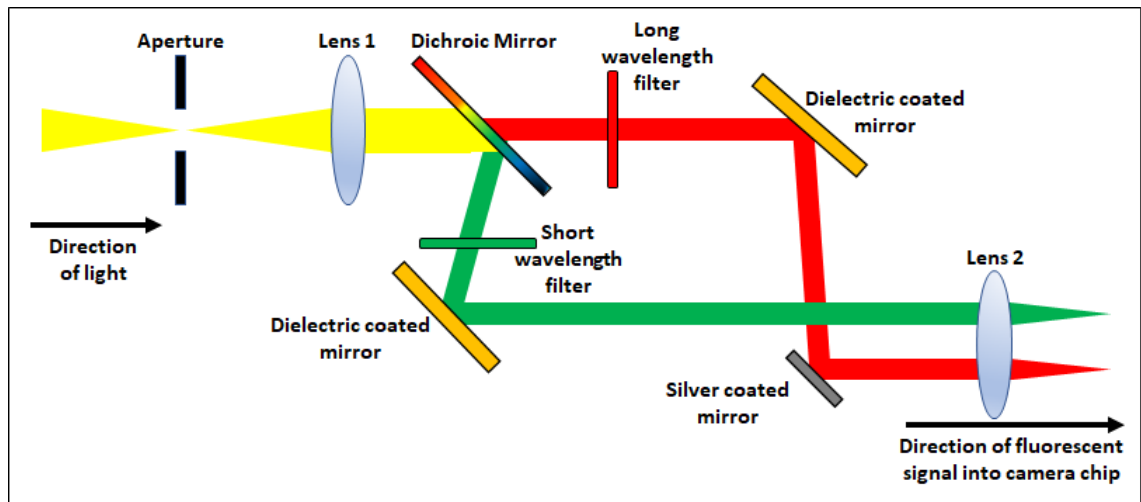


Figure 3.17 Scheme of the arrangement of the lenses, dichroic mirror, filters and mirrors inside the Optosplit II box.

Since for a single frame only  $2560 \times 400$  pixels are used in comparison to the  $2560 \times 2160$  pixels in the camera chip, two parallel images,  $2560 \times 800$  pixels, can be simultaneously or sequentially acquired with the same camera chip. The changes on the software were: the implementation of the necessary commands for the AOTF to control the three excitation wavelengths; the code programming definition of sequential and simultaneous modes of image acquisition; and the images post-acquisition processing and storage. During sequential mode the first wavelength illuminates the sample followed by the second wavelength, with the sample located in the same position before moving on to the next position. During simultaneous mode both illumination wavelengths are triggered at the same time to illuminate the sample. Both modes operate using step by step motion of the stage. After testing the simultaneous mode of acquisition it was noticed that both wavelengths are undesirably collected in both channels. Hence, the sequential excitation mode was the better option to optimise the fluorescent signal recorded from both wavelengths independently. This led to a complete separation of the spatial localisation of the two

fluorophores. The sample illumination wavelengths used were 488nm and 568nm to excite GFP and monomeric Red Fluorescent Protein mars<sup>78</sup> (mRFPmars), respectively.

Cairn Research provide an ImageJ dedicated plugin to split and align the images acquired with the Optosplit II. This is done through converting the images into RGB images and then overlaying these images and using the horizontal and vertical RGB profiles. This is possible because the images are taken from the exact same position for both illumination wavelengths and the field of view of the channels is the same.

### 3.3.1. Results

As a proof of concept and because, at present, a transgenic line of chick embryos expressing two fluorophores is not available, the microscope was used to image *Dictyostelium Discoideum* cells expressing MyosinII-GFP and LifeAct-mRFPmars, a construct that detects filamentous actin<sup>78</sup>. Figure 3.18 shows images collected in sequential mode for four hours of starved dictyostelium cells undergoing chemotactic aggregation. These are top view images of the cells sitting on top of agar, inside the rectangular chamber. The images result from the application of the code used to plot the chick embryo surface from the 3D stack on the dictyostelium acquired 3D data.

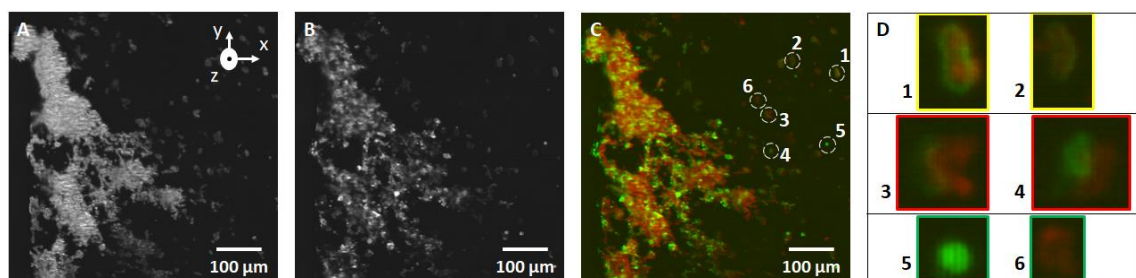


**Figure 3.18 Live images from *Dictyostelium Discoideum* acquired in dual colour sequential mode. A)** MyosinII-GFP channel; **B)** LifeAct-mRFPmars channel. **C)** Image outcomes from the alignment made from A and B, using the ImageJ Optosplit plugin. Red is MyosinII and Green is Actin. The numbers and the white dashed circles represent specific cells zoomed in and shown in figure **D)**. The numbers: 1 and 2 show two examples of channels with a perfect match; 3 and 4 show cases in which there is no perfect match of the two channels; 5 and 6 show cells which are only visible in one of the channels.

Figure 3.18 D show that upon alignment and overlay of the two channels some cells match and others do not match correctly, D – 1, 2 and D – 3, 4, respectively. The channel's mismatch may occur due to fluorophore localisation inside the cells at specific times of cellular development and behaviour or due to chromatic distortion.

Figure 3.19 show an example of RGB horizontal and vertical profile line plots, top and bottom plots, respectively. From the plots the differences in channel intensity is evident (red for MyosinII and green for Actin) with values range [0, 250]. A perfect match would mean perfect co-localisation of the fluorophores and variations in fluorescent signal intensity is expected since different fluorophores are used.

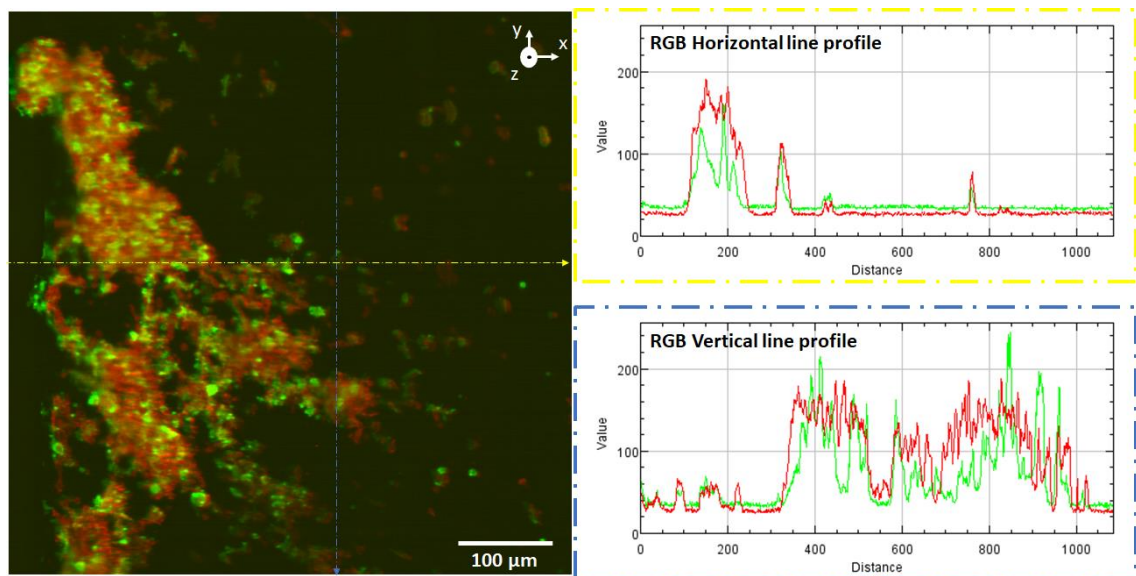


**Figure 3.19** Live Dictyostelium MyosinII and Actin fluorescent image, red and green, respectively. RGB horizontal and vertical profiles plotted within yellow and blue dashed lines. The profiles are measured left → right and top → bottom, for horizontal and vertical lines, respectively.

### 3.4. Discussion of results

Live imaging for tens of hours with frame rates  $\geq 24$  frames per second creates the opportunity to scan the embryo multiple times and leads to a considerable increment in the volume of data acquired when compared to a single scan. Although it was stated that a temporal resolution of 3 minutes between 3D stacks is sufficient to

image and follow gastrulation<sup>3</sup> using dual scan keeping the temporal resolution at 3 minutes, the data size increases from 500-600 GB to 1-1.2 TB. Thus, reaching a good compromise between going faster and producing a reasonable amount of data for live imaging the chick embryo early stages of development is desirable. The goal of speeding up the microscope acquisition process enough to cover 90-95% of the embryo whilst maintaining the spatial temporal resolution of 3 minutes is achieved by scanning two adjacent fields of view and stitching them together. Nevertheless, if required, instead of scanning the embryo twice, the embryo can be scanned multiple times at a higher frame rate, covering all the embryo and neighbouring regions and widening the imaged region to investigate processes beyond primitive streak formation. However, this is useful only if the aim is to investigate processes occurring beyond complete primitive streak formation, this comes with an extra cost of increasing the amount of data acquired.

Changes in the system set-up and software allowed multicolour experiments to be performed. In the future, a more careful registration of the two spectral channels is needed to quantify, and if necessary account for, chromatic aberrations in the optical setup. Then, the next natural step would be to use the system to investigate crucial protein activity inside the chick embryo during gastrulation using live imaging. This could be done by transfection or through the development of a new transgenic line expressing two or more fluorophores.

Imaging the hypoblast development with the DSLM microscope was very challenging, due to the need to mount the embryo with the forming hypoblast side up, facing the light-sheet. Normally the forming hypoblast faces the sub-germinal space, a small cavity between the hypoblast and the yolk filled with a small volume of fluid, with essential factors for its development. This contact is lost when the embryo is

cultured and incubated. Thus, it is very difficult to image the hypoblast at very early stages of development e.g. stage HH1, when the hypoblast is more fragile. The method used here for preparing, mounting and imaging the embryos, showed that hypoblast live imaging is successful for embryos at developmental stage HH2 or later. Hypoblast images acquired from embryos at these later stages show embryos developing normally according to literature description<sup>12,72</sup>.

The dynamics of the tissue flow in the hypoblast layer when the primitive streak is forming are not yet clearly understood. The streak furrow is visible in the epiblast with simultaneous movements of cells into the streak, with future mesendoderm cells displacing the hypoblast, most likely causing an expansion of the tissue at layers below the epiblast (Figure 1.2) due to EMT with a re-allocation of the cells in deeper layers and within the hypoblast. This central expansion strength decreases with the crescent distance from the streak furrow and the first contraction circle (Figure 3.14), possibly as a result of the counter reaction of hypoblast cells placed far from EMT regions. The second circular expansion region is caused by embryonic natural growth with the contraction resulting from the embryo limits (Figure 3.14). More research is required to establish a strong model and hypothesis for hypoblast development. The observations made in this report provide a good starting point and support the observation of events described in literature, like the scattered agglomerate of cells which will give rise to a flat layer of cells<sup>9,10,72</sup> and the central circular region<sup>71</sup>.

## 4. Cell ingress events using confocal line detection principle

High resolution images with high contrast will support the investigation of cell-cell mechanical and morphological behaviour in *in vivo* chick embryo development.

Biological live imaging with LSM, like most microscopy techniques, faces issues due to photon scattering and limited penetration depth. Scattering affects both image contrast and penetration depth of the illumination<sup>4,5,26</sup>. The penetration depth of the illumination is also dependent on the characteristics of the laser beam geometry used to generate the light-sheet. To increase imaging depth, refractive index matching optical clearing techniques have been suggested<sup>22,79</sup>. However, these techniques are not easily compatible with live imaging. Proposals for optimising penetration depth and image contrast in live imaging include the modulation of the Gaussian beam illumination into Airy or Bessel beams<sup>51,53,55,80,81</sup>, and using 2-photon illumination excitation mode<sup>6,38,60,82</sup>. On the detection side, as a means to improve the contrast if not the penetration depth, it is also possible to implement confocal line detection<sup>48,49,53,83</sup>.

The confocal line detection mode (CLDM) is a new feature on the most recent sCMOS cameras used in combination with DSLM set-ups<sup>48</sup>. To use this camera detection mode there are crucial changes and improvements to be made in the microscope software code.

### 4.1. CLDM implementation

The camera's CLDM enables synchronisation of the digitally scanned light-sheet with the exposure of a certain number of lines of pixels in the camera chip. This results



in high image contrast by minimisation of the contribution of the out-of-focus fluorescence and scattered light in the detection path. With CLDM working as an electronic slit, only the signal derived from the in-focus region passes through the slit, blocking the contribution of out of focus light in the acquired image.

In the DSLM microscope system the light-sheet is generated by a rapid movement of the laser beam, performed by the galvo-mirrors of the scanner. The laser beam is scanned across the sample. As a result, it is possible to synchronise the scanning of the laser beam with the exposure and readout of one or multiple rows of pixels in the camera chip while the light-sheet is being generated. Figure 4.1 illustrates the synchronisation of the laser illumination beam scanning with the exposure and readout of a single row of pixels in the camera chip during light-sheet formation. Only the row/s of pixels in synchrony with the laser illumination beam collect signals while the remaining rows, above and below, are disabled. This is the same as sequentially scanning the camera chip pixels row by row. Increasing the number of rows in synchrony with the laser beam will increase the signal received by the camera, effectively widening the electronic slit and reducing the image contrast. A correct balance between signal collected and number of rows of pixels in synchrony with the laser beam is required to guarantee collection of sufficient signal with optimal contrast.

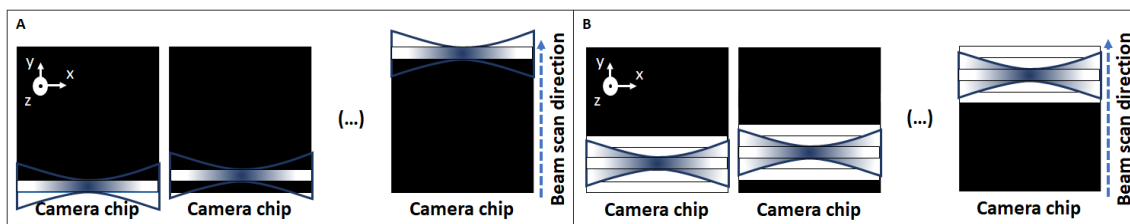


**Figure 4.1 Synchronisation between the scanned Gaussian laser beam and the camera chip A) 1 row of pixels and B) 5 rows of pixels exposure and readout at a time, during the light-sheet generation.** The three images in figures A and B show a sequence where the Gaussian laser beam, in blue, is synchronised with 1 and 5 rows of pixels bottom to top during beam scanning to originate the light-sheet. Note that even for 1 or 5 rows of pixels synchronised with the beam scanning the camera chip makes the exposure/readout row by row. This happens always, independent on the number of rows selected to synchronise with the Gaussian laser beam. When a row or rows of pixels is or are being exposed, the remaining rows, below and above, are deactivated (black region).

Due to system synchronisation issues, the initial frame size changed from 2560 \* 400 pixels to 2160 \* 640 pixels. This is because the camera CLDM works only by scanning the pixel rows along the shorter dimension of the camera chip.

The software changes implemented allow the user to input three camera CLDM parameters: the number of pixel rows to synchronise with the laser beam; the time to expose and readout each individual pixel row during beam scanning; and the number of delay pixel rows to begin the synchronisation. The number of pixel rows varies from 1 to 2160. The time to expose each pixel row ranges from 27.52  $\mu$ s to 100 ms. The number of delay pixel rows is used, if necessary, to facilitate a camera “standby” time up to the moment at which the laser beam is in parallel with the entered number of pixel rows at the beginning of the camera chip, to start the image exposure. All of these camera parameters are described in the camera user manual (Table 3-1). These parameter values must be selected in accordance with the scanner parameters, which set the laser beam scanning time. An incorrect set of values entered for the camera CLDM parameters will result in black images, because no fluorescent signal will be captured or, by chance, a fragmented image.

The hardware TTL communication between scanner and camera was changed, so that, once the scanner begins the camera is triggered to start the exposure. This is in contrast to the previous communication mode, where the scanner was starting and controlling the camera exposure time, i.e., whilst the laser beam scanning was operating, one camera was exposing from the beginning to the end. However, in a perfect CLDM synchronisation the camera total exposure time is equal to the laser beam scanning total time. To ensure that all the synchronisation is correctly performed the Oscilloscope described in the previous chapter was used.

#### 4.1.1. Results

The initial tests with CLDM began by synchronising 1 to 60 lines of pixels with the laser beam scanning and it was noticed that with a slit width of a single pixel row the images were very dark with very low fluorescent signal. The fluorescent signal did increase with the number of pixel rows, then with a slit width of 5 pixel rows the images were similar to the images acquired without the CLDM. Figure 4.2 shows chick embryo surface and cross-section live images, top and bottom images respectively, acquired without CLDM and with CLDM – 5, 10, 15, 30 and 60 Lines of pixels. These images were acquired using the same chick embryo at HH1 developmental stage.

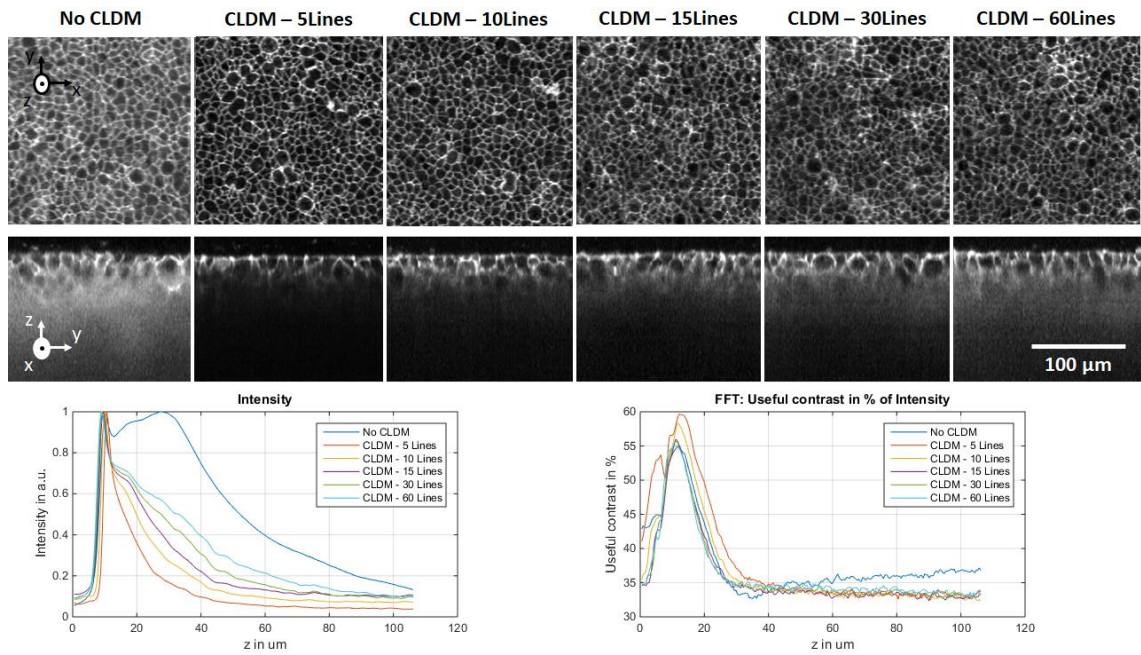


**Figure 4.2 Chick embryo at HH1 surface (top) and cross-section (bottom) images acquired, at 10x magnification, without CLDM and with CLDM - 5, 10, 15, 30 and 60 Lines of pixels synchronised with the laser beam scanning.** Below the images are the Intensity and Useful contrast graphs, dependent on embryo depth,  $z$ , in  $\mu\text{m}$ .

In Figure 4.2, the Intensity graph (bottom left) shows that increasing the number of pixel rows in synchrony with the laser beam scanning, approaches the intensity levels to the same as imaging the embryo without using CLDM. The Useful Contrast graph (bottom right) shows that the best image contrast is provided through using 5 pixel rows to synchronise with the laser beam, although it is only approximately 3% better than using 10 pixel rows and approximately 6% better than an image acquired without CLDM. As a result for images acquired with CLDM the beam was synchronised with 5 pixel rows. This corresponds to the use of an electronic slit with a width of  $3.25 \mu\text{m}$  and a length equal to the height of a single frame at 10x magnification.

There are two main disadvantages with using the sCMOS camera (Table3-1) in CLDM mode. One is that line sampling takes more time and for the sCMOS camera in use the frame rate is limited to 15 frames per second. Secondly as a natural consequence of the synchronisation between the camera's CLDM and light-sheet

generation, leading to the rejection of a considerable portion of the scattered light, most of the image signal comes from the focal plane of the light-sheet and this results in embryo deeper layers structural information loss (Figure 4.3).

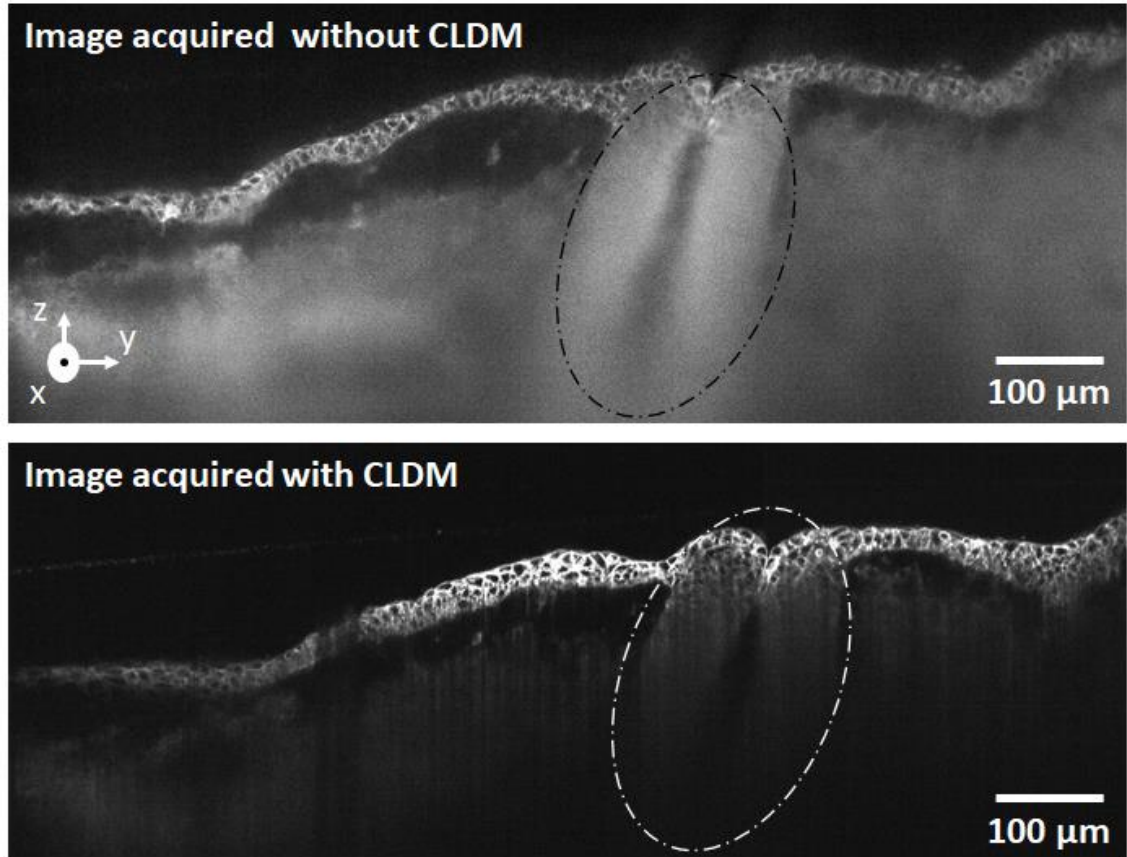


**Figure 4.3** Chick embryo at developmental stage HH6/HH7 cross-section images at 10x magnification acquired without and with CLDM, top and bottom images, respectively. The dashed black and white ellipses outline the embryo head fold region.

In Figure 4.3 the chick embryo head fold boundaries are better imaged without CLDM (region inside the black dashed ellipse) than imaged with CLDM (region inside the white dashed ellipse). With CLDM the image signal fades rapidly with depth (Intensity graph, bottom left, Figure 4.2). One way to resolve this is to scan the light-sheet over the sample twice per cross-section, i.e. two images per cross-section. In the first image the light-sheet focus is positioned at the embryo surface and in the second image the light-sheet focus is positioned slightly below the embryo surface. Then a single cross-

section image results from merging both images. As a natural consequence this would double the elapsed time between 3D stacks taking it above 3 minutes. As explained in the previous chapter a maximum of 3 minutes between 3D stacks is desirable to ensure that no important information is lost between 3D stack acquisition. This limited signal collection is more relevant for larger 3D samples such as chick embryos in later stages of development.

Figure 4.4 shows chick embryo at HH4 developmental stage cross-section images at 40x magnification, acquired without and with CLDM. Comparing the two images it is evident that the cross-section image acquired with CLDM provide more detail than the image acquired without CLDM, specifically the more turbulent region of image within the red dashed ellipses. Like the vesicles, inside the red dashed ellipses, that are visible on the image acquired with CLDM and not entirely visible on the image acquired without CLDM.

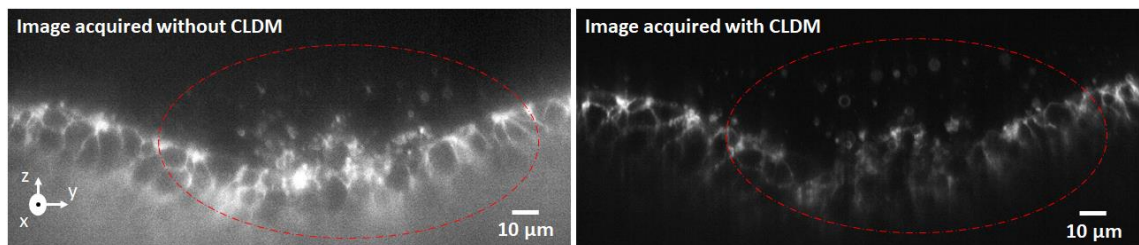


**Figure 4.4** Cross-section images from chick embryo, at 40x magnification objective, acquired without and with CLDM. Primitive streak furrow is confined inside the red dashed ellipses.

## 4.2. Epiblast cell ingression

The primitive streak formation marks the onset of gastrulation in mammals, reptiles and birds. The streak is the major site of ingression of epiblast cells<sup>1,3</sup>. Cellular ingression leads to EMT. Ingression is a complex cellular process which is probably controlled by chemical and mechanical cell-cell signalling<sup>1,3</sup>. A significant question is: how do these signalling reactions control cell behaviours responsible for cell ingression

and migration of future mesoderm and endoderm cells? A first step in these studies is a detailed characterisation of relevant cell behaviours. This is done by extensive time lapse imaging of cell ingress processes at high resolution. Without CLDM it was possible to detect cell ingress by the disappearance of cells from the embryo surface. However, it was difficult to follow details of this process due to the limited clarity of the cross-section deeper in the tissue. The cross-section images shown in Figure 4.4 clearly illustrate the enhanced detection of cell boundaries imaged with CLDM, due to the minimisation of the out of focus fluorescence and scattered light.

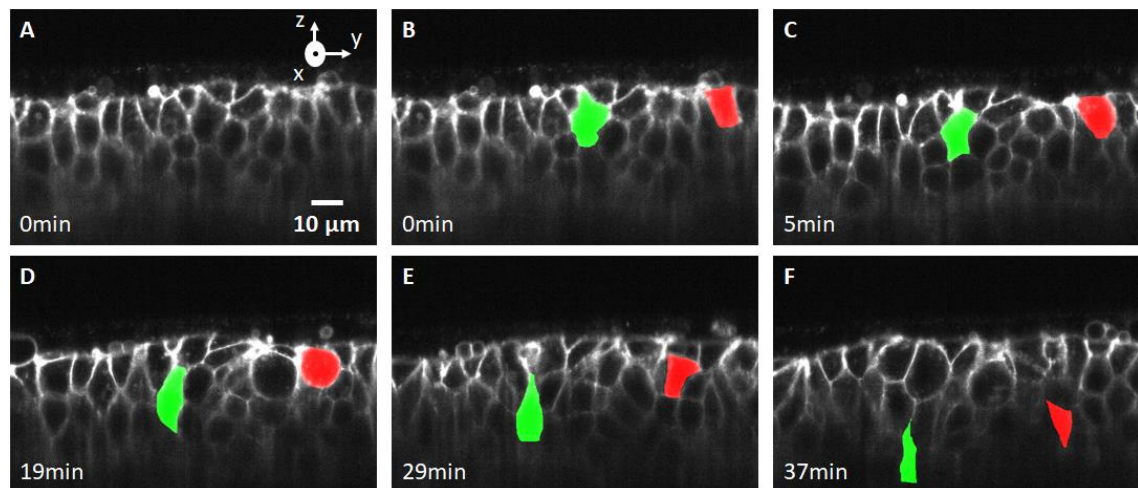


**Figure 4.5** Chick embryo cross-section images of two cell ingress events, in green and red. **A)** Chick embryo cross-section without false-colour overlay of tracked cells the cells. Images **B** to **F** show reshaping and movements of cell from the epiblast top to bottom layers.

CLDM allows tracking of the ingress of cells into the streak and neighbouring regions in detail. Figure 4.5 shows a sequence of cross-section images with two cells tracked for almost 40 minutes during their ingress from the embryo surface towards the future mesendoderm layer. Images shown represent sections acquired through the ingressing cells' middle region. As the cells reshape during the ingress process they become thinner once they start to move down<sup>3</sup>, but occasionally the cell apex might continue to be visible on the surface for some time. In Figure 4.6 the cell



ingression process is followed from both the embryo's cross-sectional and surface views. The event was recorded for 99 minutes, the time it takes for the cells to completely disappear from the embryo surface into embryo deeper layers.

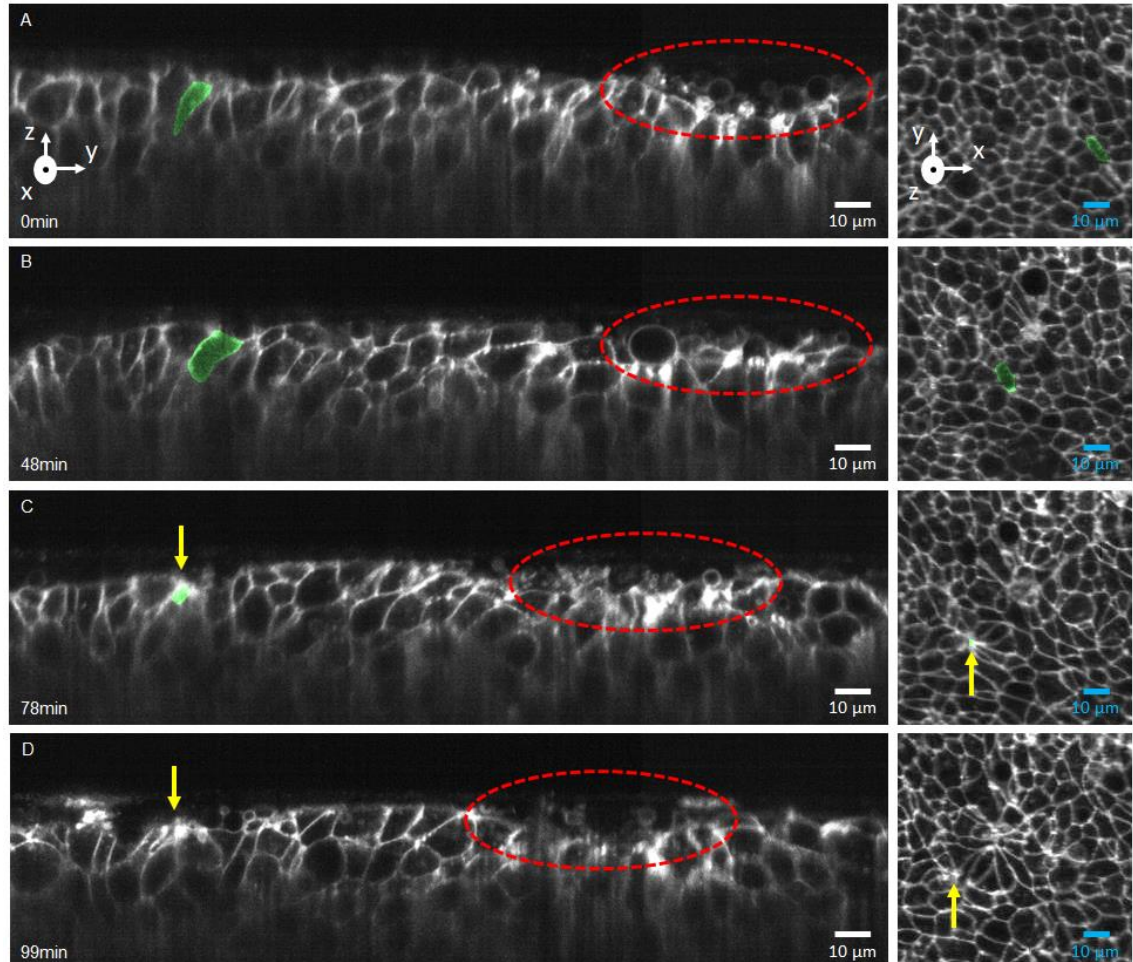


**Figure 4.6 Cell ingression event imaged over 99 minutes.** The cell is highlighted in green. The primitive streak is indicated by the red dashed ellipse. The yellow arrow points to the region at which the cell disappears and is no longer visible. From **A)** to **D)** the cell ingression is tracked in the embryo's cross-section and surface images, left and right images respectively. A considerable number of vesicles are sitting on top of the streaks.

### 4.3. Vesicles formed as part of cell ingression event

The images acquired with CLDM have greatly enhanced image sharpness and contrast. As a result, smaller structures such as vesicles sitting on the primitive streak and its neighbouring regions can be observed with much greater detail, Figure 4.7. Early stage embryos have very few vesicles on their surfaces. However, it was noticed



that vesicles appeared in considerable quantity on the top of the primitive streak during chick embryo developmental stage HH4.

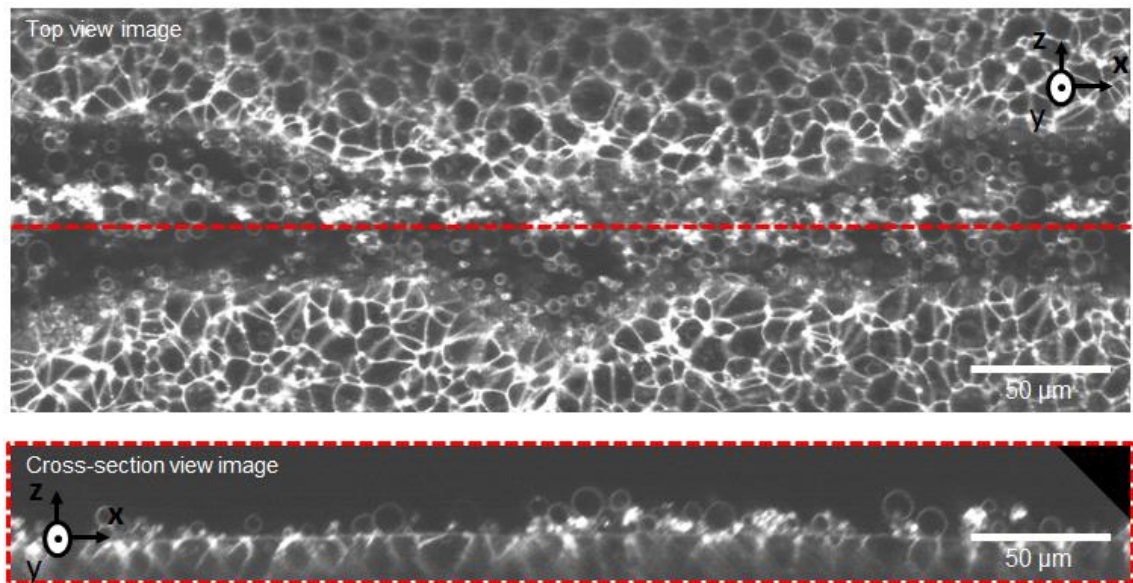


**Figure 4.7 Concentration of vesicles on top of the primitive streak, visualised on the 3D stack transformed volume.** Top image is the embryo's view at 12  $\mu\text{m}$  from the embryos surface. The bottom image is a cross-section image through the streak at the position indicated by the red dashed line in top view image.

This leads to the following questions: 1) What is the origin of the vesicles? 2) Do they arise as part of the cell ingression process and are they required for cell ingression to occur<sup>1,3,73</sup>? 3) Do they play a role in cell-cell signalling or are they a means to discard part of the cell such as the apical tight junction complex<sup>84</sup>, allowing the ingression event to occur?

The origin of the vesicles was investigated through looking carefully at the images acquired at 40x magnification with CLDM and these show evidence suggesting that vesicles may be a consequence of the cell ingression process, Figure 4.8.

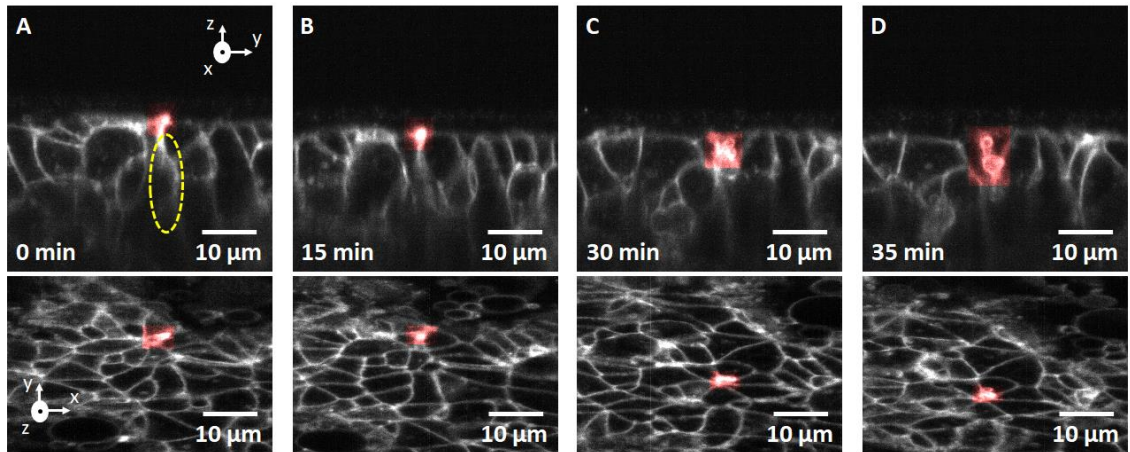


**Figure 4.8 Vesicle being formed as a consequence of cell ingression.** Vesicle formation indicated in red. Yellow circular dashed line indicates a cell connected to the vesicle. Sequence of embryo cross-section images showing vesicle formation beginning, after 15, 30 and 35 minutes of acquisition, **A**), **B**), **C**) and **D**), respectively. Bottom images represent the respective embryo's surface images.

Based on the acquired image observations, a hypothesis was proposed that these vesicles are formed as part of the ingression process during the rosette formation that occurs during cell ingression<sup>17</sup>. These structures form when the cell apex contracts, possibly with the help of neighbouring cells<sup>3</sup> (Figure 4.9).

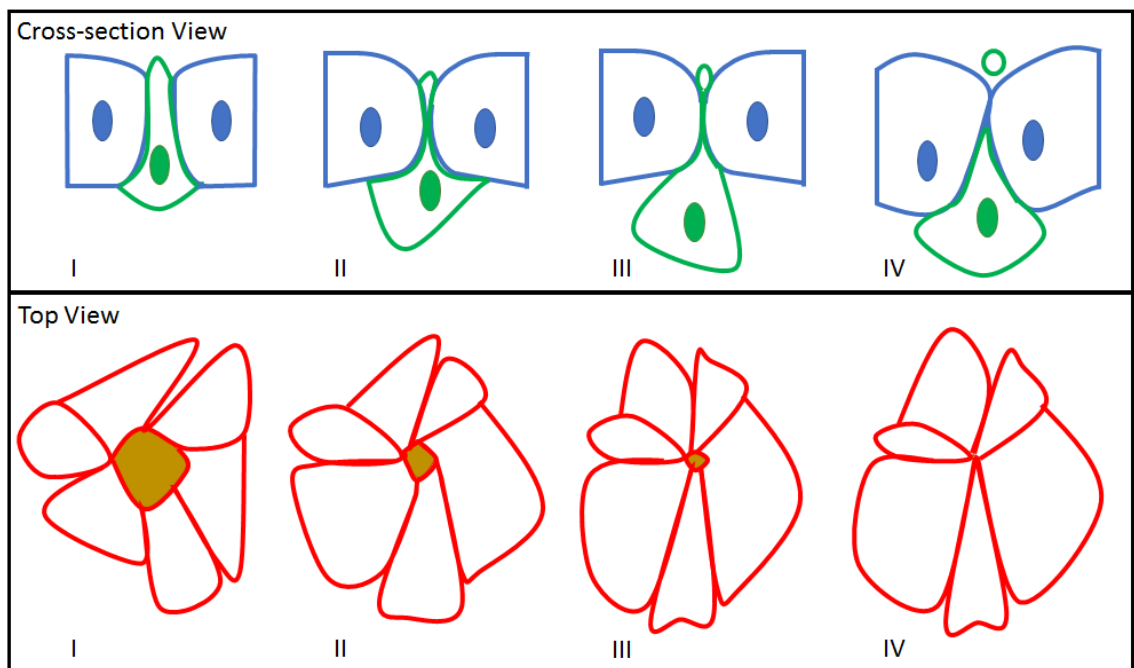


**Figure 4.9 Model explaining the vesicle formation and origin.** In the cross-section view (upper panels) the cell in green is about to ingress and part of the cell is abscised as a vesicle. During the abscission process the cell disappears completely from the surface (yellow cell in the lower top view panels).

The hypothesis presented in Figure 4.9 is based on the finding that vesicles are more concentrated in regions close to the streak groove, where most of cell ingression

events occur. These vesicles appear to have a wide range of sizes, as seen in Figure 4.7, they are generally circular and fluorescent. The fluorescent signal suggests that these structures were at some stage part of the cells, since in the transgenic chick embryos imaged during this project only the cell membranes express GFP.

Although the hypothesis proposed holds true for some cells it seems that not all cells forming the rosette near to the primitive streak complete the ingression. Figure 4.10 illustrates a vesicle formation looking at the embryo surface and corresponding to cell cross-section images. A cell is a 3D structure and as such the cross-section images were acquired from three distinct regions along the cell following the link between cell and future vesicle. It was observed that the cell cross-section is decreasing in size while the vesicle seems to increase in volume, Figure 4.10 C, without complete cell ingression.

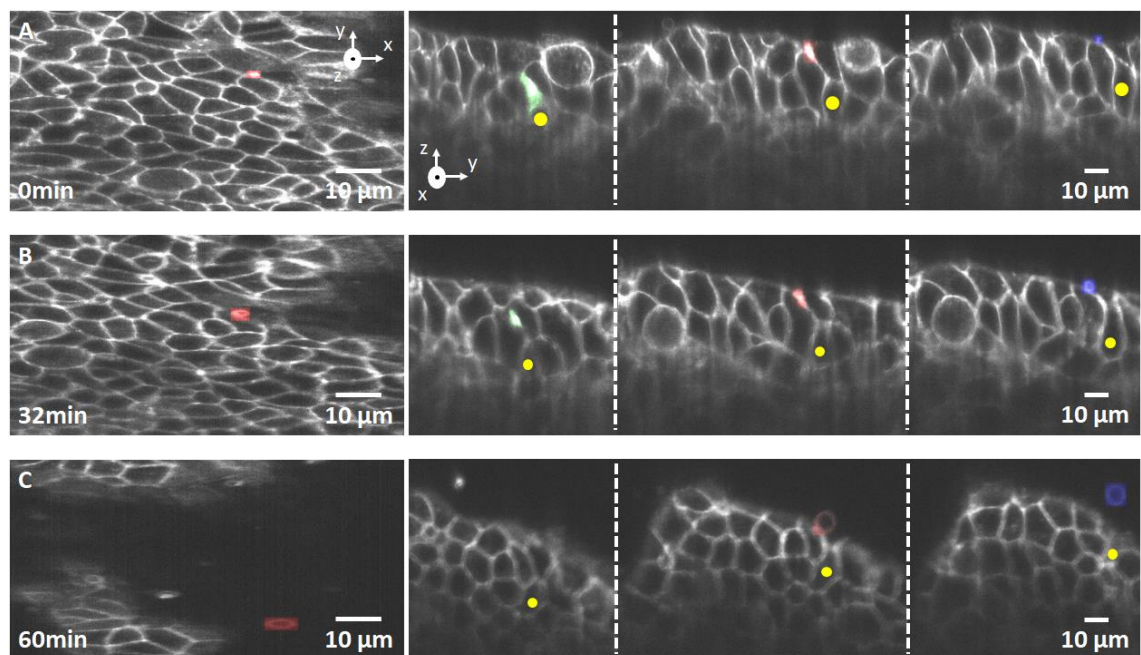


**Figure 4.10 Embryo surface and cross-section images during vesicle formation from epiblast cell.** Sequence of surface images on the left **A)**, **B)** and **C)** and its correspondent cross-sections on the right. The three cross-section images were acquired along the cell showing the cell - vesicle connection. The vesicle is marked in red on embryos surface images. On cross-section images, the yellow dot indicates the cell responsible for vesicle formation. Green, red and blue marks highlight the cell - vesicle connection.

When a cell prepares to ingress a rosette is formed. The fluorescent signal at the site of the rosette is relatively strong, caused by the fact that several cell membranes come together around the central ingressing cell. Cell ingress events are usually associated with the brightest spots in the acquired images, confirmed by the rosette structure formed by the cells. During the many observations performed, and following the vesicles near to the primitive streak region, it was evident that there are rosettes in which cells appear instead of being sites where cells ingress (Figure 3.10).

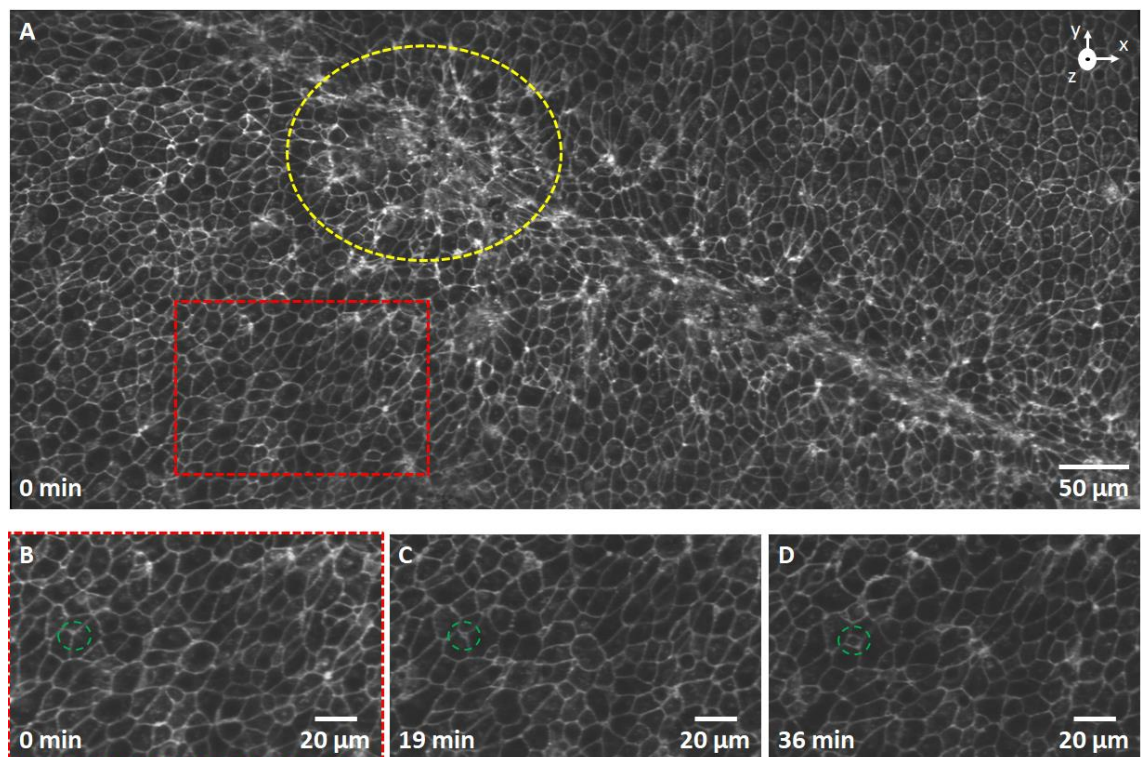


**Figure 4.11** HH4 chick embryo, rosette giving rise to a cell instead of finishing with a cell ingress. Image acquired at 40x magnification. **A)** Embryo surface, with primitive streak anterior tip surrounded by the yellow dashed circle. The red dashed square indicates the region in which the rosette is observed. Images with epithelial cells forming the rosette, indicated by the green dashed circle at the beginning of the acquisition, after 19 minutes and after 36 minutes, **B), C)** and **D)**.

In 48 rosettes tracked and followed, for approximately 75 minutes, on 4 embryos at developmental stage HH4 in regions very close to the primitive streak, approximately 80% result in cell ingress events, Table 3-1. While in the remaining 20% cells emerge from the rosettes to the surface. From the ingress events 92%



result in vesicle formation and from the emerging events 30% suggest that a vesicle originated from the process.

**Table 4-1 Cell ingress and emerging events observed in 48 cellular rosettes, counted in 4 embryos.** V indicates confirmation of Vesicle presence in the process. NV indicates confirmation of No Vesicle presence in the process.

Embryo 1				Embryo 2				Embryo 3				Embryo 4			
Ingressing		Emerging		Ingressing		Emerging		Ingressing		Emerging		Ingressing		Emerging	
6		4		11		-		8		-		13		6	
V	NV	V	NV	V	NV	V	NV	V	NV	V	NV	V	NV	V	NV
5	1	2	2	11	-	-	-	6	2	-	-	13	-	1	5

#### 4.4. Discussion of results

CLDM is without any doubt a valuable complement to LSFM, with a considerable improvement of image contrast as shown in Figures 4.2 and 4.3. These improved images allow tracking of individual epiblast cells during their transition to future mesendoderm cells. The low maximum frame rate limit (15 frames per second) makes it impossible to combine CDLM with the embryo dual scan method to cover a broader region on the embryo and will be more useful in the high-resolution investigation of cellular events in a smaller area.

Release of vesicles by cells, termed abscission, has been previously observed as a normal process during delamination of neuroblasts during neurogenesis in the neural tube<sup>84</sup>. The imaging of vesicles on fixed embryos was attempted without success, since practically all the vesicles sitting on the embryo's surface were washed away while carrying out the embryo fixation protocol. Origination of vesicles were observed in the HH4 embryonic developmental stage as part of and/or consequence of cell ingress. It is not yet clear whether this is the same as the abscission process described above or what its function is. It is necessary to determine what constituents are inside the

vesicles. The fact that the vesicles are fluorescent suggests that these vesicles were part of the cells, since chick embryos imaged are from a transgenic line with only the membranes labelled. This might be one of the reasons why this process is not well documented. Also, it was observed that a great majority of rosettes culminating with vesicle formation and cell ingression exhibit a very strong fluorescent signal. It was noticed that not all rosettes originate a complete cell ingression, a process already observed<sup>73</sup>, instead some cells come back to the surface. This finding suggests that cells located in the epiblast of the embryo might pull back cells that have already begun the ingression process or that some cells simply do not end up ingressing towards the embryo mid region due to further action-reaction forces on the tissue. For the future, a comprehensive analysis of the mesendoderm layers requires the development of suitable computational methods to segment and analyse the 3D cell shape changes associated with cell ingression events.

## 5. DSLM – Bessel beam and 2-photon illumination modes

Imaging with increased contrast and an increased penetration depth allows the tracking of cells flowing from the epiblast surface towards inner regions of the embryo, complementing and enhancing the 3D visualisation of cellular behaviours. Due to the independent orthogonal conjugation of the illumination and detection axes, LSFM offers numerous opportunities to improve and re-design both light-sheet and image detection methods/techniques. As discussed previously, two major issues affecting image quality in microscopy are scattering and penetration depth<sup>4,5,26</sup>. With CLDM the scattered light, as contributed by out of focus regions along the illumination path, is strongly minimised in the images, resulting in images with increased contrast. In this chapter, changes are made to the microscope to improve the imaging optical penetration depth. To improve penetration depth, two techniques with promising results, as described in literature, are used. First, a beam shaping technique is applied to modulate a Gaussian beam into a Bessel beam<sup>51–53,55,58,81,85,86</sup>. Secondly, further optical changes are performed and a multiphoton laser is used to apply a 2-photon excitation<sup>18,38,60,61,87,88</sup> into the transgenic chick embryos expressing a membrane targeted GFP. Although not used here, both techniques can be combined into 2-photon excitation Bessel beams<sup>89</sup>.

### 5.1. Bessel beam light-sheet DSLM

There is a considerable body of papers detailing the effects of Bessel beam light-sheets and their impact on imaging quality<sup>81,86,89</sup>, however there is a lack of information detailing their performance and use in live imaging of real tissues. Therefore, in this research, so that the benefits of Gaussian and Bessel beams on live

imaging of chick embryos could be seen, it was crucial to use for each beam the parameters that would provide the best image contrast, resolution, depth of focus and penetration depth. When compared to other embryos such as *C. Elegans*<sup>23,87</sup>, Zebrafish<sup>51</sup> or *Drosophila*<sup>56</sup>, chick embryos are a lot larger and structurally more complex, giving rise to an increased challenge. Moreover, the chick embryo surface is initially flat but in time becomes highly irregular and, additionally, the embryo medium is highly scattering. Therefore, the chick embryo provides a good test for Bessel reputed increased focus and penetration depth.

In this project an SLM was used to modulate the Gaussian beam into a Bessel beam. The main reason for using a SLM resides in its flexibility and versatility for outputting quasi-Bessel beams. Additionally, producing the Bessel beam with an annulus results in blocking most of the illumination light, since only a portion of the light pass through the annular slit. With the axicon some suggest that it produces a Bessel beam with variable axial intensity, while the SLM produces a Bessel beam with uniform axial intensity<sup>85</sup>. Thus, an SLM was introduced to the system to modulate the Gaussian beam into a Bessel beam (Figure 5.1). There is a secondary optical pathway for the Gaussian beam, allowing direct comparison between the two illumination modes. Although, the SLM could be used to output a Gaussian beam<sup>56</sup>, the aim here is to compare the Bessel images with the images acquired with the original system illustrated in Figure 3.2.



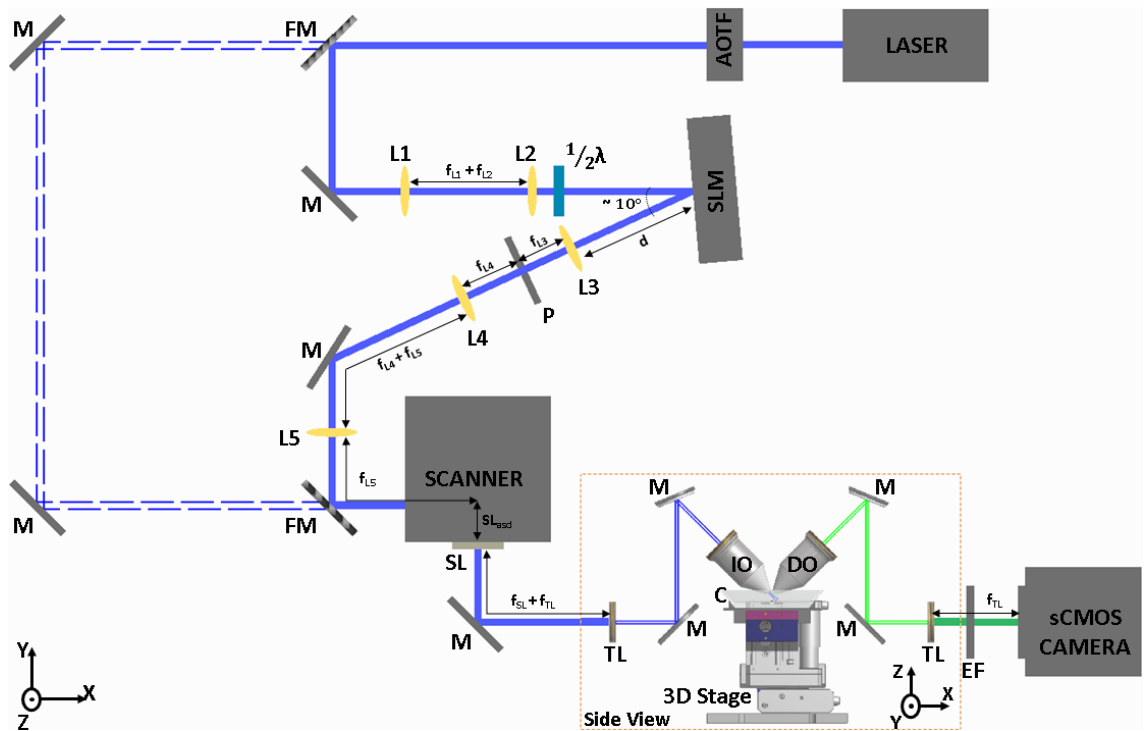


**Figure 5.1 DSLM with Gaussian and Bessel beam illumination paths.** Optical setup top view, with sample holder, illumination and detection objectives in side view. The Blue filled line and the blue dashed lines represent the Bessel and Gaussian illuminations pathways, respectively. The laser is a monochromatic, 488nm. AOTF – Acousto-optic tuneable filter. FM – Flip mirror. M – Mirrors. L1 to L5 – Achromatic doublet lenses.  $\frac{1}{2}\lambda$  – Half-wave plate. SLM – Spatial light modulator. P – Pinhole. SL – f-theta scan lens. TL – Tube lens. IO – Illumination objective. C – Sample chamber. DO – Detection objective. EF – Emission filter.  $f_{L_i}$ ,  $i=1, \dots, 5$ , are the lenses focal lengths,  $d$  is the distance between the SLM and L3 ( $\sim 100$  mm) and  $SL_{\text{asd}}$  is the SL rear edge aperture stop distance. The distance from each TL to the corresponding IO/DO is 200 mm.

The microscope software commands and hardware connections are not changed from those used in chapter 3. In the set-up, the laser beam passes through the AOTF which acts as a shutter preventing unnecessary illumination of the sample when no images are being acquired. Flip mirrors are used to switch between Gaussian and Bessel beam optical paths. For Gaussian illumination, the beam goes directly to the scanner. For Bessel illumination, the Gaussian beam, 0.7 mm diameter, is expanded with a telescope (10x) to overfill the SLM's display, 7.36 mm \* 7.36 mm, and its polarisation is adjusted with a half-wave plate. To modulate the Gaussian beam into a Bessel beam the SLM displays a conical phase mask with an added linear phase shift. For light phase modulation in off-axis regime according to Meadowlark, the SLM is placed with an

angle of approximately  $10^\circ$ . The conical phase slope applied defines the Bessel beam central core and depth of focus<sup>56</sup>. The added linear shift will provide the separation between the hologram desired Bessel pattern and the hologram diffraction background due to SLM chip pixellation<sup>56</sup>. The system is shown in Figure 5.1 and L3 images a ring correspondent to the SLM's far-field diffraction pattern. As a result of L3 movement the ring dimensions could be altered, thus to avoid undesirable changes of the beam the position of L3 is fixed at a certain distance from the SLM, smaller than L3 focal length<sup>56</sup>, in the system from Figure 5.1 the distance is approximately of 100 mm. The zero-order diffraction pattern from background, caused by SLM display pixellation, and higher-order diffractions are blocked with a pinhole, P, placed in the focus of L3. The ring is then imaged onto the scanner with a 6x telescope to fill the entire illumination objective back aperture, and produce a Bessel beam with short depth of focus, or with a 2x telescope achieving a Bessel beam with longer depth of focus. An  $f$ - $\theta$  scan lens, a tube lens and the illumination 10x magnification objective, are used to generate and deliver the light-sheet into the sample. The resulting fluorescent signal is acquired through another 10x or a 40x magnification objective and a tube lens. The fluorescence signal passes through an emission filter and is recorded by the sCMOS camera. All the details related to the new devices and parts used in the Bessel pathway, system from Figure 5.1, are described in Table 5-1.

**Table 5-1 Devices and parts used in DSLM Bessel pathway, illustrated in Figure 5.1.**  $\lambda$  – Wavelength, F – Focal Length.

<b>Devices / Parts</b>	<b>Company</b>	<b>Part Number</b>	<b>Specification</b>
L1	Thorlabs	AC254-040-A-ML	F = 40 mm
L2	Thorlabs	AC254-400-A-ML	F = 400 mm
$1/2\lambda$	Thorlabs	WPH10M-488	$\lambda = 488$ nm
SLM	Meadowlark	P512-0532	512 * 512 XY Nematic SLM Display window dielectric coating $\lambda$ : 450-865nm
L3 (Option1)	Thorlabs	AC254-150-A-ML	F = 150 mm
P	Thorlabs	SM1D25	Diameter: 0.8 – 25 mm
L4 (Option 1)	Thorlabs	AC254-050-A-ML	F = 50 mm
L5 (Option 1)	Thorlabs	AC254-300-A-ML	F = 300 mm
L3 (Option2)	Thorlabs	AC254-200-A-ML	F = 200 mm
L4 (Option 2)	Thorlabs	AC254-150-A-ML	F = 150 mm
L5 (Option 2)	Thorlabs	AC254-300-A-ML	F = 300 mm

In table 5-1, Option1 and Option2 for the lenses L3, L4 and L5, refer to the configurations to completely fill the illumination objective back aperture or not, respectively. The images acquired with Bessel illumination shown in the following pages were acquired using the lenses Option1 configuration, with the illumination objective back aperture completely filled.

The Bessel beam profile exhibits an extended focus and a central core surrounded by several rings, or side lobes, whose contribution degrades image quality (Figure 5.2, maximum intensity projection images and beam profile cross-section images acquired at the beam focus).

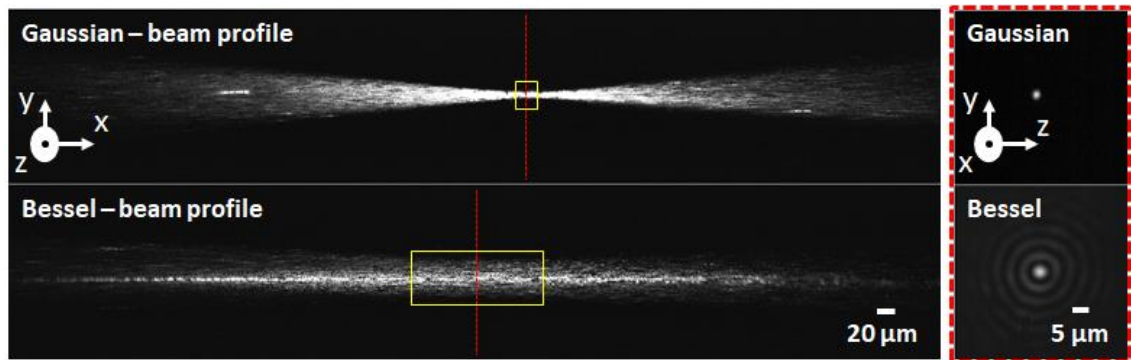


**Figure 5.2** Gaussian and Bessel beam maximum intensity projections (MIP) of  $z$  stacks taken inside a volume of beads, prepared according to section 2.4 of this document, (left) and the beams respective cross-section profiles (right) acquired after using a mirror placed at the illumination objective focus. The red dashed lines represent the region at which the cross-section profile image were acquired. The yellow boxes represent the beams focus range. The side lobes from the Bessel beam are visible on the cross-section image.

To minimise side lobe contribution and thus increase Bessel image sharpness, synchronisation between light-sheet generation and the camera via CLDM was implemented. For instance, solely by imaging the Bessel light-sheet with CLDM (Bessel CLDM) the contribution from the side lobes is greatly decreased, Figure 5.3.

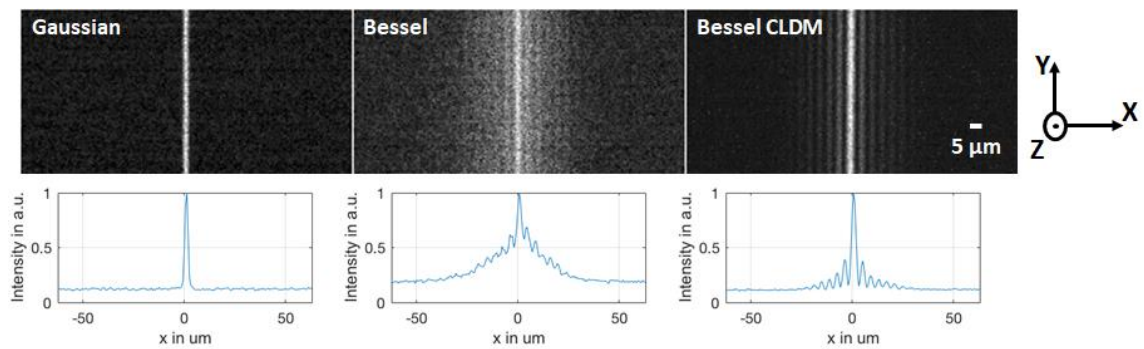


**Figure 5.3** Gaussian, Bessel and Bessel CLDM light-sheet images (top) acquired after using a mirror placed at the illumination objective focus and their respective intensity profile graphs (bottom). The images were acquired after reflecting the light-sheet waists on a mirror.

Using the camera CLDM the electronic confocal slit dimensions were kept the same as those presented in the previous chapter (4), a width of 5 lines of pixels or  $3.25 \mu\text{m}$  and a length equal to the height of a single cross-section image.

As it was stated previously, the Gaussian and the Bessel beams were optimised to provide the best images possible. The Gaussian beam was set to give the chick embryo's surface top layer good images, i.e. a beam with 2.2  $\mu\text{m}$  full width at half maximum (FWHM) and 45  $\mu\text{m}$  depth of focus. A Bessel beam with the same Gaussian central core width would have a depth of focus of 100  $\mu\text{m}$  at FWHM. However, this increased depth of focus of the Bessel beam did not cover the chick embryo cross-section image field of view. Additionally, the image signal degrades with depth. As a result of the above, the Bessel beam depth of focus was increased up to approximately 650  $\mu\text{m}$  with a central core width of 5.7  $\mu\text{m}$  at FWHM, covering the entire field of view and providing chick embryo surface images with the same details of an image acquired with the short Bessel beam. In comparison, a Gaussian beam with a depth of field of approximately 650  $\mu\text{m}$  would have a central core width of 8.4  $\mu\text{m}$ , and the beam would diverge as it propagates. Therefore, the Bessel beam was used with a depth of focus of approximately 650  $\mu\text{m}$  which increased the chance of seeing a broader region of the chick embryo deeper layers, with the embryo surface being imaged with acceptable detail. The Gaussian beam used has a width of 2.2  $\mu\text{m}$  at FWHM, since widening the depth of focus would lead to an increased beam waist, lowering image resolution and enhancing background signal, degrading the image contrast.

To complement the image analysis, Bessel CLDM images were deconvolved (Bessel CLDM Dec.). Deconvolution is used in microscopy to improve image sharpness<sup>67,90</sup> and is a useful post-acquisition technique for images acquired with non-diffracting beams<sup>51,89</sup>, for side lobe contribution minimisation. The Richardson-Lucy deconvolution model was used to deconvolve the images. The image processing and deconvolution software was implemented in Matlab<sup>66,67</sup>. The Gaussian images were also deconvolved, although no improvement was noticed in the resultant images. As a

result, this was not implemented further during the Bessel and Gaussian performance in chick embryo live imaging.

From measurements performed in the sample plane the Bessel illumination requires approximately five times more intensity than Gaussian to achieve the same image intensity.

### 5.1.1. Results

Live imaging of chick embryos at different developmental stages<sup>13</sup> HH1, HH3 and HH5 were performed, using Gaussian, Bessel and Bessel CLDM (Figure 5.4 A). Approximately 20 minutes separated the images acquired with different modes. The embryo's surface was extracted from the 3D data followed by segmentation to obtain key information about epiblast cell behaviour and dynamics during gastrulation. Segmentation was executed using a watershed algorithm<sup>3</sup> and performed in a region composed of 450-700 cells for all three stages of development (Figure 5.4 C). Accordingly, a manual count was made on the segmented cells and the segmented errors were obtained (Table 5-2). The segmentation errors were divided into two categories: over-segmentation, when a cell is segmented to include one or more cells; under-segmentation, when the segmentation fails in segmentation of an individual cell (Figure 5.4 B). The error percentages are achieved by dividing the number of errors, for over and under-segmentation, by the total number of cells manually determined in the segmented region. The errors shown in these mistakes measurements are obtained from the standard deviation calculations made from the readings.

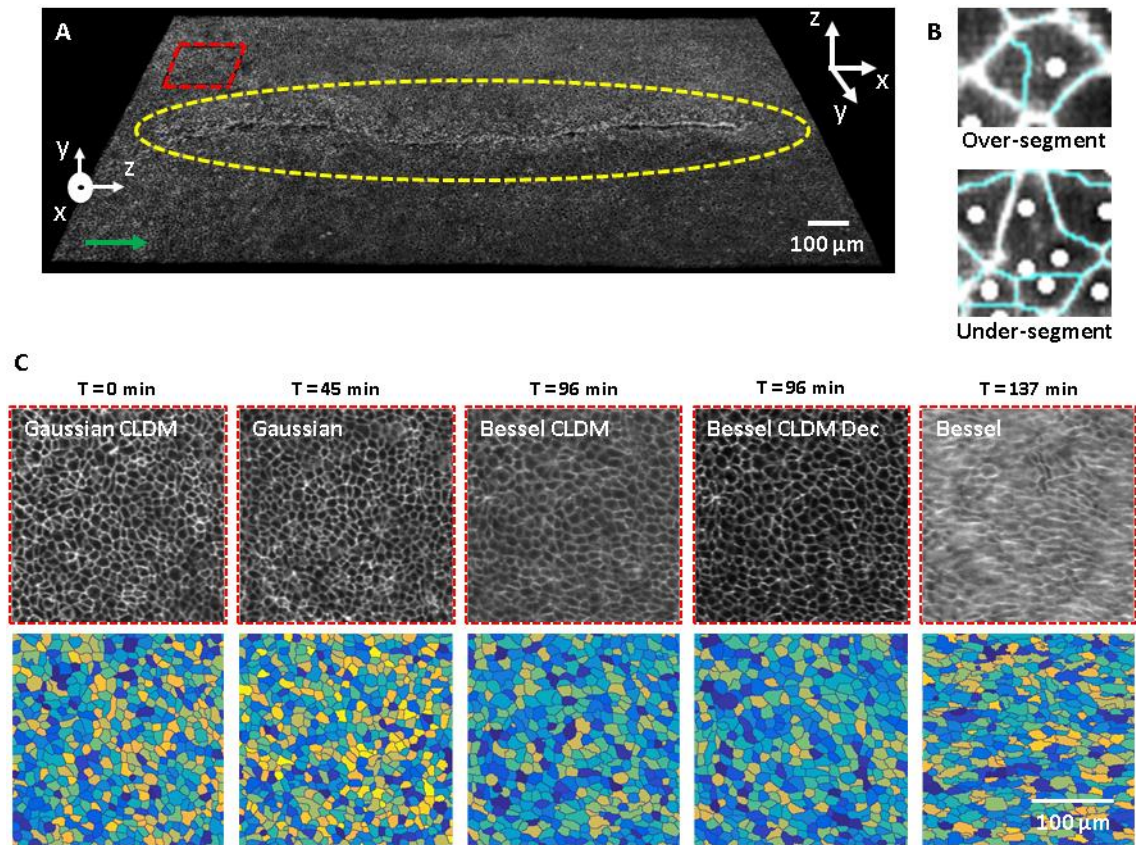


**Figure 5.4** Chick embryo surface imaged at 10x magnification objective using Gaussian and Bessel light-sheet illuminations, with and without CLDM, and surface segmentation results. **A)** HH3 embryo icy rendering surface imaged with a Gaussian light-sheet. Yellow dashed ellipse indicates primitive streak location. The red dashed frame indicates the embryo region at which segmentation was performed. The green arrow indicates the Posterior-Anterior direction. **B)** Over-segmentation and under-segmentation errors examples. The white dots represent cell centroids. The blue lines indicate the segmented membrane. **C)** The top images, show the embryo surface imaged by: Gaussian, Gaussian CLDM, Bessel and Bessel CLDM. The last image shows the deconvolution of Bessel CLDM image. The bottom images, randomly coloured, show corresponding surface segmentation results. T represent the acquisition elapsed time between the first illumination mode used, Gaussian CLDM, and the other illumination modes.

**Table 5-2 Embryo surface segmentation errors counted manually.** Os – Over-segmentation, Us – Under-segmentation. NA – Not Applicable.

	HH1		HH3		HH5	
	Os	Us	Os	Us	Os	Us
Gaussian	3.6 ± 1.0 %	3.5 ± 0.9 %	3.2 ± 0.3 %	2.8 ± 0.4 %	0.3 ± 0.2 %	0.7 ± 0.5 %
Gaussian CLDM	2.8 ± 0.0 %	2.5 ± 0.5 %	2.4 ± 0.0 %	2.3 ± 0.5 %	0.7 ± 0.1 %	1.1 ± 0.4 %
Bessel	NA	NA	NA	NA	NA	NA
Bessel CLDM	5.5 ± 0.4 %	5.9 ± 1.8 %	5.9 ± 2.7 %	5.5 ± 0.7 %	5.2 ± 0.1 %	6.3 ± 1.5 %
Bessel CLDM Dec.	2.7 ± 0.1 %	3.1 ± 0.4 %	3.1 ± 0.1 %	4.0 ± 0.5 %	3.3 ± 0.8 %	4.7 ± 0.0 %

The cell membranes are clearly visible with high contrast for both Gaussian modes. Segmentation results are slightly better with CLDM with images showing reduced blur. The basic raw Bessel image resolution and contrast is too poor for good segmentation, consequently CLDM becomes essential for Bessel illumination imaging. Segmentation of the Bessel CLDM images revealed results slightly different from the ones presented by the two Gaussian modes. Deconvolving the Bessel CLDM images resulted in image sharpness and contrast improvements, bringing segmentation results closer to Gaussian modes for HH1 and HH3 embryos.

More experiments and further analysis to assess the benefits of Bessel illumination in deeper layers of the chick embryos were performed with the aim of imaging cell ingress events and following cells below the epiblast. Segmentation results for a portion of the cross-section images are improved by CLDM (Figure 5.5 A). Both Gaussian illumination mode segmentation results appear more reliable than segmentation made on any of the Bessel illumination modes, although a segmentation of the complete epiblast cross-section layer was not possible in any of the modes. As a result of the image contrast degradation at depth complemented by the weakness of the fluorescent signal after traveling through a few layers of cells, it is not possible to clearly see the epiblast bottom layer. Due to the electronic slit, Gaussian CLDM and Bessel CLDM modes reduce the considerable blur and fuzziness of the images, and the Bessel CLDM deconvolved image shows an enhanced contrast compared to Bessel. This is verified by the left hand graph plotted in Figure 5.5 B, where a fast intensity decay for Gaussian CLDM and Bessel CLDM deconvolved indicate an enhanced sharpness when compared to the other modes. This metric measures the intensity on the embryo's surface cross-section images as the function of depth. The second metric, shown on the plot on the right side of Figure 5.5 B, quantifies the useful contrast



ratio<sup>38</sup>. This ratio was computed for a 3D stack portion of the embryo at HH3 (cross-section images in Figure 5.5 A). The plot on the right-hand side of Figure 5.5 B shows that for all modes at the same depth higher contrast is provided by Gaussian CLDM and Bessel CLDM deconvolved. This is evidence that these modes show good resolution of structures inside the deeper layers of the embryo.

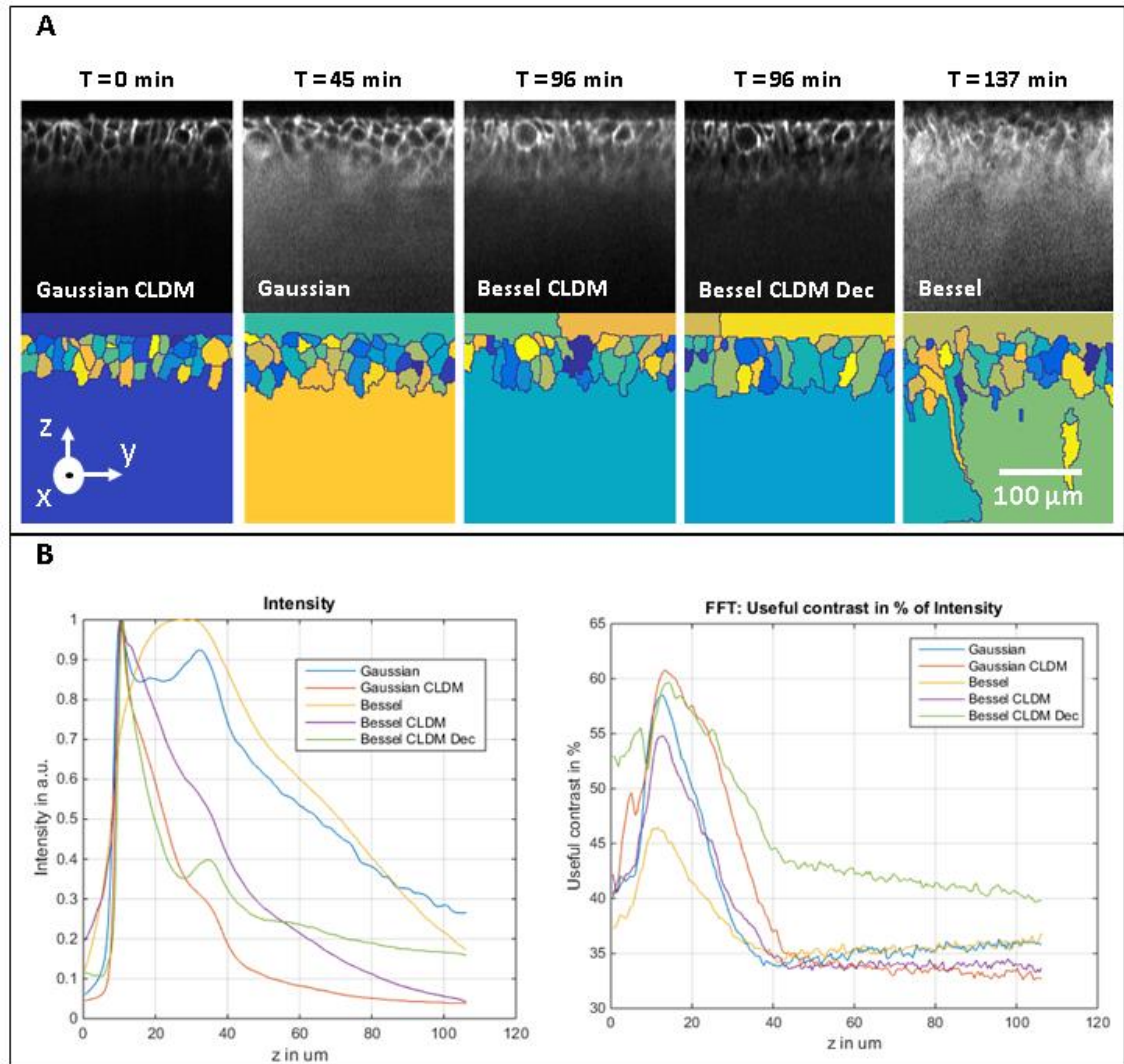


**Figure 5.5 HH3 embryo cross-section images acquired with Gaussian and Bessel illumination modes, their segmentation results and the Intensity and Useful contrast plots. A)** Top images are the embryo's cross-section images of the thick cell layer close to the primitive streak, imaged at 10x, acquired by: Gaussian, Gaussian CLDM, Bessel and Bessel CLDM. The last image shows the deconvolution of the Bessel CLDM image. Bottom images, randomly coloured, show the segmentation results. **B)** Graphs representing the images signal intensity and useful contrast as function of the penetration depth. T represents the acquisition elapsed time between the first illumination mode used, Gaussian CLDM, and the other illumination modes.

In addition to the earlier stage embryos, up to HH3, embryos at a later developmental, HH10, were imaged, as can be seen in Figure 5.6.

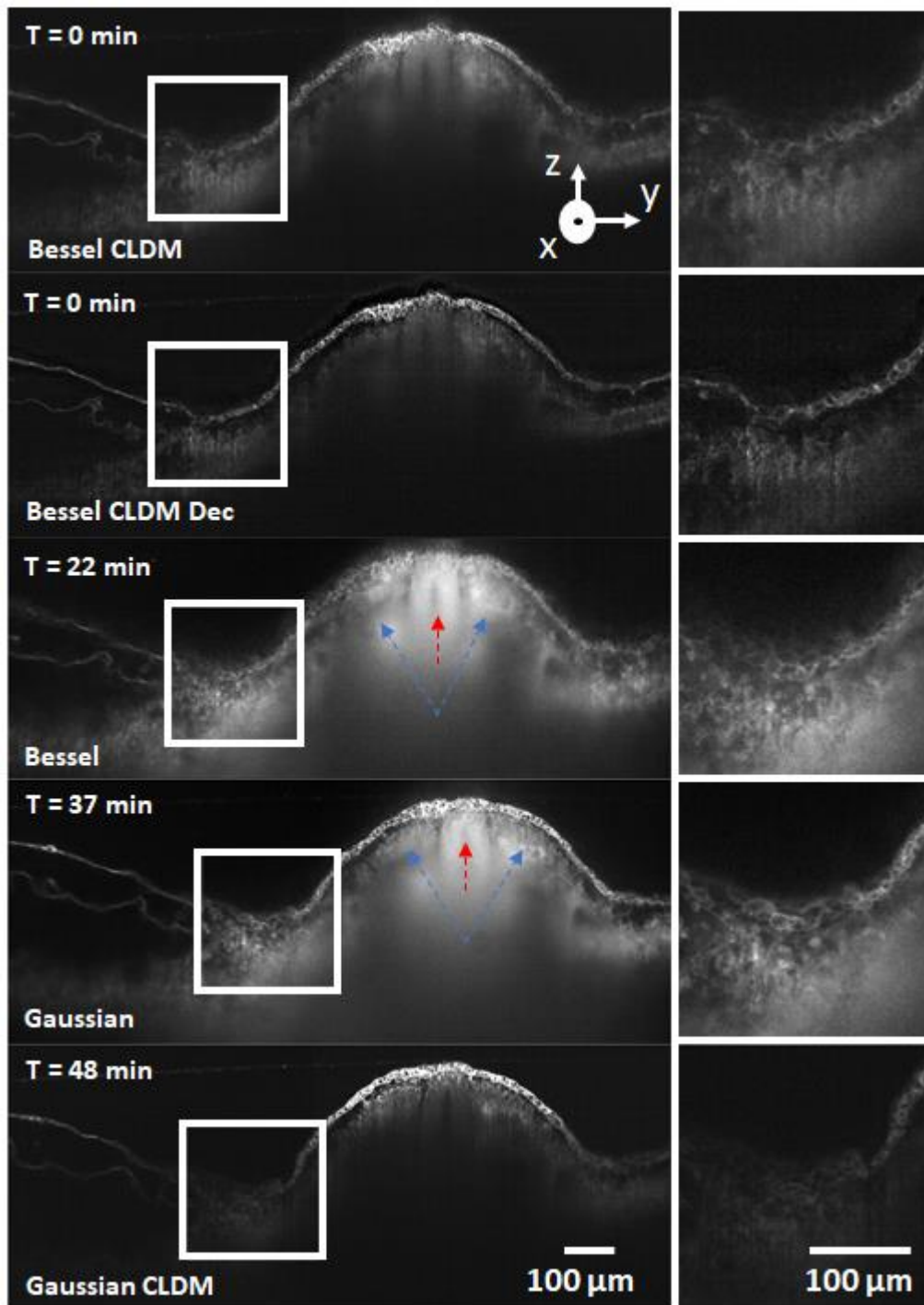


**Figure 5.6 Cross-section images from a HH10 developmental stage embryo.** The images were acquired by Gaussian and Bessel illumination modes at 10x magnification objectives. The embryo's future neural tube and somites are indicated by the red and blue dashed arrows, respectively. The white square in the left-hand images is zoomed out on the right-hand images, the region highlights the cellular structural complexity of the embryo at later stages of development, e.g. HH10. T represents the acquisition elapsed time between the first illumination mode used, Bessel CLDM, and the other illumination modes.

Figure 5.6 shows a section of the embryo's neural tube and somites, red and blue arrows, respectively, with the Bessel CLDM deconvolved mode of operation giving the image with the widest focal range covering most of the embryo. The layer of cells from the embryo surface inside of the zoomed white squares are best resolved by Bessel CLDM deconvolved. In Figure 5.6, the influence of the CLDM on Gaussian illumination conditioning the amount of signal collected in depth is clearly seen. The signal strength is higher inside the focus, located at the surface of the embryo, and confined to that region with fast degradation outside of the focus.

Figure 5.7 shows another two examples where the Bessel CLDM deconvolved mode of operation, overall, is more successful in resolving structures in deeper layers of an embryo in developmental stage HH10 than the Gaussian CLDM.

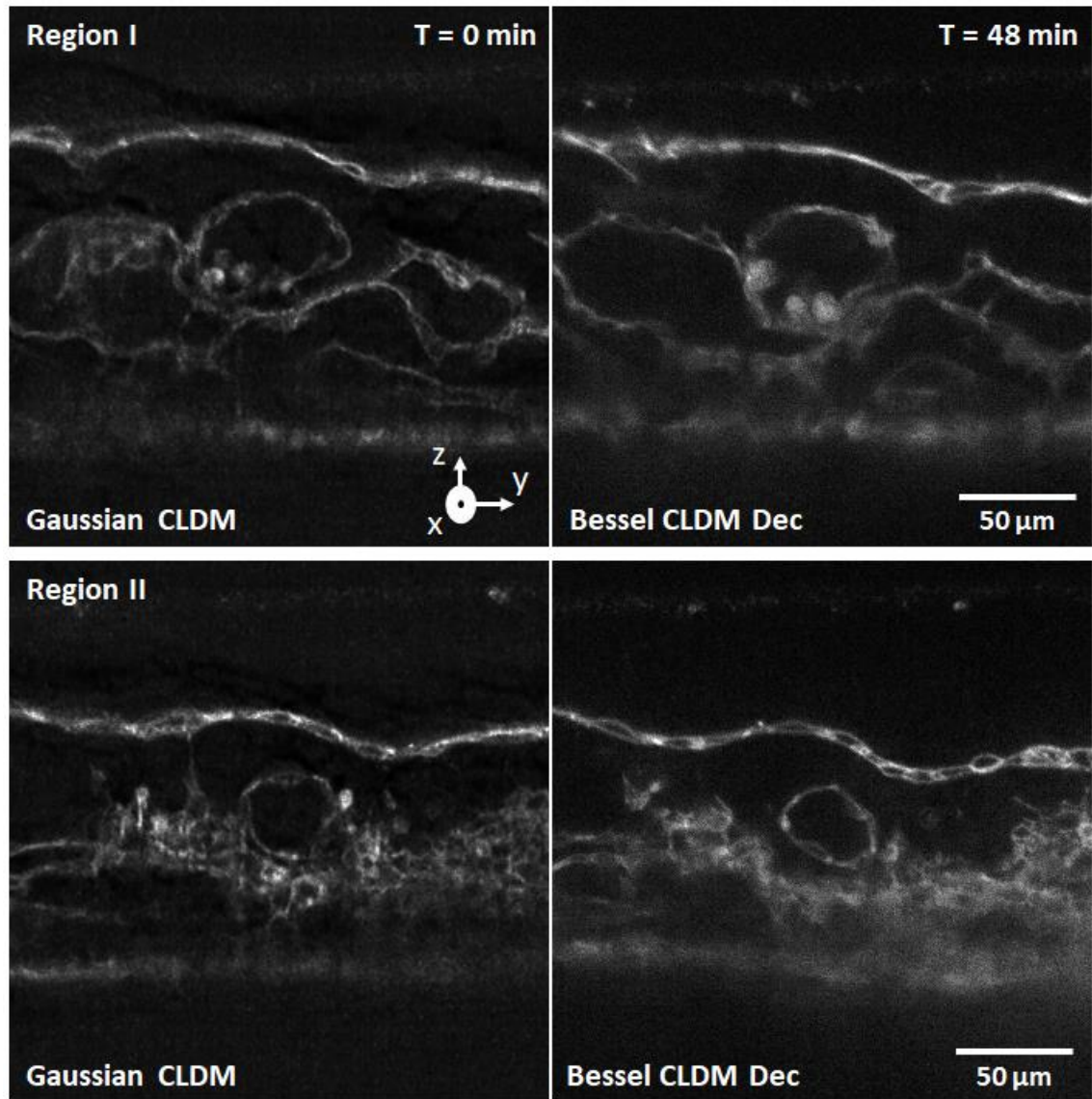


**Figure 5.7** Cross-section images from two distinct regions, Region I and Region II, inside of a HH10 developmental stage chick embryo. The embryo was imaged with Gaussian and Bessel illuminations, with CLDM for both illumination modes at 10x magnification. The Bessel images were deconvolved (Dec). T represents the acquisition elapsed time between the Bessel CLDM Dec and the Gaussian CLDM illumination modes.

However, it is not known whether this is a consequence of a wide focal range or due to an increased penetration depth. Regardless, the improvement brought about by Bessel illumination is not sufficient for cell tracking or segmentation, because the cell boundaries in out of focus regions are not significantly well defined.

## 5.2. 2-photon light-sheet DSLM

To implement the 2-photon illumination mode in the original 1-photon illumination mode system, illustrated in Figure 3.1, changes were made to the optical pathway (Figure 5.8). Details of the tuneable laser, lenses, scan lens, illumination tube lens and emission filter used are given in Table 5-3.

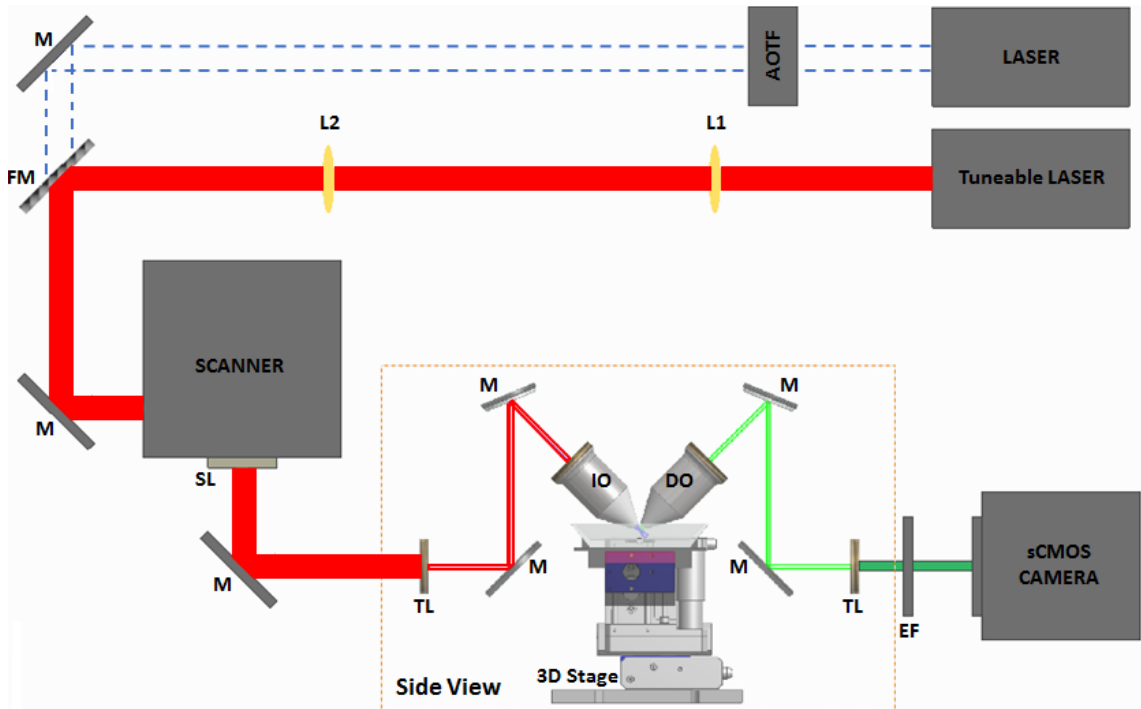


**Figure 5.8 DSLM set-up, incorporating two illumination pathways: 1-photon and 2-photon illumination modes.** The blue dashed lines and the red line represent 1-photon and the 2-photon excitation pathways, respectively. For 1-photon excitation: the laser is monochromatic 488 nm; the AOTF working as a shutter can control up to 8 wavelengths simultaneously; M – Mirror. For 2-photon excitation: the tuneable pulsed laser outputs the beam with wavelength ranging between 720-1010 nm; L1 and L2 – Lenses; M – Mirror; SL – Scan Lens. In the side view: TL – Tube Lens; M – Mirror; IO – Illumination Objective; C – Chamber holding the embryo; DO – Detection Objective; 3D stage to position and move the sample; EF – Emission Filter.

**Table 5-3 Details of new devices and parts used in DSLM 2-photon illumination pathway, illustrated in Figure 5.8.**  $\lambda$  – Wavelength, F – Focal Length.

Devices / Parts	Company	Part Number	Specification
Tuneable Laser	M Squared	Sprit XT	$\lambda$ : 720-1010 nm Output power ( $\lambda = 800$ nm): 1.5 W Pulse duration: 140 fs Repetition rate: 80 MHz
L1	Thorlabs	AC254-150-B-ML	F = 100 mm
L2	Thorlabs	AC254-300-B-ML	F = 250 mm
SL	Thorlabs	SL50-CLS2	$\lambda$ : 450-1100 nm Pupil entrance diameter: 4 mm Distance from pupil entrance to scan lens: 37.8 mm Working Distance: 26.4 mm
TL	Thorlabs	TTL200 - B	F = 200 mm
BF	Cairn Research	DC/ET750sp-2p8	$\lambda$ : 400-745nm

There are no changes required for the software commands and hardware connections from those used in chapter 3. In the optical set-up, a second beam path is inserted to direct 2-photon excitation towards the sample. A 2x telescope is placed after the tuneable laser, L1 and L2 in Figure 5.8, to control the beam focus extension to give a complete fill of the illumination objective back aperture. The scan lens used was provided by Thorlabs, model SL50-CLS2, it can be used for wavelengths ranging 450-1100 nm with a working distance of 26.4 mm. One flip mirror is used to switch between the 1-photon and 2-photon illumination modes.

For 2-photon excitation the laser emits a high power pulsed beam at 800 nm with 1.5W. Therefore, extra-care needs to be taken in illuminating biological samples for live imaging since this dose of energy, when absorbed by the sample, can compromise embryonic development. This leads to a trade-off between laser power and image exposure time, influencing the image acquisition frame rate. As a reference frame rate the values from Truong *et al.*<sup>38</sup> were considered, for instance a single frame

of 400 \* 900 pixels was exposed for 150 ms, for a wavelength of 940 nm with 100 mW, using a very low frame rate of 7 frames per second. Due to the low efficiency of 2-photon excitation there are two ways in which it is possible to increase the fluorescent signal collection. The first option was to increase the beam intensity, if possible, because the output power of the laser used in this project was dependent on the wavelength, with higher wavelengths resulting in a lower output power. The second option was to keep the laser power constant and to increase the camera exposure time, thus decreasing the acquisition frame rate. Because the laser power intensity was not controlled, the latter option was the only option available to increase the fluorescent signal of the live images acquired and presented in the following pages. At low frame rates the 1-photon illumination beam the laser output power used range was 0.1-1 mW, to avoid saturation of the sCMOS camera for an exposure time of XXX ms. With 2-photon illumination mode the laser output power range was 0.8 to 1.5 W, and no saturation of the sCMOS camera was observed, again for an exposure time of XXX ms.

To image the embryo with 2-photon and 1-photon illumination modes the frame rate was kept the same, although the laser output powers were different. The two laser output powers cannot be matched, since the power delivered with 2-photon illumination is not controlled and the power delivered with 1-photon illumination is limited to 20 mW, i.e. 2.5% of 0.8 W. Additionally, the intensity power after the illumination objective (Figure 5.8) was measured for 2-photon and 1-photon illumination modes and, approximately, only 17% and 30%, respectively, of the output laser power reaches the sample.

Images of the Gaussian beam profile generated by 1-photon and 2-photon excitation in a fluorescent medium (fluorescein) and a medium filled with fluorescent



plastic beads ( $0.2\ \mu\text{m}$ ), revealed the expected longer beam with 1-photon excitation (Figure 5.9) since the out of focus light is also recorded whilst with 2-photon excitation the signal comes, mostly, from the focus. This figure highlights the intrinsic characteristic of 2-photon excitation: low out of focus fluorescent signal before and after the focus, in contrast to 1-photon excitation. The 1-photon light-sheet in a medium with beads covers an area of beads approximately 5 times larger than the area illuminated by 2-photon light-sheet, since in Figure 5.9 both scanned beams are sent to the same medium filled with beads and with 1-photon illumination all the field of view shows the beads and with 2-photon illumination only the beads inside the beam focus are imaged (Figure 5.9, the red rectangle is approximately one fifth of image height).

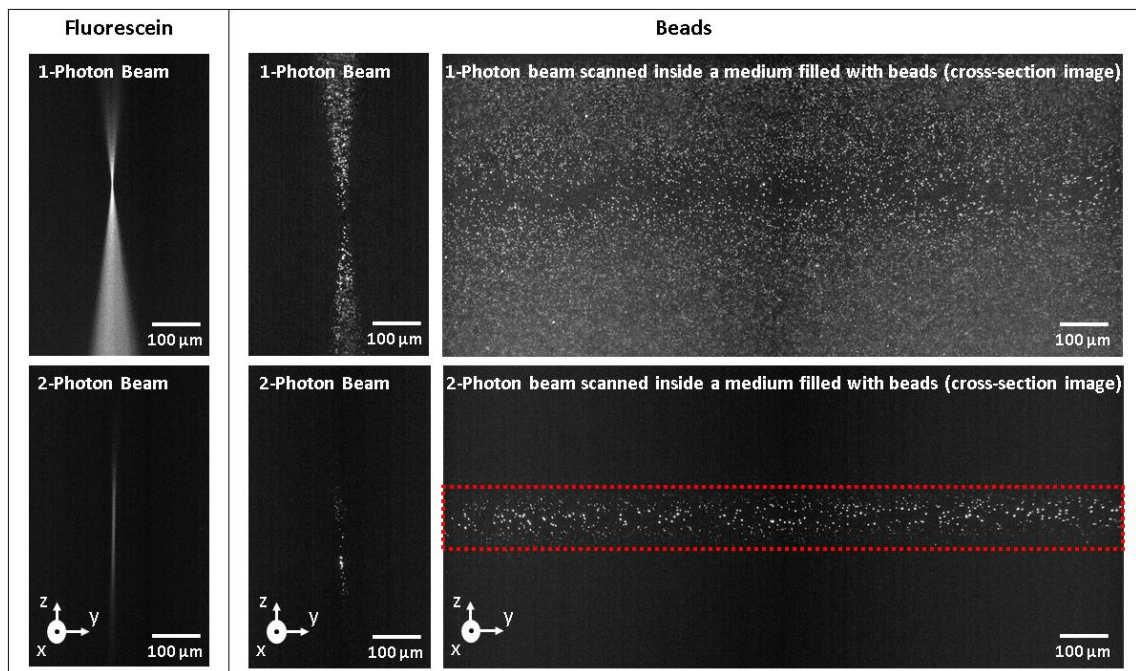


**Figure 5.9 1-photon and 2-photon excitation beam profiles in fluorescein solution and volume of beads (prepared according to section 2.4 of this document), and their respective light-sheets illuminating a medium filled with plastic beads ( $0.2\ \mu\text{m}$ ).** In the fluorescein images the beam is sent directly into the medium, the same happens in the beads left hand images. In the beads right-hand images' the image is acquired during a beam scan along the y axis direction, forming the light-sheet. The red dashed rectangle highlights the beads imaged with 2-photon light-sheet, is one fifth of the image height.



### 5.2.1. Results

Following the quest to optimise the DSLM microscope images, 2-photon excitation was implemented on the system as it was expected to achieve a better compromise between penetration depth and image contrast with this illumination mode when compared to images achieved by 1-photon excitation. Embryos at developmental stage HH1 were imaged using a 10x magnification detection objective (Figure 5.10 A, embryo surface and cross-section images). The image acquisition elapsed time between the 1-photon and 2-photon illumination modes is 3 minutes. The images were acquired at approximately 5.5 frames per second. For 2-photon illumination an excitation wavelength of 960 nm with the laser output average power of 0.8 W was used, while for 1-photon illumination an excitation wavelength of 488 nm with laser output power of 0.3 mW was used.

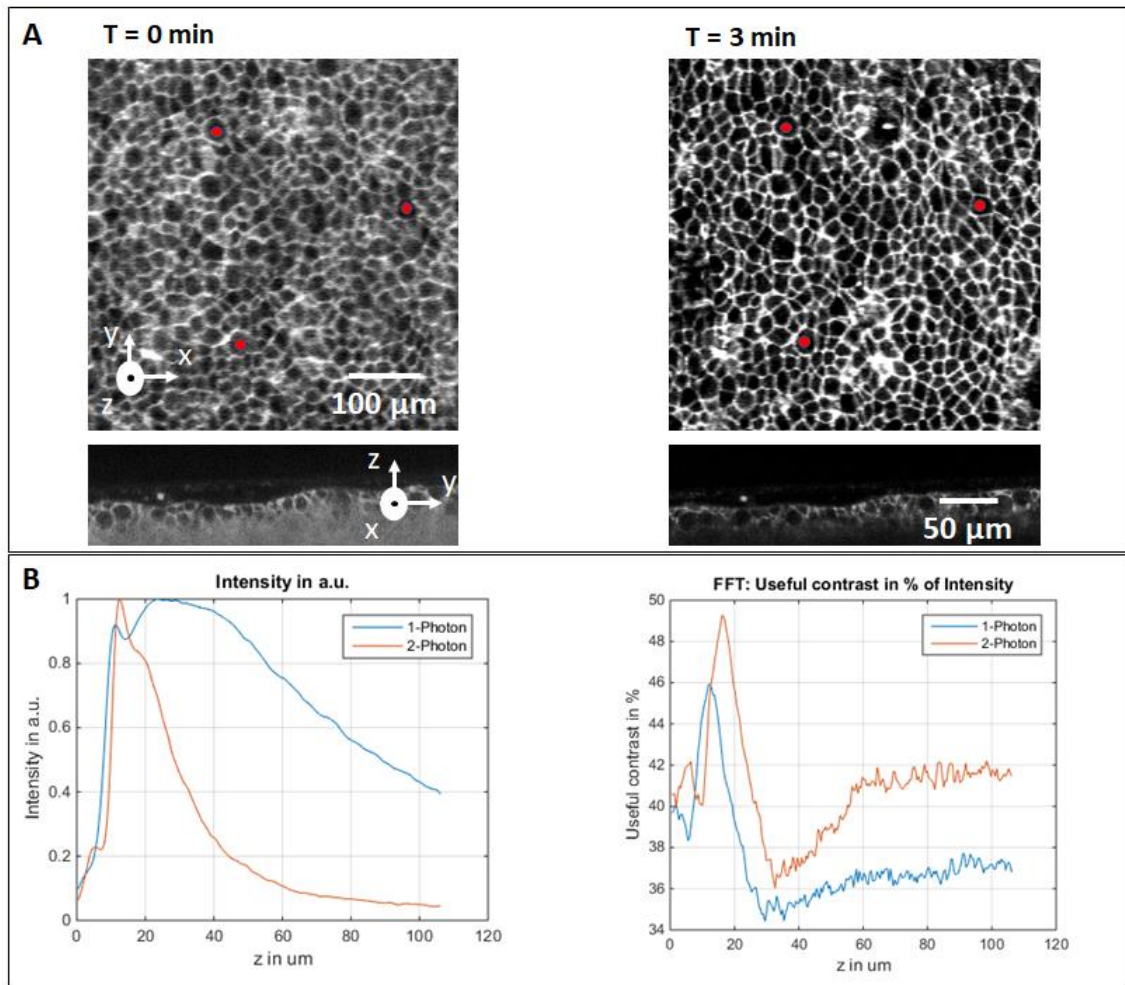


**Figure 5.10 Chick embryo at developmental stage HH1 imaged with 1-photon and 2-photon illumination modes, and their respective Intensity and Useful contrast plots. A)** Embryo surface and cross-section images, top and bottom, respectively. The images were acquired with 1-photon and 2-photon illumination modes, left and right-hand set of images, respectively. The red dots indicate the same cells in both images. T is the 3D stack acquisition elapsed time between 1-photon and 2-photon illumination modes. **B)** Intensity and Useful contrast graphs dependent on embryo depth, left and right-hand sides, respectively. Blue line – 1-photon illumination and red line – 2-photon illumination.

At HH1 the primitive streak is not yet formed. The images show a reduced background in the case of 2-photon excitation illumination image visual observation. This observation is supported by the Intensity graph in Figure 5.10 B showing a rapid intensity signal decay for 2-photon and a slow intensity decay for 1-photon. The rapid decay of intensity in depth for 2-photon excitation is due to the light absorbed and scattered after the embryo epiblast's first layers in combination with its localised excitation to the focal plane of the light-sheet. As a result, most of the 2-photon excitation fluorescent signal comes from the first two or three layers of cells from the

epiblast. While 1-photon illumination excites fluorophores before and after the focal plane of the light-sheet with out of focus light, in turn reducing the image contrast by increasing substantially the background signal. Note that at depth = 40  $\mu\text{m}$  1-photon intensity is almost 5x lower than the 2-photon intensity. The Useful contrast graph in Figure 5.10 B, shows that 2-photon illumination mode offers approximately 4% more contrast than 1-photon illumination.

Embryos at developmental stage HH4 with a visible primitive streak were imaged as well, Figure 5.11 A, at 5.5 frames per second. For 2-photon illumination a wavelength of 960 nm and 0.8 W laser output average power was used and for 1-photon illumination mode a 488 nm and 0.2 mW laser output power was used.

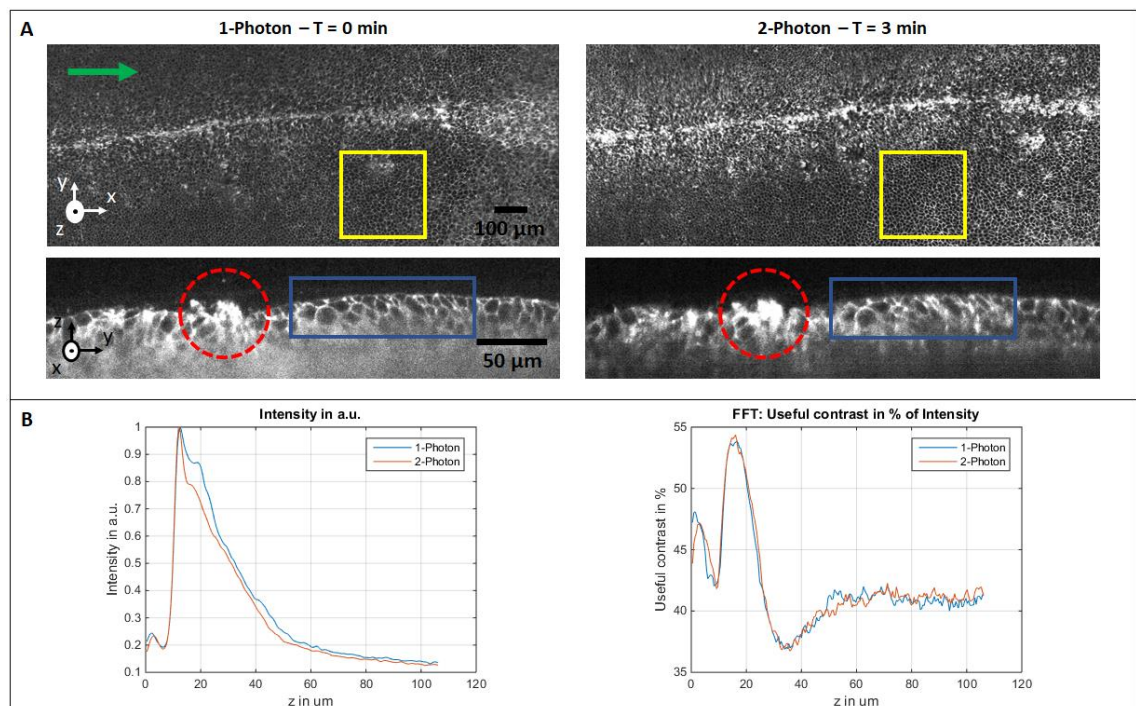


**Figure 5.11 Chick embryo at developmental stage HH4 imaged with 1-photon and 2-photon illumination modes, and their respective Intensity and Useful contrast plots. A)** Embryo surface and cross-section images, top and bottom, respectively. The images were acquired with 1-photon and 2-photon illumination modes, left and right-hand set of images, respectively. The blue rectangles are confining the same cells in both images. The red dashed circles show the primitive streak in the cross-section image. The green arrow points to the Posterior -> Anterior direction. The yellow squares show the region from which a 3D volume was cropped to perform Intensity and Useful contrast plots. T is the 3D stack acquisition elapsed time between 1-photon and 2-photon illumination modes. **B)** Intensity and Useful contrast graphs dependent on embryo depth, left and right-hand sides, respectively. The graphs were plotted over a volume cropped from the embryo images 3D stack (yellow square). Blue line – 1-photon illumination and red line – 2-photon illumination.

For an embryo in developmental stage HH4 imaged with the two illumination modes as shown in Figure 5.11 A, the visual observation of the images background looks very similar for both modes. This is verified in the Intensity graph in Figure 5.11 B where the 2-photon illumination intensity decay is not significantly faster than the intensity decay provided by 1-photon illumination. In the cross-section images the same cells are imaged (region inside the blue rectangles) with an elapsed time of 3 minutes and the image acquired with 1-photon illumination resolves better at the embryo surface cell boundaries than the image acquired with 2-photon illumination. Additionally, 2-photon offers only slightly better contrast than 1-photon, i.e. in less than 1% better contrast than 1-photon illumination mode (Figure 5.11 B Useful contrast graph).

Again, segmentation errors in surfaces imaged with 1-photon and 2-photon illumination modes were measured considering over and under-segmentation errors were analysed for the Gaussian and Bessel images as in chapter 5.1. This evaluation of the illumination mode that provides better data to segment is performed using Watershed principle. The surfaces analysed confine 475-600 cells. Segmentation error results are presented in Table 5-4 for embryos in developmental stages HH1 and HH4.

**Table 5-4 Embryos on developmental stages HH1 and HH4 surface segmentation errors counted manually.** Os – Over-segmentation, Us – Under-segmentation.

	HH1		HH4	
	Os	Us	Os	Us
Gaussian 1-photon	3.8 ± 2.1 %	10.2 ± 3.0 %	1.0 ± 1.0 %	9.4 ± 3.3 %
Gaussian 2-photon	1.7 ± 1.1 %	13.2 ± 5.1 %	0.2 ± 0.1 %	7.9 ± 2.3 %

The results from Table 5-4, clearly show that 2-photon excitation results in fewer segmentation errors for embryos in developmental stage HH4, for example it gives five-fold less over-segmentation errors when compared to 1-photon excitation.

For an embryo at HH1 developmental stage, 2-photon excitation offers two-fold less segmentation errors than 1-photon excitation. However, for both embryos at HH1 and HH4, there is no significant difference between the under-segmentation errors. Remembering that, for over-segmentation a single cell is segmented more than once and for under-segmentation some cells are not segmented. Then, the success of 2-photon illumination mode in showing less over-segmentation errors rises from the fact of having significant low levels of background. While the under-segmentation errors are more related to the fluorescent signal yield by each cell membrane, which varies from cell to cell. This is also visible in Table 4-1, for embryos in developmental stages HH1 and HH4 imaged with Bessel illumination CLDM upon deconvolution, at which proportionally the contrast improvement results in less over-segmentation errors when compared to the benefits attributed to under-segmentation errors.

To analyse the penetration depth provided by 2-photon illumination mode late stage developed embryos, with a beating heart, were imaged (Figure 5.12). However, there was no intention on imaging the beating heart or synchronising it with the image acquisition process<sup>41</sup>. From the cross-section images of the chick embryo heart, 2-photon illumination mode, 900 nm (1.51 W), better resolves the cells surrounding the heart, while 1-photon illumination mode, 488nm (0.5 mW), penetrates deeper into the embryo, giving a better perspective of the heart and its structures, although the image is very noisy. The heart is located a few tens of  $\mu\text{m}$  below the embryo surface. The images were acquired with an exposure of 7 frames per second.

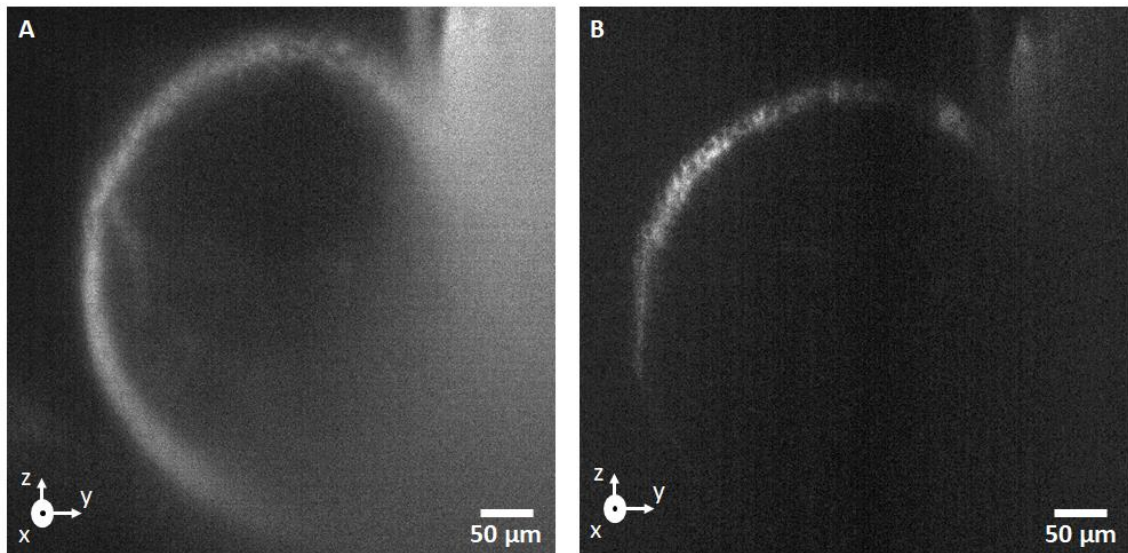


**Figure 5.12** Chick embryo at developmental stage HH12 heart cross-section images, acquired with 1-photon and 2-photon illumination modes, A) and B), respectively.

Figure 5.13 shows the chick embryo notochord and somites, yellow dashed ellipses and white circles, respectively. The notochord cross-section images agree with observations of the heart cross-section images, i.e. 2-photon illumination, 940 nm (1.1 W), better resolves structures in the first layers of the embryo, though at deeper levels it covers a smaller region of the embryo when compared to 1-photon excitation.

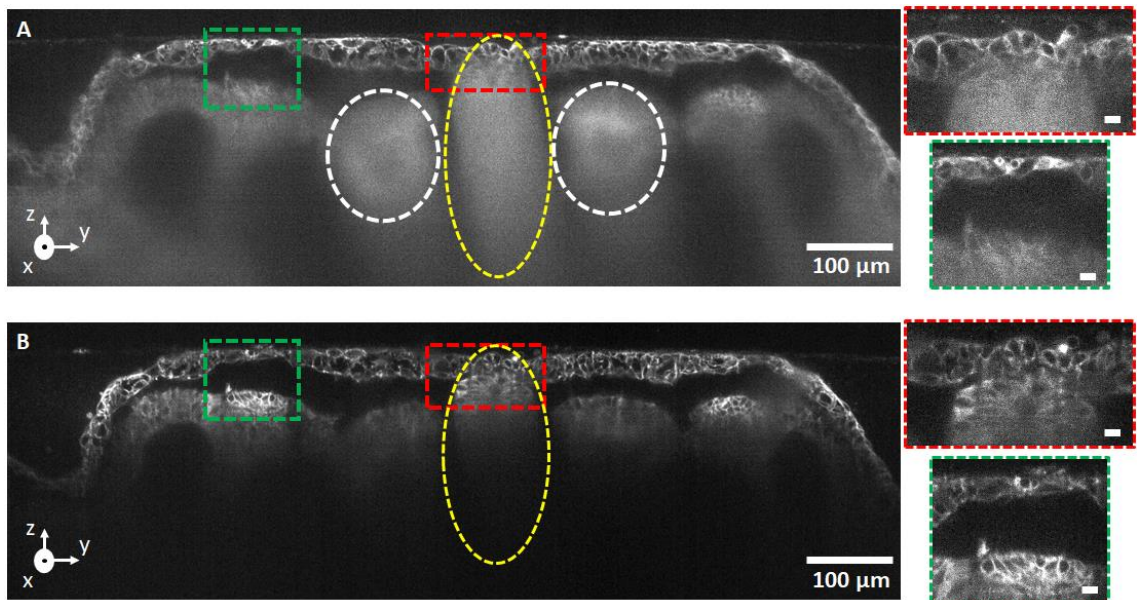


**Figure 5.13** Chick embryo at developmental stage HH12 notochord cross-section images, acquired with 1-photon and 2-photon illumination modes, A) and B) respectively. The yellow dashed ellipses surround the notochord. The white dashed circles surround the somites. The red and green dashed rectangles highlight the regions zoomed in on the right side of the cross-section images, A and B. The scale bar on the zoomed images is 10  $\mu\text{m}$ .



### 5.3. Discussion of results

It has been shown that chick embryo Bessel beam light-sheet live imaging gives poorer resolution when compared to Gaussian beam light-sheets<sup>51</sup>, mainly due to the Bessel side lobes contribution. As a result, it is not surprising to see the superior performance of the embryo surface segmentation in images acquired with Gaussian illumination modes. Deconvolution improves the Bessel CLDM images, bringing the image sharpness and contrast levels closer to the images obtained with Gaussian CLDM images (Figure 5.5). However, it is necessary to perform extra post-acquisition processing task (deconvolution), while obtaining Gaussian images is more straight forward.

What was not known was whether the Bessel beam generated extended focus and increased penetration depth would work in thick and complex structures such as chick embryos. Looking at the cross-section images from a few cell layers there is no evidence that Bessel CLDM deconvolved shows higher penetration depth than Gaussian CLDM (Figures 5.5). This reveals that Bessel illumination's non-diffracting property is limited by few layers of cells confined in a thick epiblast. Hence, it was decided to live image late stage developmental embryos, HH10, to evaluate the Gaussian CLDM and Bessel CLDM deconvolved performance for structures in the embryo's deeper layers (Figures 5.6 and 5.7). The gain provided by Bessel beam illumination was not considered substantial enough to use in post-acquisition analysis such as segmentation. Although, this research shows that Bessel beam illumination works better for imaging structures just below the first few cell layers of the embryo's epiblast (Figures 5.6 and 5.7). This is an important achievement regarding the

challenge of imaging a mammal's representative complex model system such as chick embryos.

All the images acquired are very dependent on the fluorescent signal provided by the chick embryo. The fluorescent signals vary considerably from embryo to embryo (Figure 3.1). Using 2-photon illumination mode the images are also dependent on the efficiency of the 2-photon excitation of the fluorophore. This makes the imaging process complex. To increase the 2-photon excitation efficiency the flux of photons must increase, and this can be done by increasing the laser power. The other way of increasing the fluorescent signal collection can be done by extending the image exposure time. This leads to a decreased frame rate and high-power leads to a decreased lifetime of the sample during *in vivo* imaging. This makes 2-photon excitation impracticable to use for fast live imaging, at least at 12 frames per second, covering a region of the chick embryo with 4 mm extension for tens of hours. In addition, embryo dual scan needs a frame rate of at least 25 frames per second. At low frame rates in large samples live imaging considerable events and processes happening in the embryo will not be captured.

Through a direct comparison between 1-photon and 2-photon illumination modes, looking at the 2D projections of the imaged embryos surface and their correspondent cross-section images, 2-photon illumination has better contrast, almost 4% for HH1 and less than 1% for HH4 developmental stages than 1-photon illumination in chick embryos (Figures 5.10 and 5.11). This suggests that for embryos developing at later stage HH4 the benefits of using 2-photon illumination decrease substantially. Overall, the segmentation results are better for 2-photon illumination than 1-photon illumination, with five-fold and approximately two-fold less over-segmentation errors for embryos at developmental stage HH4 and HH1, respectively.



The slight improvement provided by 2-photon illumination in penetration depth allows the visualisation of cells at deeper layers of the embryo (Figures 5.13 and 5.14), although the highlighted regions have low contrast and the cells will not be correctly segmented, as with the Bessel's illumination images, and the 2-photon illumination depth of focus is limited. The combination of 2-photon excitation and Bessel beam is, naturally, the next step to follow. Bessel gives an extended focus and an extended penetration depth, while 2-photon gives the higher contrast and an intrinsic capability of reaching the embryo deeper layers, due to the long wavelength. The final question for live imaging the challenging chick embryo: are better results achieved using 2-photon Bessel or CLDM Bessel? It is proposed that the best technique to implement would be 2-photon CLDM Bessel beam illumination mode. This results in a more complex system but the improvements may be significant.

## 6. Dual detection - illumination DSLM

The motivation for this project was to push LSFM to its limits for live imaging of chick embryos to support the study of the gastrulation process in early developmental stages up to primitive streak complete formation, looking at the tissue and in detail the cell-cell dynamics and their mechanical interactions. In order to accomplish this, the cells were followed by observing the embryo surface images and embryo cross-section images (see previous chapters). However, the embryo becomes undulated during development and this occurs everywhere within the embryo, possibly leading to situations at which the light-sheet becomes parallel to portions of the embryo surface making light-sheet sample sectioning less efficient. This can be prevented by sectioning the embryo from different views and the fusion of these views leads to a better 3D reconstruction of the imaged volume. This is possible because LSFM is a very fast technique.

Chapter 5 discussed how Bessel beams and 2-photon light-sheets are used to improve image contrast and penetration depth considering the unique properties of these illumination modes. This chapter discusses further re-designing and building of an improved and fully automated DSLM, the dual detection-illumination DSLM. Multi-view LSFM is well described and documented by the LSFM community<sup>4,5</sup> and can be performed by sample rotation<sup>20</sup>, and/or by increasing the number of illumination<sup>36</sup> and detection objectives<sup>29</sup>. In this research this was done through building a new optical system and using two objectives and working sequentially or simultaneously for illumination and detection<sup>91,92</sup>. The acquired images from two orthogonal views were merged together<sup>31</sup>, resulting in better image contrast and decreased image deterioration depth dependency<sup>91,92</sup>.

Imaging the sample with two orthogonal light-sheets results in the minimisation of the imaging “shadowing” effect. It has been mentioned that during development the chick embryo becomes more and more contorted, leading to situations in which the light-sheet is almost parallel to the embryo surface. The resulting image has shadowing on the embryo surface created by the almost parallel illumination. Another view or a second orthogonal illumination of the same region minimises the shadowing effect, as is shown in Figure 6.1.

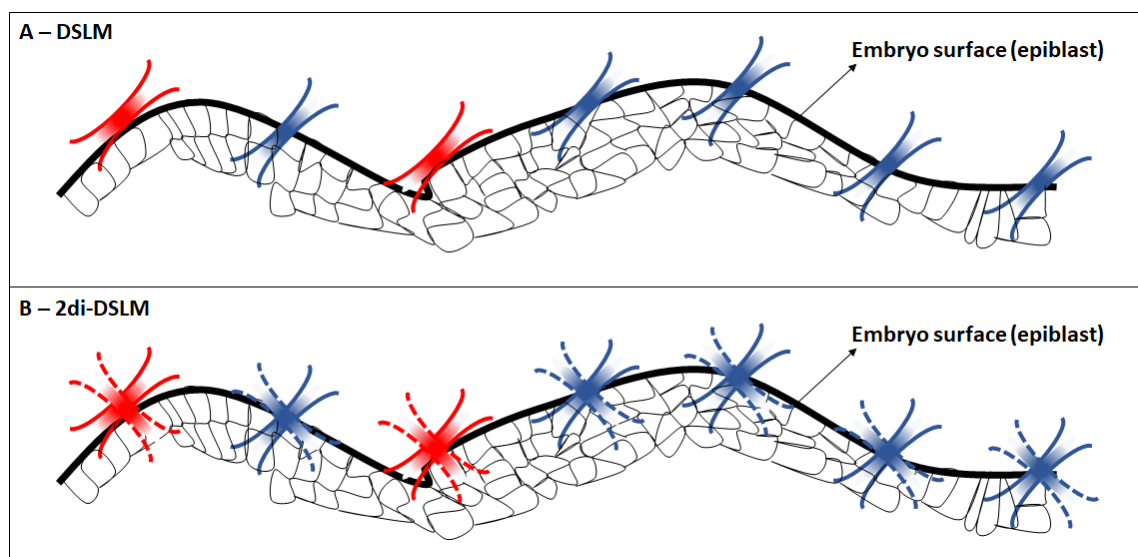


**Figure 6.1 Shadowing effect minimisation with 2di-DSLM. A)** In a DSLM, the red light-sheet cross-section indicates a situation at which the light-sheet is almost parallel to the embryo's surface, due to its curvature, leading to a shadowing effect on the image. **B)** Minimisation of the shadowing effect occurs in 2di-DSLM, where the dashed light-sheet cross sections bisect the embryo's surface at the regions where shadowing effect occurs on the DSLM, in red.

Since the chick embryos are illuminated at a  $45^\circ$  angle and the embryo is kept inside a chamber<sup>65</sup>, sample rotation would require complex engineering and re-design of the embryo chamber. Additionally, attention would need to be paid to the albumen medium within which the embryo is submerged, which needs to be steady to avoid imaging distortions due to liquid movements. Dual illumination-detection<sup>91</sup> requires a re-design of the microscope's optical set-up. Consequently, the image acquisition

procedure is affected, leading to changes in the microscope software to acquire images either sequentially or simultaneously.

## 6.1. Dual detection - illumination DSLM set-up and software

A new optical set-up was developed with the two objectives used in an alternating fashion for detection and illumination, leading to the dual detection-illumination DSLM (2di-DSLM) illustrated in Figure 6.2. In the optical set-up, instead of using two independent galvo mirrors or a galvo mirror combined with a 50:50 beam splitter to generate the light-sheets, a Knife edge prism was used. The advantage of the Knife edge prism is a single piece with two mirror surfaces placed orthogonally to each other.

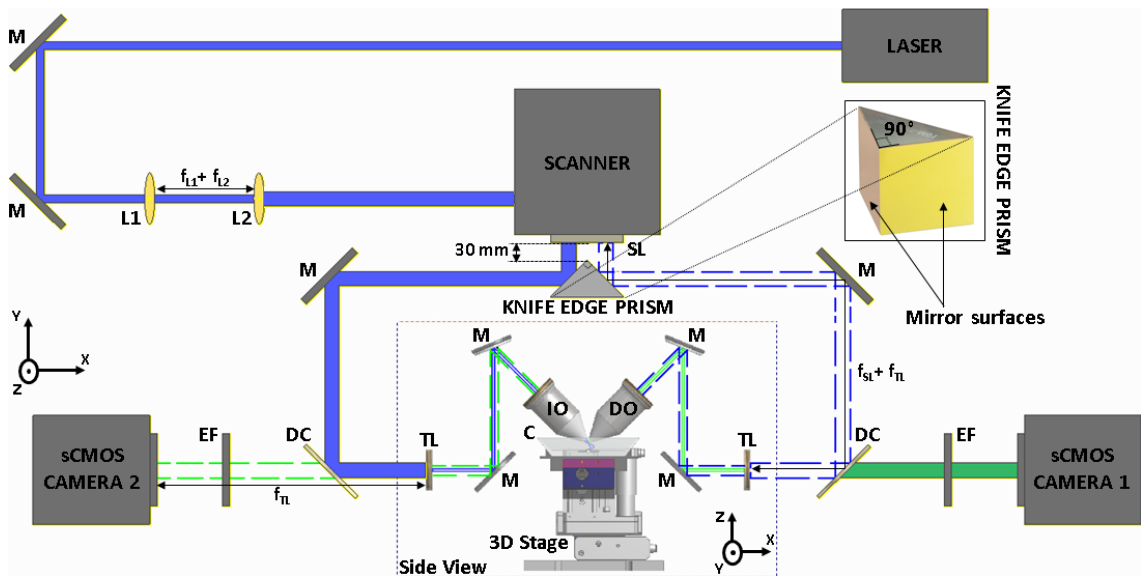


**Figure 6.2 2di-DSLM microscope optical set-up.** The blue solid line and the blue dashed line represent the sequential mode illumination. The green solid line and the green dashed line represent the sequential detection mode. The laser outputs a 488nm beam; M – Mirror; L1 and L2 are the Lenses on the beam expander telescope; Scanner, using two galvo-mirrors, scans the beam along two axes; SL – Scan Lens; DC – Dichroic mirror, reflecting wavelengths below 505nm and transmitting all the wavelengths above; EF – Emission Filter for GFP. On the side view: TL – Tube Lens; M – Mirror; IO – Illumination Objective; C – Chamber holding the embryo; DO – Detection Objective; 3D stage to position and move the sample. The Knife edge prism with two mirror surfaces is zoomed inside the black square, where the two mirror faces are pointed out. The distance between the SL and the TL is equal to the sum of their respective focal lengths,  $f_{SL} + f_{TL}$ ,  $f_{SL} = 160$  mm and  $f_{TL} = 200$  mm. The distance from the camera to the TL is equal to  $f_{TL} = 200$  mm, the same distance between each TL and the corresponding IO/DO.

Note that on the system presented there are no shutters for the laser beam, this means the laser is always ON. When images are not being acquired the scanner galvo-mirrors deviate the laser beam from the sample.

Details of the devices and optical parts used in the system illustrated in Figure 6.1 are given in Table 6-1.

**Table 6-1 Devices and parts used in the 2di-DSLM set-up illustrated in Figure 6.2.**

<b>Devices / Parts</b>	<b>Company</b>	<b>Part Number</b>	<b>Specification</b>
Laser	Melles Griot	643-RYB-A02	Air-cooled Krypton:Argon $\lambda = 488\text{nm}, 568\text{nm}$ and $647\text{nm}$
Mirrors	Thorlabs	PF10-03-P01	Protected Silver Mirror
L1	Thorlabs	AC254-050-A-ML	F = 50 mm
L2	Thorlabs	AC254-100-A-ML	F = 100 mm
Mirrors	Thorlabs	PF10-03-P01	Protected Silver Mirror
Knife Edge Prism	Thorlabs	MRAK25-P01	Protected Silver Mirror Surfaces
Scanner	SCANLAB	SCANcube 7	$\lambda: 450 - 2500 \text{ nm}$ XY Scan
Scan Lens	SCANLAB	100829	F = 160 mm Optimal $\lambda = 532 \text{ nm}$ $\lambda = 488 \text{ nm}: \text{Transmission} > 90\%$
Tube Lenses	Thorlabs	TTL200	F = 200 mm $\lambda: 350 - 700 \text{ nm}$
Objective 10x	Nikon	N10XW-PF	NA = 0.3 / WD = 3.5 mm
Dichroic Mirrors	Chroma	T505lpxr	Long pass filter, $\lambda = 505 \text{ nm}$
Emission Filter	Chroma	ET500lp	Long pass filter, $\lambda = 500 \text{ nm}$
sCMOS Camera	Hamamatsu	ORCA-Flash4.0 V3 – C13440-20CU	Pixel: $6.5 \mu\text{m} * 6.5 \mu\text{m}$ Chip: $2048 * 2048$ pixels Full frame acquisition rate: 100 frames/second
3D Stage	Physik Instrumente	V-524.1AA/1AB and V-528.1AB	Max Velocity = 250 mm/s Resolution = 20 nm 3 Axes mounted -> XYZ X: V-524.1AA Y: V-524.1AB Z: V-528.1AB

To build a more compact and robust system requiring minimal adjustments with accurate alignment, two arms were designed. The arms hold both illumination and crucial detection optics: tube lens, mirrors and objective (Figure 6.3). The mirrors,

tube lenses and objectives are placed at the exact locations in the arms to deliver an aligned laser beam and light-sheet at a 45° angle to the sample.

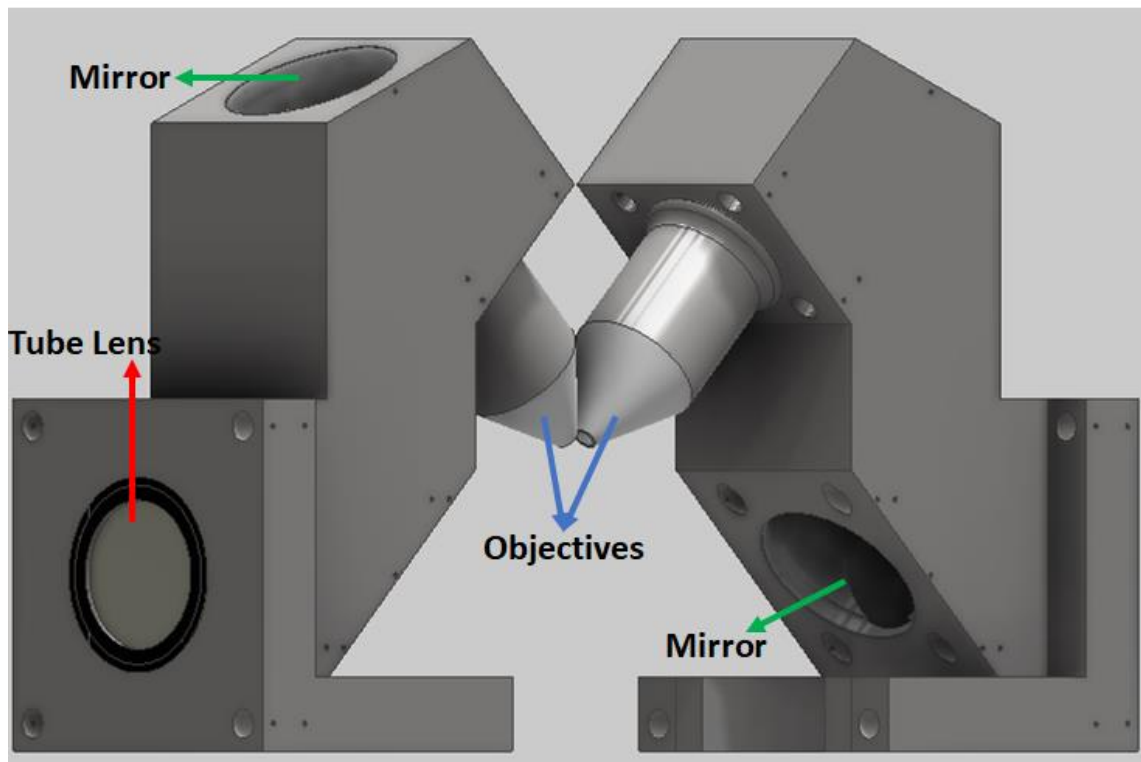


**Figure 6.3** Illustration of the 2di-DSLM arms holding: tube lens, mirrors and objectives.

The microscope arms are independent from each other as illustrated in Figure 6.3. This means that during the system alignment, the arms need to be brought together to the exact position at which the two light-sheets intersect at a 90° angle. The objectives' focus need to be positioned exactly at the intersection of both light-sheets, for both arms. Therefore, the focus plane of the two arms is coincident assuring that both are imaging the same object.

The software to control the microscope was written in C++. The acquisition of images is made through software commands and hardware TTL connections. The scanner controls camera1 through a TTL connection. The scanner TTL signals are Mark and Jump, which refer to Low and High voltages for TTL signalling, respectively. For both signals the scanner moves the galvo-mirrors to specific positions, indicated by the

user. With the Mark signal the laser beam is scanned along the knife edge prism mirrored surface to produce the light-sheet for Camera1 and with the Jump signal the laser beam is scanned along the second mirrored surface of the knife edge prism to produce the light-sheet for Camera2. For reference, when the scanner controls the laser through hardware connections, which is not the case of the presented system, Mark is usually used to turn ON the laser beam and Jump to turn it OFF.

Camera1 controls Camera2 through another TTL connection. After acquiring a set of frames defined by the user, a 3D stack with all the frames from each camera is saved on the hard disk of the control PC. The process is similar to the one used by the DSLM system, presented in the second chapter, for image acquisition. During an experiment, the 3D stage can be moved in a step by step motion or in an automatic mode called the profile mode. The stepping mode is controlled and commanded by the software and it is slower than the profile mode. In the latter mode, due to a special feature of the 3D stage, the stage can hold in a position after performing a movement of defined step. For example, the stage can perform 2000 steps of 1  $\mu\text{m}$ , each step being executed in 5 milliseconds with the position being held for 10 milliseconds after each step. The steps are automatically performed every 15 milliseconds. The step size, the number of steps, the time to perform each step and the time to hold a position after each step are determined by the user. Once the stage is in the holding position the frames can be acquired. Both 3D stage operation modes are initialized by software commands, exactly before the scanner starts forming the light-sheet. Ideally, the Scanner would trigger the stage to start the motion.

The 3D stage and scanner are controlled by software commands, while Camera1 and Camera2 are triggered by TTL hardware commands (Figure 6.4).

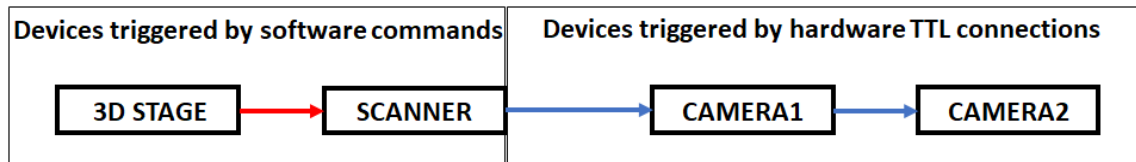


**Figure 6.4** 2di-DSLM devices triggered by software, 3D Stage and Scanner, and devices triggered by hardware TTL connections, Camera1 and Camera2. The scanner is always triggered after the 3D stage, as indicated by the red arrow. The scanner triggers camera1 through a TTL signal, and camera1 triggers camera2 through another TTL signal, indicated by the blue arrows.

The microscope operates in two acquisition modes: simultaneous or sequential, as illustrated in Figure 6.5.

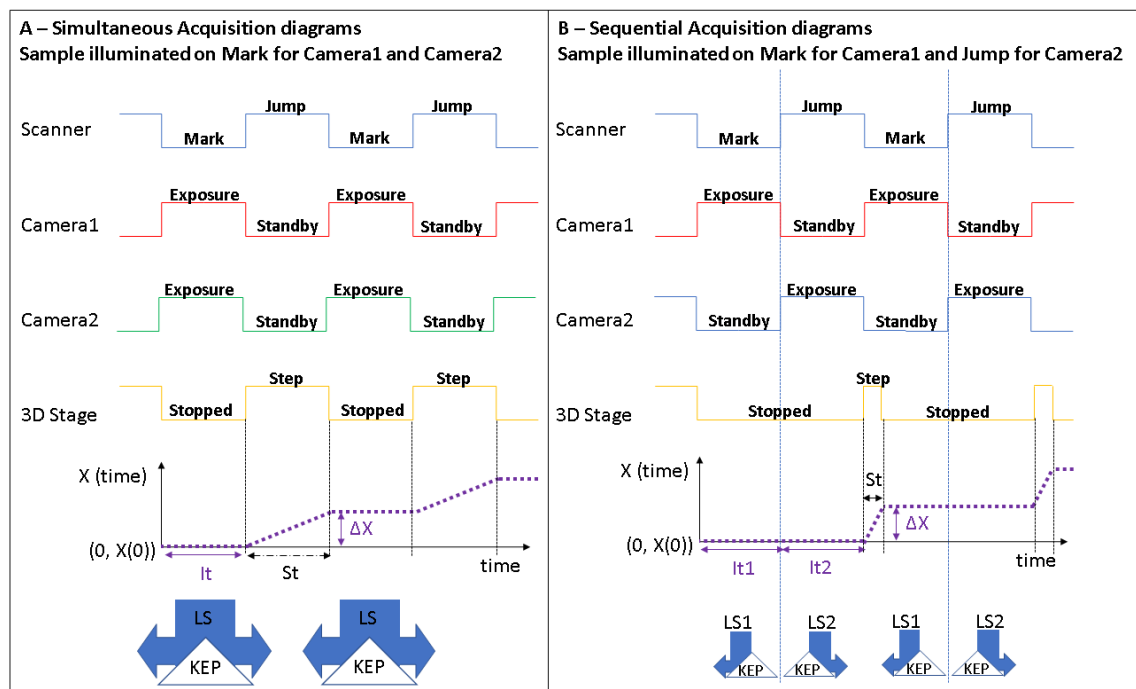


**Figure 6.5** Microscope Scanner, Cameras and Stage operation during image acquisition modes: simultaneous and sequential, illustrations A and B respectively. KEP - Knife Edge Prism. **A)** In simultaneous mode, Camera1 and Camera2 exposure occurs at same time. The plot at the bottom illustrates the sample illumination time,  $I_t$ , the stepping time,  $St$ , the stage step size,  $\Delta X$ , and the sample position depending on time,  $X$  (time). The Light-Sheet (LS) is sent to cover both mirror faces of the KEP at once. **B)** In sequential mode, Camera1 and Camera2 exposure occurs in sequence. The plot at the bottom illustrates the sample illumination time for Camera1 and Camera2,  $I_{t1}$  and  $I_{t2}$ , the stepping time,  $St$ , the stage step size,  $\Delta X$ , and the sample position depending on time,  $X$  (time). The first Light-Sheet (LS1) is sent to the first mirror face of the KEP and once Camera1 has finished exposing the second Light-Sheet (LS2) is sent to the second mirror face of the KEP and Camera2 starts exposing.

In simultaneous mode ideally both cameras would collect images at the same time, requiring the two light-sheets to be delivered through the sample at the same time as well. In the 2di-DSLM, since the scanner triggers camera1 and camera1 triggers



camera2, this means that both cameras are exposing all the time in the simultaneous mode when the scanner is forming the light-sheet across the knife edge prism reflective faces. In the sequential mode, the cameras are exposing sequentially in time. Camera1 is the first to take an image and once its exposure finishes the exposure of camera2 is initiated with the cameras never exposing at the same time. The scanner Mark and Jump commands are designed to control laser beam intensity during the scanning process, which is not the case in the current 2di-DSLM microscope. These Mark and Jump TTL signals are used to trigger the cameras. Camera1 is triggered by the Mark command provided by the scanner. Camera2 receives its trigger from camera1 as outlined in Figure 6.4.

### 6.1.1. Results

Initially the intention was to use a 50:50 beam splitter, but the 2di-DSLM optical set-up did not include light shutters limiting the beam splitter usage to simultaneous acquisition. Therefore, the beam splitter could not be used for sequential imaging. As a solution a knife edge prism was used to operate the microscope in sequential and simultaneous acquisition modes (Figure 6.6) without requiring the incorporation of shutters into the system (Figure 6.2).

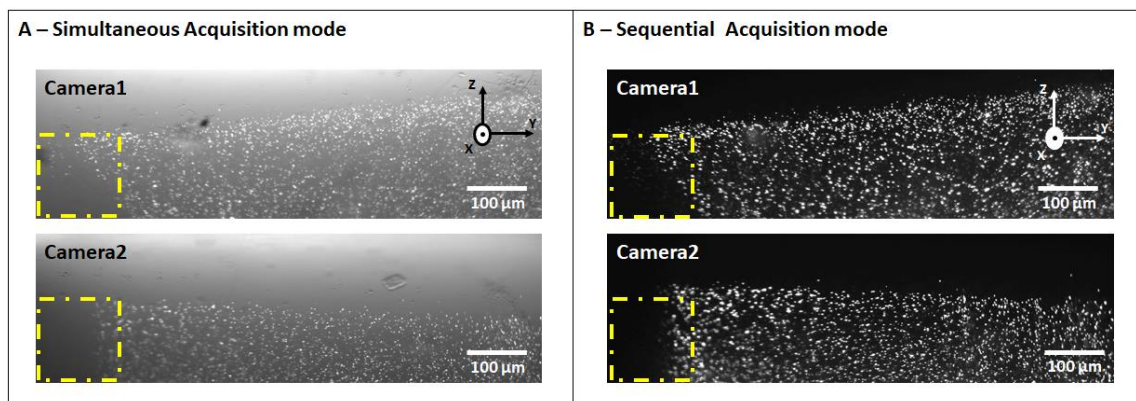


**Figure 6.6 Plastic beads (prepared according to section 2.4 of this document), 0.5 μm, cross-section images acquired with 2di-DSLM in simultaneous and sequential modes, A) and B) images, respectively. Due to misalignment issues the cross-section field of view was partially filled and the yellow dashed square shows the gap on the images.**

The empty space on the left side of the cross-section images in Figure 6.6, confined by the yellow dashed square, occurs due to microscope misalignment issues on the detection and illumination objectives field of views intersection at the same plane. The light-sheets bisecting the sample are not coincident since Camera1 cross-section images are not coincident with Camera2 cross-section images. The microscope arms, illustrated in Figure 6.3, had manufacturing defects which caused displacement of the optical parts, including tube lenses, mirrors and objectives, from the exact location at which the parts would maintain the correct beam alignment inside the arms. The knife edge prism is a prism with two reflective surfaces, with the exact same dimensions, placed orthogonally in relation to each other forming an edge. Due to the knife edge prism geometry, it is not possible to use exact simultaneous illumination onto the sample or two light-sheets being delivered in at the exact same time into the sample. The solution was to expose both cameras at the same time, while the light-sheets in both arms are formed by the scanner travelling from one reflective surface of the knife edge towards the other reflective surface.

Referring to the images shown in Figure 6.6, the background signal present in the images acquired with the simultaneous mode is substantially minimised by changing the acquisition mode regime to sequential. A ruler was imaged by the two objectives ensuring that both were focused into the same plane. Therefore, the 2di-DSLM was used to image the chick embryo in an area where it could be ascertained that the same region of the chick embryo was imaged by the two objectives, Figure 6.7.

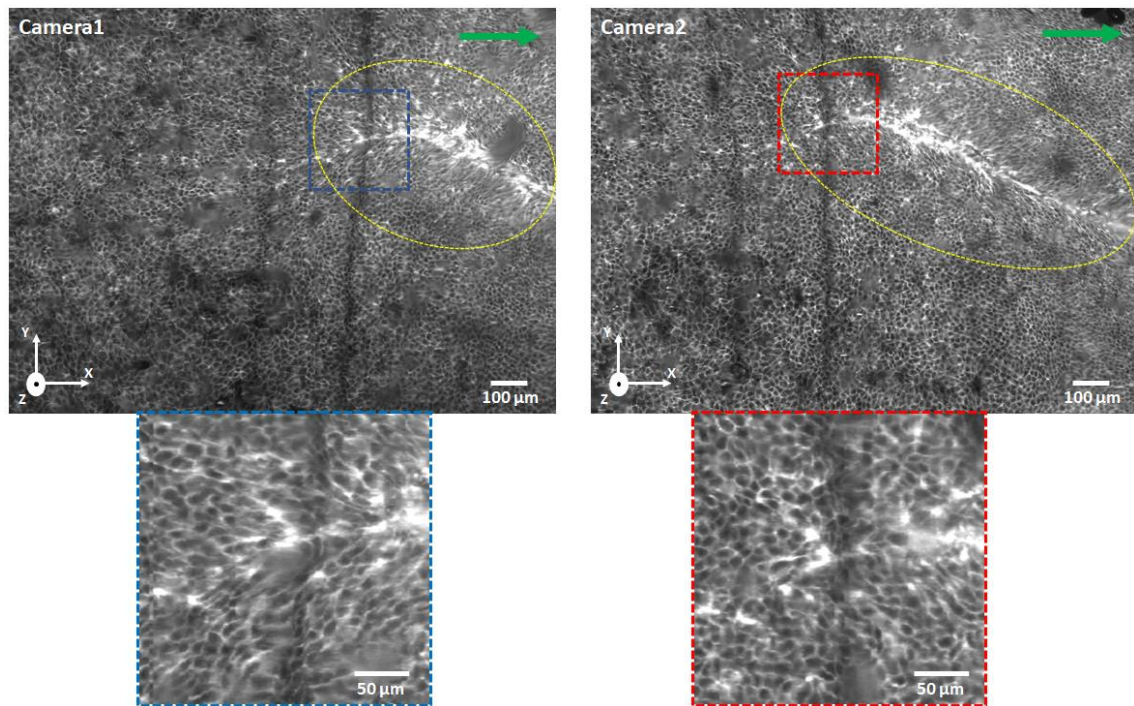


**Figure 6.7 2di-DSLM chick embryo at developmental stage HH3 surface images acquired in sequential acquisition mode.** The blue and red dashed rectangles are the correspondent zoomed regions close to the anterior tip of the primitive streak, below each embryo surface image. The dashed yellow circle surrounds the primitive streak and the green arrow points towards the Anterior → Posterior direction.

In Figure 6.7 the chick embryo surface images from Camera1 and Camera2 show the same region of the embryo, considering that it is hard to identify the same cells imaged by both cameras. The images confirm that the two arms, and consequent light-sheets, were not properly aligned. Other evidence of the system misalignment is visible on the chick embryo cross-section images, in Figure 6.8. The cross-section images from camera1 and camera2 have very few common or similar cells and details. The primary mechanisms for co-locating images relies on the position of the primitive streak and the shape of the fluorescent membrane vesicles present on the top of the streak.

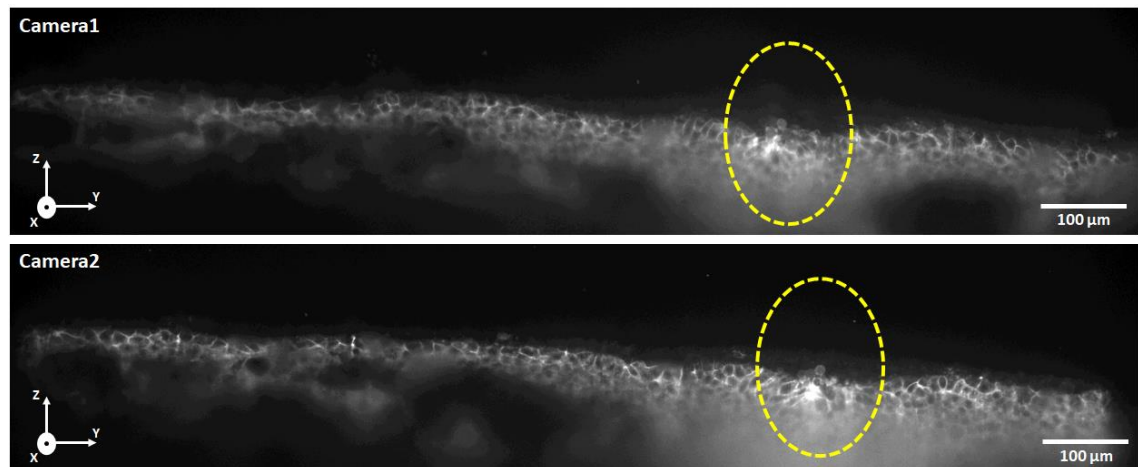


**Figure 6.8** 2di-DSLM chick embryo at developmental stage HH3 cross-section images, acquired in sequential acquisition mode. The dashed yellow ellipse surrounds the primitive streak furrow.

## 6.2. Discussion of results

Due to a misalignment issue, it is difficult to fully assess or discuss the results offered by 2di-DSLM in direct comparison to the ones provided by DSLM. As shown in the images in Figures 6.7 and 6.8, 2di-DSLM has less background signal with the sequential acquisition mode than with simultaneous acquisition mode. The knife edge prism is a better solution than the 50:50 beam splitter using the sequential acquisition mode, when light shutters are not being used. Whilst acquiring images in simultaneous mode both cameras are exposing for the exact same time, but the light-sheet travels from the first reflective surface of the knife edge prism towards the second reflective surface. Thus, a 50:50 beam splitter is required for true simultaneous mode operation, where both light-sheets are delivered into the sample at same time as the images are collected. However, simultaneous imaging would result in increased background signal, even if appropriate dichroic mirrors and a dedicated GFP emission filters are used.

The 2di-DSLM concept and design was challenging, due to the complexity of the optical system and the software and hardware connections required to control the

microscope. After careful examining of the two arms used in the microscope it was found that the holes holding the mirrors, tube lenses and objectives were positioned incorrectly. The imperfections in the positioning of these critical components was enough to compromise the correct dual view image acquisition. However, this chapter shows efforts to design a robust and compact 2di-DSLM optical set-up and exhibits its preliminary imaging results (Figures 6.6, 6.7 and 6.8). For the near future, the best way to improve the 2di-DSLM system compactness and alignment would rely on accurate manufacturing of the two 2di-DSLM arms (Figure 6.3) in the same block with the exact positioning of all the optical components.

## 7. Conclusions

There is no novelty in using LSFM to live image chick embryo development up to primitive streak formation<sup>3</sup>. This project aimed to improve a DSLM microscope to acquire chick embryo live images with increased: contrast, sharpness, penetration depth and depth of focus. The microscope improvement would allow further study of the chick embryo cell-cell chemical and mechanical signalling during the gastrulation process. The chick embryo is quite a challenging model system due to its low transparency, millimetric size, thickness and structural complexity, when compared to the most usual embryos live imaged with LSFM, e.g. *C. Elegans*, *Drosophila* or Zebrafish.

The novelty of this project lies in the approach followed to reach the project goals, leading to live imaging of the chick embryo through the incorporation of known techniques into the basic DSLM microscope set-up, i.e. a known detection technique (CLDM) and two known illumination modes (Bessel beam and 2-photon), and through building a dual illumination-detection DSLM microscope.

The changes and optimisations made to the DSLM microscope optical set-up, software and hardware communications resulted in images with increased: contrast, sharpness, penetration depth and depth of focus. In addition, the optimisations and changes made to the microscope increased acquisition speed and dual colour capability.

High speed DSLM enables whole embryo *in vivo* imaging, by scanning the embryo multiple times until complete coverage is obtained. This allows a better correlation between cellular motion and tissue flow looking at different regions of the

embryo. For chick embryos in the early stages of development this allows coverage of 90-95% of the embryo surface, scanning the embryo twice at 25 frames per second. This maintains 3 minutes of elapsed time between 3D stacks. These 3 minutes allow gathering of all the cellular and tissue information occurring during the chick embryo live imaging, without a significant loss of information.

Dual scan doubles the experimental data size, to approximately 1 TB per experiment. Through increasing the frame rate at which the images are acquired the embryo can be scanned three or four times. However, increasing the number of scans generates more data, thus increasing analysis time. In this project two scans gave a good compromise between data generated and information collected from beginning of chick embryo gastrulation to primitive streak full extension.

Dual colour DSLM allows colocalisation of 2 proteins. Unfortunately, during this project chick embryos with two fluorophores were not imaged. The simultaneous observation of the role of two proteins on the embryo open the possibility to learn and follow in detail the action of complementary proteins or to establish the correlation between specific proteins.

As predicted, confocal line detection enhances image contrast. The results are easily visible in the images collected. The implementation of this allowed tracking and monitoring of epiblast cells during ingression events. This enabled the investigation of vesicle origin, which in the first instance was found out to be a consequence of cell ingression. The current issue with CLDM relies on its low maximum frame rate speed of 15 frames per second, which does not enable double scanning of the embryo, as this requires 25 frames per second, covering a bigger region of the embryo.

Bessel beam light-sheet illumination appears to be a very “costly” technique. The cost comes from its optical implementation and the process at which the images are submitted until relevant information can be extracted from them. Optimisation of the benefits of Bessel beams linked to the minimal image post-acquisition processing was attempted. This was possible through the combination of Bessel beams with CLDM, suppressing considerably the Bessel side lobes contribution to the images. Nevertheless, the images were not comparable to those obtained using Gaussian illumination beams. After deconvolving the images, the results were slightly improved, but still not to the level of Gaussian illumination beams. Improvements were seen at the penetration depth provided by Bessel beams in comparison to Gaussian beams. However, considering the necessity of cellular segmentation as a starting point for image analysis, the penetration depth improvement was not significant enough to justify the usage of Bessel illumination over Gaussian illumination. However, with depth of focus and penetration depth being prime considerations it was decided that it was worth spending time optimising the Bessel illumination set-up, combining it to CLDM and improving the image post-acquisition processing. Although, if the sample is relatively transparent and structurally simple, not thick and complex as is a chick embryo sample, the results may be significant.

In terms of penetration depth Gaussian 2-photon illumination mode does not bring a significant improvement when compared to Gaussian 1-photon illumination. However, the improvement of contrast and signal detection is effective. Although, the implementation of 2-photon illumination with all the optical changes and improvement is tricky and complex. As result, a 10 hours live imaging was not



performed since after 2/3 hours of imaging the embryo structure was damaged due to laser high intensity power. Gaussian 1-photon would be the mode of choice for imaging thick and big samples such as chick embryo as this illumination mode provides better compromise concerning image quality, sample preservation and degradation.

According to the literature, dual illumination-detection DSLM or 2di-DSLM is a promising technique. With the data obtained and knowing it was acquired in a misaligned system, its benefit on chick embryo live imaging cannot be evaluated. The problem now is the system alignment, which can be solved through designing new arms and ensuring that all the optical parts and devices are positioned in their exact and correct positions. It is suggested that both arms are on the same physical platform, and formed from a single piece. This should ensure the best symmetry for both illumination-detection pathways which was practically unachievable with two independent arms, with mirrors slightly out of positions.

Finally, it is important to note that in LSFM there is space for the implementation of additional techniques, improving the system due to the independence of the illumination and detection axes, these techniques can be implemented individually or combined. This makes LSFM one of the most versatile microscopic techniques of the present time.

## References

1. Chuai, M., Hughes, D. & Weijer, C. J. Collective epithelial and mesenchymal cell migration during gastrulation. *Curr. Genomics* **13**, 267–77 (2012).
2. Chuai, M. *et al.* Cell movement during chick primitive streak formation. *Dev. Biol.* **296**, 137–149 (2006).
3. Rozbicki, E. *et al.* Myosin-II-mediated cell shape changes and cell intercalation contribute to primitive streak formation. *Nat. Cell Biol.* **17**, 397–408 (2015).
4. Stelzer, E. H. K. Light sheet fluorescence microscopy for quantitative biology. *Nat. Methods* **12**, 23–26 (2015).
5. Power, R. M. & Huisken, J. A guide to light-sheet fluorescence microscopy for multiscale imaging. *Nat. Methods* **14**, 360–373 (2017).
6. Tomer, R., Khairy, K., Amat, F. & Keller, P. J. Quantitative high-speed imaging of entire developing embryos with simultaneous multiview light-sheet microscopy. *Nat. Methods* **9**, 755–63 (2012).
7. Stern, C. D. & Downs, K. M. The hypoblast (visceral endoderm): an evo-devo perspective. *Development* **139**, 1059–69 (2012).
8. Wolpert, L., Tickle, C. & Arias, A. M. *Principles of Development, Fifth Edition.* (Oxford University Press, 2015).
9. Weinberger, C., Penner, P. L. & Brick, I. Polygression, an important morphogenetic movement in chick gastrulation. *Integr. Comp. Biol.* **24**, 545–554 (1984).
10. Weinberger, C. & Brick, I. Primary hypoblast development in the chick. *Wilhelm Roux's Arch. Dev. Biol.* **191**, 119–126 (1982).
11. Bertocchini, F. & Stern, C. D. The hypoblast of the chick embryo positions the

- primitive streak by antagonizing nodal signaling. *Dev. Cell* **3**, 735–744 (2002).
12. Mitrani, E., Shimoni, Y. & Eyal-Giladi, H. Nature of the hypoblastic influence on the chick embryo epiblast. *J. Embryol. Exp. Morphol.* **75**, 21–30 (1983).
  13. Hamburger, H. L. H. A series of normal stages in the development of the chick embryo. *Dev. Dyn.* **88**, 49–92 (1951).
  14. Voiculescu, O., Bertocchini, F., Wolpert, L., Keller, R. E. & Stern, C. D. The amniote primitive streak is defined by epithelial cell intercalation before gastrulation. *Nature* **449**, 1049–52 (2007).
  15. Voiculescu, O., Bodenstern, L., Lau, I. J. & Stern, C. D. Local cell interactions and self-amplifying individual cell ingression drive amniote gastrulation. *Elife* **3**, e01817 (2014).
  16. Wolpert, L. *et al. Principles of Development.* (1997).
  17. Wagstaff, L. J., Bellett, G., Mogensen, M. M. & Münsterberg, A. Multicellular rosette formation during cell ingression in the avian primitive streak. *Dev. Dyn.* **237**, 91–96 (2008).
  18. Tomer, R., Khairy, K., Amat, F. & Keller, P. J. Quantitative high-speed imaging of entire developing embryos with simultaneous multiview light-sheet microscopy. *Nat. Methods* **9**, 755–63 (2012).
  19. Keller, P. J. *et al.* Fast, high-contrast imaging of animal development with scanned light sheet-based structured-illumination microscopy. *Nat. Methods* **7**, 637–642 (2010).
  20. Haseloff, J., Stelzer, E. H. K., Maizel, A., Universita, G. & Street, D. High-resolution live imaging of plant growth in near physiological bright conditions using light sheet fluorescence microscopy. 377–385 (2011). doi:10.1111/j.1365-313X.2011.04692.x

21. Weber, M. & Huisken, J. Light sheet microscopy for real-time developmental biology. *Curr. Opin. Genet. Dev.* **21**, 566–572 (2011).
22. Saghafi, S., Becker, K., Hahn, C. & Dodt, H. U. 3D-ultramicroscopy utilizing aspheric optics. *J. Biophotonics* **7**, 117–125 (2014).
23. Fu, Q., Martin, B. L., Matus, D. Q. & Gao, L. Imaging multicellular specimens with real-time optimized tiling light-sheet selective plane illumination microscopy. *Nat. Commun.* **7**, 11088 (2016).
24. Royer, L. A. *et al.* Adaptive light-sheet microscopy for long-term, high-resolution imaging in living organisms. *Nat. Biotechnol.* 1–125 (2016). doi:10.1038/nbt.3708
25. Ahrens, M. B., Orger, M. B., Robson, D. N., Li, J. M. & Keller, P. J. Whole-brain functional imaging at cellular resolution using light-sheet microscopy. *Nat Methods* **10**, 413–420 (2013).
26. Pantazis, P. & Supatto, W. Advances in whole-embryo imaging: a quantitative transition is underway. *Nat. Rev. Mol. Cell Biol.* **15**, 327–39 (2014).
27. Ritter, J. G., Veith, R., Veenendaal, A., Siebrasse, J. P. & Kubitscheck, U. Light sheet microscopy for single molecule tracking in living tissue. *PLoS One* **5**, 1–9 (2010).
28. Rauzi, M. *et al.* Embryo-scale tissue mechanics during *Drosophila* gastrulation movements. *Nat. Commun.* **6**, 8677 (2015).
29. Krzic, U., Gunther, S., Saunders, T. E., Streichan, S. J. & Hufnagel, L. Multiview light-sheet microscope for rapid in toto imaging. *Nat. Methods* **9**, 730–733 (2012).
30. Strobl, F., Schmitz, A. & Stelzer, E. H. K. Live imaging of *Tribolium castaneum* embryonic development using light-sheet – based fluorescence microscopy.

- Nat. Protoc.* **10**, 1486–1507 (2015).
31. Huisken, J. Slicing embryos gently with laser light sheets. *BioEssays* **34**, 406–411 (2012).
  32. Bourgenot, C., Saunter, C. D., Taylor, J. M., Girkin, J. M. & Love, G. D. 3D adaptive optics in a light sheet microscope. *Opt. Express* **20**, 13252 (2012).
  33. York, A. G. *et al.* Resolution doubling in live, multicellular organisms via multifocal structured illumination microscopy. *Nat. Methods* **9**, 749–754 (2012).
  34. Jahr, W., Schmid, B., Schmied, C., Fahrbach, F. O. & Huisken, J. Hyperspectral light sheet microscopy. *Nat. Commun.* **6**, 1–7 (2015).
  35. Friedrich, M., Gan, Q., Ermolayev, V. & Harms, G. S. STED-SPIM: Stimulated emission depletion improves sheet illumination microscopy resolution. *Biophys. J.* **100**, L43–L45 (2011).
  36. Tomer, R., Lovett-barron, M., Kauvar, I., Broxton, M. & Deisseroth, K. SPED Light Sheet Microscopy : Fast Mapping of Biological System Structure and Function. *Cell* **163**, 1796–1806 (2015).
  37. Wu, Y. *et al.* Inverted selective plane illumination microscopy (iSPIM) enables coupled cell identity lineaging and neurodevelopmental imaging in *Caenorhabditis elegans*. *Proc. Natl. Acad. Sci. U. S. A.* **108**, 17708–13 (2011).
  38. Truong, T. V., Supatto, W., Koos, D. S., Choi, J. M. & Fraser, S. E. Deep and fast live imaging with two-photon scanned light-sheet microscopy. *Nat. Methods* **8**, 757–60 (2011).
  39. Bouchard, M. B. *et al.* Swept confocally-aligned planar excitation (SCAPE) microscopy for high-speed volumetric imaging of behaving organisms. *Nat. Photonics* **9**, 113–119 (2015).
  40. Keller, P. J., Schmidt, A. D., Wittbrodt, J. & Stelzer, E. H. K. Reconstruction of

- zebrafish early embryonic development by scanned light sheet microscopy. *Science* **322**, 1065–9 (2008).
41. Mickoleit, M. *et al.* High-resolution reconstruction of the beating zebrafish heart. *Nat. Methods* **11**, 1–6 (2014).
  42. Huisken, J., Swoger, J., Del Bene, F., Wittbrodt, J. & Stelzer, E. H. K. Optical sectioning deep inside live embryos by selective plane illumination microscopy. *Science* **305**, 1007–9 (2004).
  43. Huisken, J. & Stainier, D. Y. R. Even fluorescence excitation by multidirectional selective plane illumination microscopy ( mSPIM ). **32**, 2608–2610 (2007).
  44. Dupertuis, M. a., Proctor, M. & Acklin, B. Generalization of complex Snell-Descartes and Fresnel laws. *J. Opt. Soc. Am. A* **11**, 1159 (1994).
  45. Torrance, K. E., SPARROW, E. M. & Birkebak, R. C. Polarization, Directional Distribution, and Off-Specular Peak Phenomena in Light Reflected from Roughened Surfaces. *J. Opt. Soc. Am.* **56**, 916 (1966).
  46. Silvestri, L., Bria, A., Sacconi, L., Iannello, G. & Pavone, F. S. Confocal light sheet microscopy: micron-scale neuroanatomy of the entire mouse brain. *Opt. Express* **20**, 20582 (2012).
  47. Fahrbach, F. O. & Rohrbach, A. Propagation stability of self-reconstructing Bessel beams enables contrast-enhanced imaging in thick media. *Nat. Commun.* **3**, 632 (2012).
  48. Baumgart, E. & Kubitscheck, U. Scanned light sheet microscopy with confocal slit detection. *Opt. Express* **20**, 21805–21814 (2012).
  49. Medeiros, G. de *et al.* Confocal multiview light-sheet microscopy. *Nat. Commun.* **6**, 8881 (2015).
  50. Kumar, A. *et al.* Using stage- and slit-scanning to improve contrast and optical

- sectioning in dual-view. *Biol. Bull.* 26–39 (2016). doi:10.1086/689589
51. Vettenburg, T. *et al.* Light-sheet microscopy using an Airy beam. *Nat. Methods* **11**, 541–4 (2014).
  52. Fahrbach, F. O., Gurichenkov, V., Alessandri, K., Nassoy, P. & Rohrbach, A. Light-sheet microscopy in thick media using scanned Bessel beams and two-photon fluorescence excitation. *Opt. Express* **21**, 13824 (2013).
  53. Fahrbach, F. O. & Rohrbach, A. Propagation stability of self-reconstructing Bessel beams enables contrast-enhanced imaging in thick media. *Nat. Commun.* **3**, 632 (2012).
  54. Durnin, J., Miceli, J. & Eberly, J. H. Diffraction-free beams. *Phys. Rev. Lett.* **58**, 1499–1501 (1987).
  55. McGloin, D. & Dholakia, K. Bessel beams: Diffraction in a new light. *Contemp. Phys.* **46**, 15–28 (2005).
  56. Fahrbach, F. O. & Rohrbach, A. A line scanned light-sheet microscope with phase shaped self-reconstructing beams. *Opt. Express* **18**, 24229–24244 (2010).
  57. Arlt, J. & Dholakia, K. Generation of high-order Bessel beams by use of an axicon. *Opt. Commun.* **177**, 297–301 (2000).
  58. Brzobohatý, O., Cizmár, T. & Zemánek, P. High quality quasi-Bessel beam generated by round-tip axicon. *Opt. Express* **16**, 12688–12700 (2008).
  59. Gerchberg, B. R. W. & Saxton, W. O. A Practical Algorithm for the Determination of Phase from Image and Diffraction Plane Pictures. *Optik (Stuttg.)*. **35**, 237–246 (1972).
  60. Centonze, V. E. & White, J. G. Multiphoton Excitation Provides Optical Sections from Deeper within Scattering Specimens than Confocal Imaging. *Biophys. J.* **75**, 2015–24 (1998).

61. Marsh, P., Burns, D. & Girkin, J. Practical implementation of adaptive optics in multiphoton microscopy. *Opt Express* **11**, 1123–1130 (2003).
62. Benninger, R. K. P. & Piston, D. W. Two-Photon Excitation Microscopy for the Study of Living Cells and Tissues. *Curr. Protoc. Cell Biol.* **04**, Unit-4.1124 (2013).
63. HANNINEN, P. E., SOINI, E. & HELL, S. W. Continuous wave excitation two-photon fluorescence microscopy. *Journal of Microscopy* **176**, 222–225 (1994).
64. Dittrich, P. S. & Schwille, P. Photobleaching and stabilization of fluorophores used for single-molecule analysis with one- and two-photon excitation. *Appl. Phys. B Lasers Opt.* **73**, 829–837 (2001).
65. Rozbicki, E., Chuai, M. & Weijer, C. J. Technique for Liquid Culture of Early Chick Embryos Suitable for Long Term Live Imaging. 1–7 (2016).
66. Biggs, D. S. C. & Andrews, M. image restoration algorithms. (1997).
67. Wang, D., Meza, D., Wang, Y., Gao, L. & Liu, J. T. C. Sheet-scanned dual-axis confocal microscopy using Richardson–Lucy deconvolution. *Opt. Lett.* **39**, 5431 (2014).
68. Meyer, F. Topographic distance and watershed lines. *Signal Processing* **38**, 113–125 (1994).
69. Mcdole, K. *et al.* Whole-central nervous system functional imaging in larval *Drosophila*. *Nat. Commun.* **6**, 7924 (2015).
70. Optics, S. Data Sheet S4LFT0061/065. [www.silloptics.de/en/products/laser-optics/f-theta-lenses/product-overview/](http://www.silloptics.de/en/products/laser-optics/f-theta-lenses/product-overview/) (2017). doi:10.1111/j.1464-410X.1984.tb05852.x
71. Eyal-Giladi, H. & Kochav, S. From cleavage to primitive streak formation: A complementary normal table and a new look at the first stages of the development of the chick. I. General morphology. *Dev. Biol.* **49**, 321–337 (1976).



72. Eyal-Giladi, H., Kochav, S. & Ginsburg, M. From cleavage to primitive streak formation: A complementary normal table and a new look at the first stages of the development of the chick. II. Microscopic Anatomy and Cell Population Dynamics. *Dev. Biol.* **49**, 321–337 (1976).
73. Ramkumar, N. *et al.* Crumbs2 promotes cell ingression during the epithelial-to-mesenchymal transition at gastrulation. *Nat. Cell Biol.* **18**, 1281–1291 (2016).
74. Bangs, F. K., Schrode, N., Hadjantonakis, A.-K. & Anderson, K. V. Lineage specificity of primary cilia in the mouse embryo. *Nat. Cell Biol.* **17**, 113–22 (2015).
75. Smith, C. S., Joseph, N., Rieger, B. & Lidke, K. A. Fast, single-molecule localization that achieves theoretically minimum uncertainty. *Nat. Methods* **7**, 373–5 (2010).
76. Kinoshita, K., Itch, H. & Hayakawa, T. DualView Microscopy with a Single Camera: RealTime Imaging of Molecular Orientations and Calcium. **115**, 67–73 (1991).
77. Baddeley, D. *et al.* 4D Super-Resolution Microscopy with Conventional Fluorophores and Single Wavelength Excitation in Optically Thick Cells and Tissues. **6**, (2011).
78. Fischer, M., Haase, I., Simmeth, E., Gerisch, G. & Müller-Taubenberger, A. A brilliant monomeric red fluorescent protein to visualize cytoskeleton dynamics in Dictyostelium. *FEBS Lett.* **577**, 227–232 (2004).
79. Keller, P. J. & Dodt, H. U. Light sheet microscopy of living or cleared specimens. *Curr. Opin. Neurobiol.* **22**, 138–143 (2012).
80. Yang, Z. *et al.* A compact Airy beam light sheet microscope with a tilted cylindrical lens. *Biomed. Opt. Express* **5**, 3434–42 (2014).
81. Fahrbach, F. O., Simon, P. & Rohrbach, A. Microscopy with self-reconstructing beams. *Nat. Photonics* **4**, 780–785 (2010).

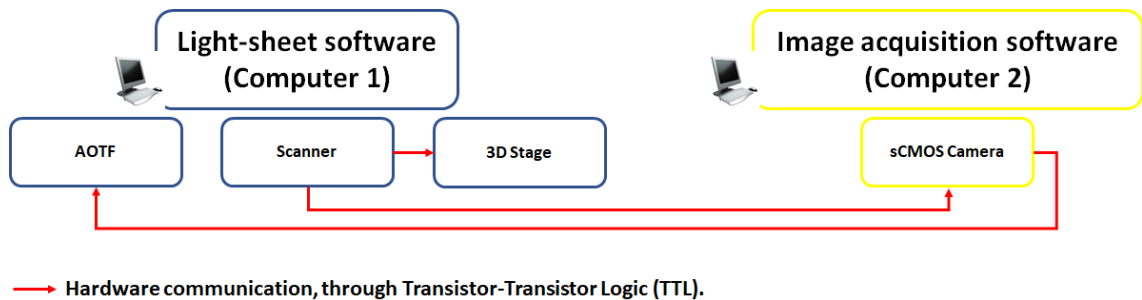
82. Mahou, P., Vermot, J., Beaufepaire, E. & Supatto, W. Multicolor two-photon light-sheet microscopy. *Nat. Methods* **11**, 600–601 (2014).
83. Schacht, P., Johnson, S. B. & Santi, P. a. Implementation of a continuous scanning procedure and a line scan camera for thin-sheet laser imaging microscopy. *Biomed. Opt. Express* **1**, 598–609 (2010).
84. Das, R. M. & Storey, K. G. Apical abscission alters cell polarity and dismantles the primary cilium during neurogenesis. *Science (80-. )*. **343**, 200–204 (2014).
85. Cizmár, T. & Dholakia, K. Tunable Bessel light modes: engineering the axial propagation. *Opt. Express* **17**, 15558–15570 (2009).
86. Planchon, T. a *et al.* Rapid three-dimensional isotropic imaging of living cells using Bessel beam plane illumination. *Nat. Methods* **8**, 417–423 (2011).
87. Olarte, O. E. *et al.* Image formation by linear and nonlinear digital scanned light-sheet fluorescence microscopy with Gaussian and Bessel beam profiles. *Biomed. Opt. Express* **3**, 1492–1505 (2012).
88. Schrader, M., Hofmann, U. G. & Hell, S. W. Ultrathin fluorescent layers for monitoring the axial resolution in confocal and two-photon fluorescence microscopy. *J. Microsc.* **191**, 135–140 (1998).
89. Chen, B.-C. *et al.* Lattice light-sheet microscopy: Imaging molecules to embryos at high spatiotemporal resolution. *Science (80-. )*. **346**, 1257998–1257998 (2014).
90. Preibisch, S. *et al.* Efficient Bayesian-based multiview deconvolution. *Nat. Methods* **11**, 645–8 (2014).
91. Wu, Y. *et al.* Spatially isotropic four-dimensional imaging with dual-view plane illumination microscopy. *Nat. Biotechnol.* **31**, 1032–8 (2013).
92. Wu, Y. *et al.* Simultaneous multiview capture and fusion improves spatial

resolution in wide-field and light-sheet microscopy. *Optica* **3**, 897 (2016).

## Appendices

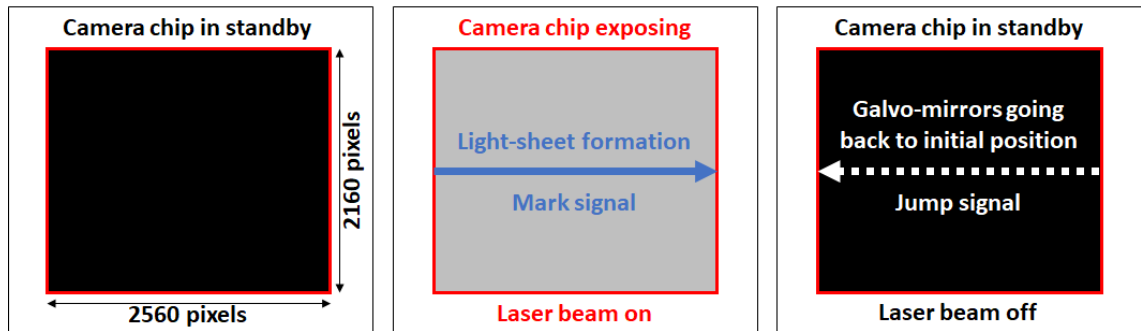
### A.1 DSLM: Light-sheet software and image software

The DSLM microscope is controlled by two custom programs that run in two independent computers, the light-sheet software and the image acquisition software. The light-sheet software controls light-sheet formation and sample positioning, through controlling the following devices: AOTF, scanner and 3D stage. The image acquisition software controls the sCMOS camera and regulates the images acquisition workflow. The following description of the software will focusses on the communication and synchronisation between both software codes and computers.

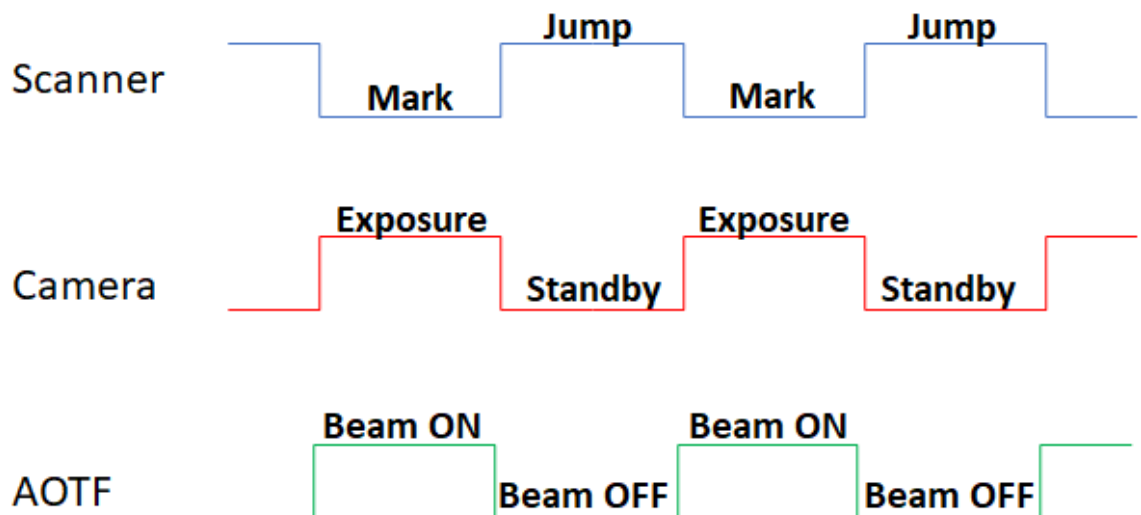


The scanner acts as the master device for hardware signalling. The scanner forms the light-sheet. The light-sheet is formed from one edge of the camera to the other, travelling along the 2560 pixels on the camera chip, during camera exposure. One complete beam scan or light-sheet formed represents one image captured. The image acquisition synchronisation is established between camera and scanner, to ensure that the images are captured and saved on the computer with correct timing. The scanner produces high and low transistor-transistor logic (TTL) signals during the galvo-mirror movements, they are named Jump and Mark respectively. During the slow scan of the galvo mirror to perform digital scanning of the light sheet, the TTL output is low and this is referred to as Mark. While the scanner is returning to the start

position the TTL output is high and this is referred to as Jump. The falling edge of the Mark TTL signal is used to trigger camera exposure and the length of the Mark signal determines the duration of the camera exposure. The Jump TTL signal brings the galvo-mirrors rapidly back to their initial position, at the same time the frame is saved on the computer.

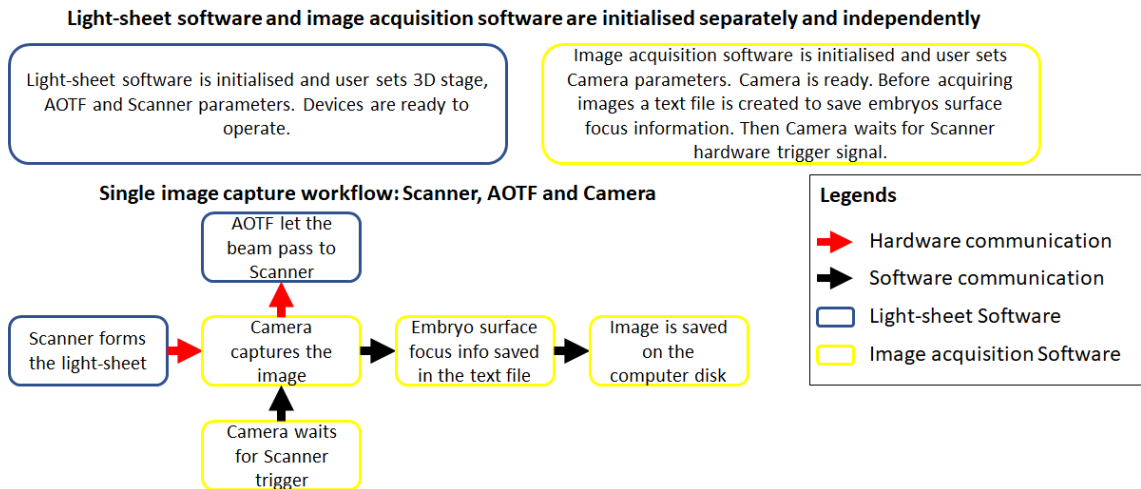


After saving the frame the camera waits for the next trigger. When the camera is exposing it sends a hardware signal to the AOTF to let the laser beam travel through the scanner to form the light-sheet. When the camera is not exposing, the AOTF deviates the beam away from the scanner, thus avoiding illumination of the sample while the galvo-mirrors are moving back to their initial position.



Note that in the image above, the Jump signal has the same duration as the Mark signal. In practice this is not true. Normally the Jump time back to the start position is shorter than the Mark time. The length of a single frame time is the sum of the lengths

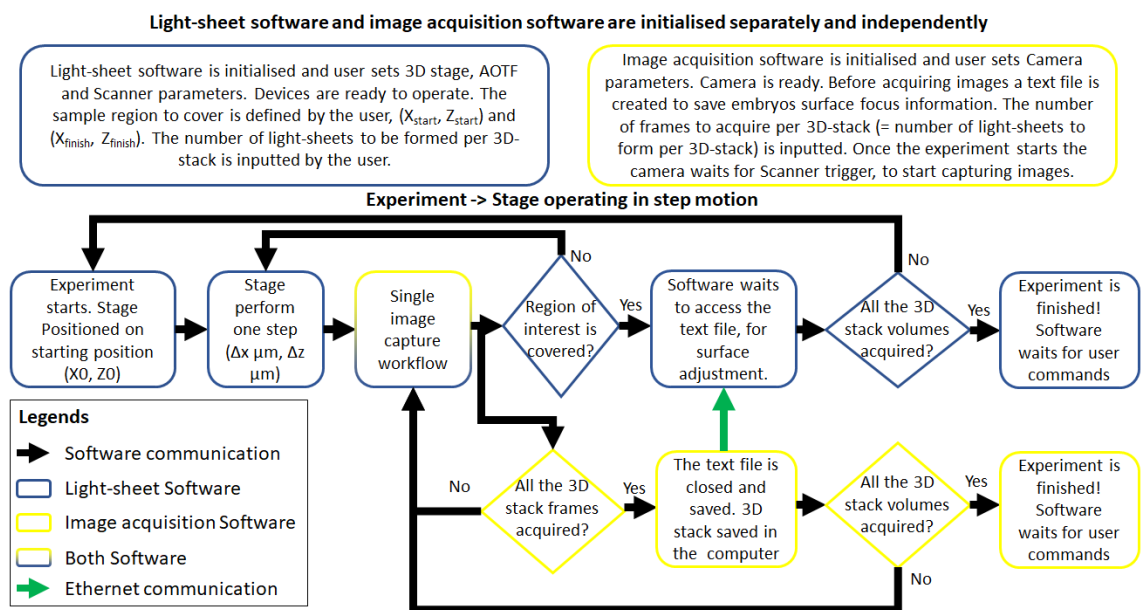
of the Mark and Jump times, determining the exact frame rate. A single image capture workflow is shown in the image below.



The number of frames to form a single 3D stack is equal to the number of light-sheets formed by the scanner. Before starting the experiment, the number of frames and the precise instructions for control of the galvo mirrors are compiled and uploaded into the scanner control card. At the start of the experiment the software code starts after a software command. With the stage operating in continuous mode, the first light-sheet Mark TTL signal triggers the stage to start moving, covering the sample region of interest with constant velocity, thus ensuring that all the images are acquired with equal spatial and temporal distance. After acquiring all the images, the image acquisition software saves all the frames acquired into a single 3D stack in the computer. For a 20 hour image acquisition experiment around 500-600 individual 3D stacks are acquired.

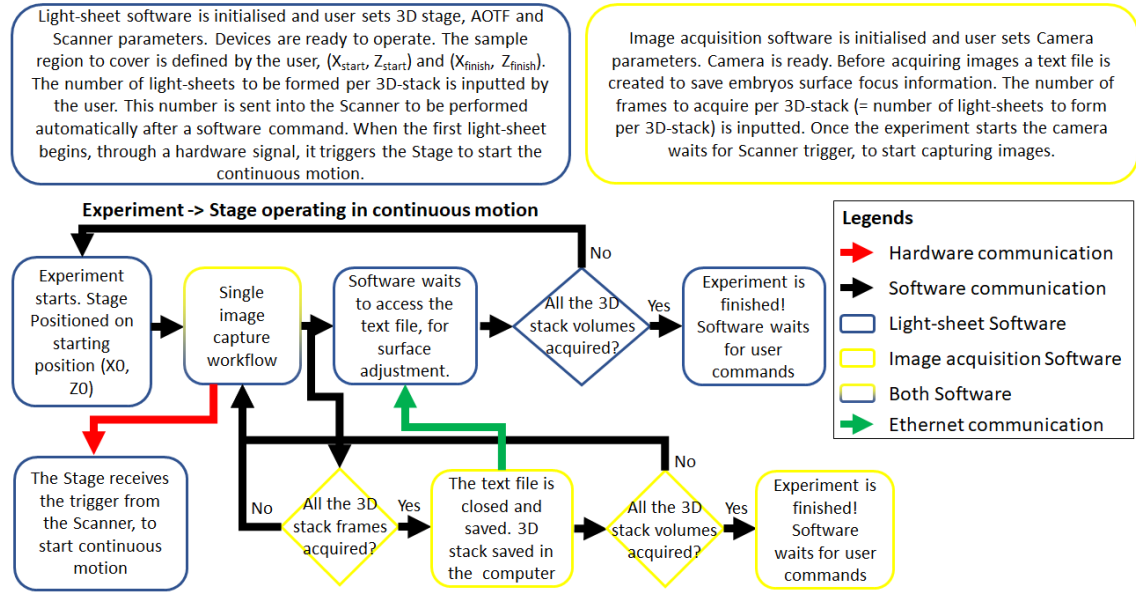
The synchronisation of the light-sheet and acquisition software is made through access of the stage height correction text file. This text file is created by the image acquisition software and after acquiring a complete 3D stack this file is saved and closed. Closing the file makes it now accessible to the light-sheet software through an ethernet connection. Then the image acquisition software waits for a new trigger from

the scanner to start a new 3D stack acquisition. The light-sheet software uses the data stored in the text file to convert into new coordinates for the stage to position the embryo surface in focus, as described in section 3.1 and in more detail in appendix A.2. After updating the new coordinates, the light-sheet software is ready to start a new 3D stack acquisition. The stage moves back to the initial position. Then to start a new 3D stack acquisition, the scanner sends a new trigger to the camera and the stage. This implies that the image acquisition software always waits for the light-sheet software to begin a new 3D stack acquisition. The image below shows the workflow associated with the acquisition of individual 3D stacks, with the stage operating in step by step motion.



The next diagram illustrates the workflow associated with the acquisition of individual 3D stacks, with the stage operating in continuous motion mode.

### Light-sheet software and image acquisition software are initialised separately and independently



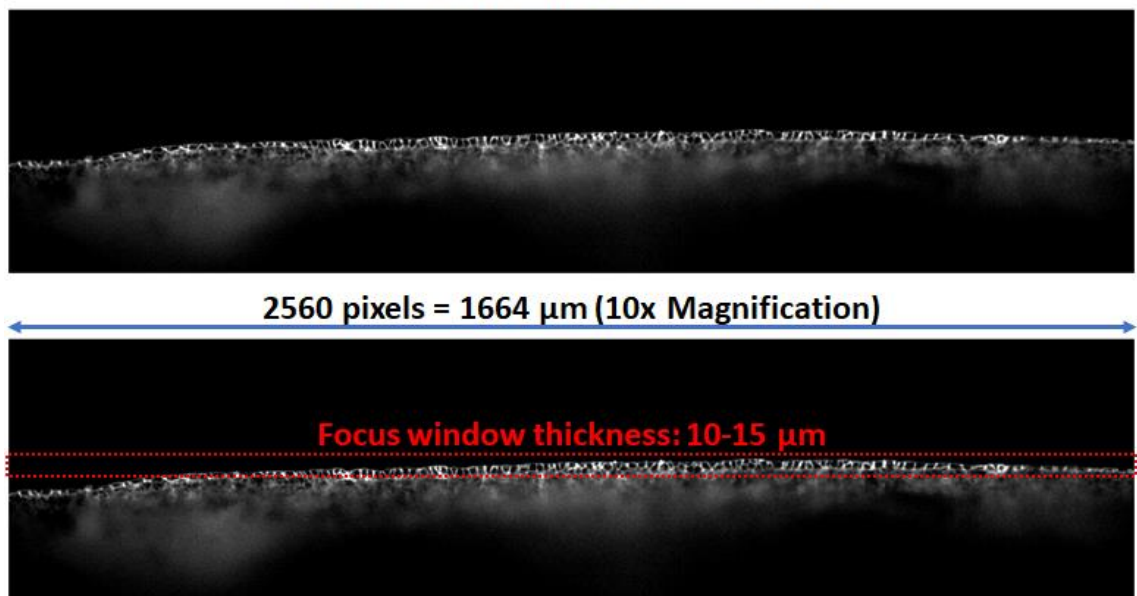
The user of the light-sheet software can set the time lapse interval between 3D stacks. This command only works if the interval time is longer than the time it takes to acquire the 3D stack plus the time it takes to update the new 3D stage coordinates and save the data to disk. In the event the interval is shorter than the time required to perform one acquisition cycle, the next 3D stack acquisition starts once the new coordinates to position the embryo surface are updated by the light-sheet software.



## A.2 DSLM: Sample position compensation to maintain in focus

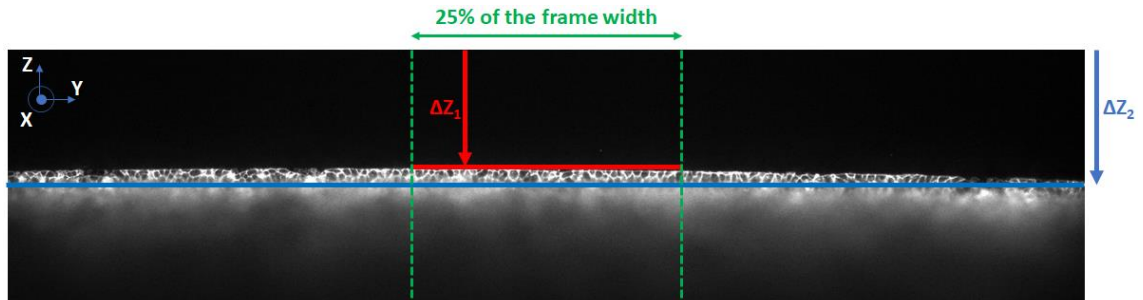
As explained in section 3.1, during the 3D stack images acquisition an algorithm is executed to keep the embryo surface inside the focus window located at the middle of the image. The light-sheet focus is set to be located at the middle of the acquired image. In the example shown below the focus window has a range of 10-15  $\mu\text{m}$  and ensures the best resolution and high contrast cross-section images at the embryo surface first layer.

**Cross-section image of a chick embryo**



As outlined in appendix A.1, the DSLM microscope is controlled by two computers. The light-sheet software controls the light-sheet formation and sample positioning. The image acquisition software, controls all the images processing, acquisition and storage. The image acquisition software calculates and stores in a text file the difference, in pixels, between the position of the embryo surface and the middle of the frame. The position of the embryo's surface is calculated in a central region consisting of 25% of the frame width centred around the middle of the frame. Within this region the algorithm averages intensity values in each pixel row from top to

bottom and identifies the row with the highest grey value variance of light intensity. This row will correspond to the embryo surface top layer. The difference in pixels between this row and the pixel row sitting in the centre of the frame dictates the adjustment required to bring the sample into the focus.



$\Delta Z_1$  -> line of pixels coincident with the embryos surface

$\Delta Z_2$  -> line of pixels in the middle of the frame

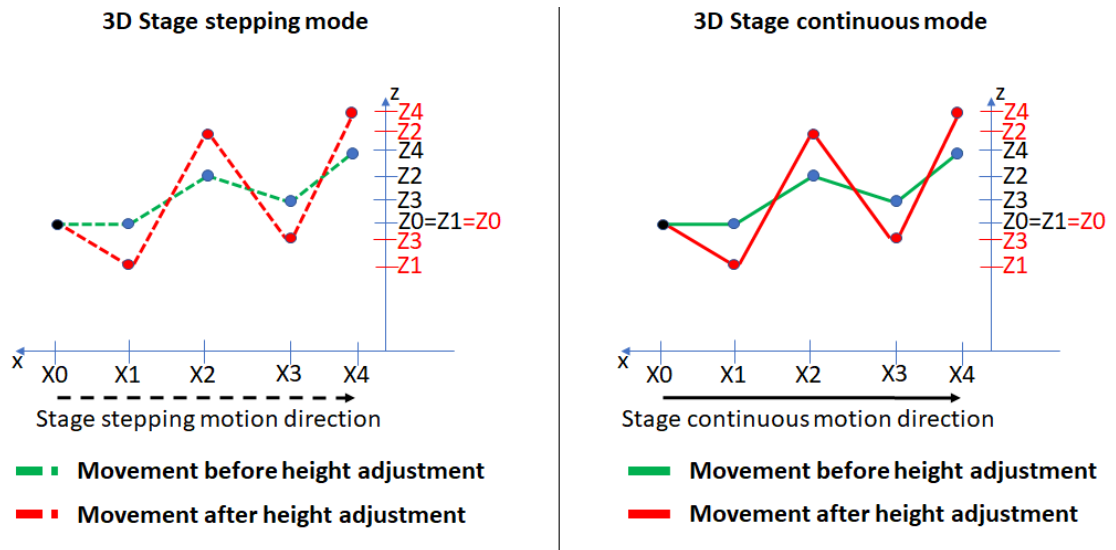
$\Delta Z_2 - \Delta Z_1$  = distance in pixels that need to be adjusted, bringing the embryos surface to the middle of the frame

During a 3D stack acquisition, the text file is opened and inaccessible for the light-sheet software. Once the complete set of images making up the 3D stack is acquired the text file is closed and saved by the image acquisition software. Through an ethernet connection linking the two computers controlling the microscope, the text file becomes accessible by the light-sheet software. The light-sheet software converts the distances from pixels into  $\mu\text{m}$  and this information is used to adjust the Z axis position during the next scan, thus ensuring that the embryo will be in or close to focus during the next 3D stack acquisition.

The height adjustment is made through an interpolation between five positions along the embryo. Since the embryo is uneven during development some regions of the surface are at different Z positions than others. To ensure all the embryo surface is captured an interpolation is made between the selected five positions, for adjusting the Z position of the embryo surface to keep it always in focus. Note that during development the embryo surface oscillate between ups and downs, along Z axis, as represented in graphs illustrated below. For instance, a certain region of the embryo

can be initially in a high Z position and after few hours can come to a lower Z position.

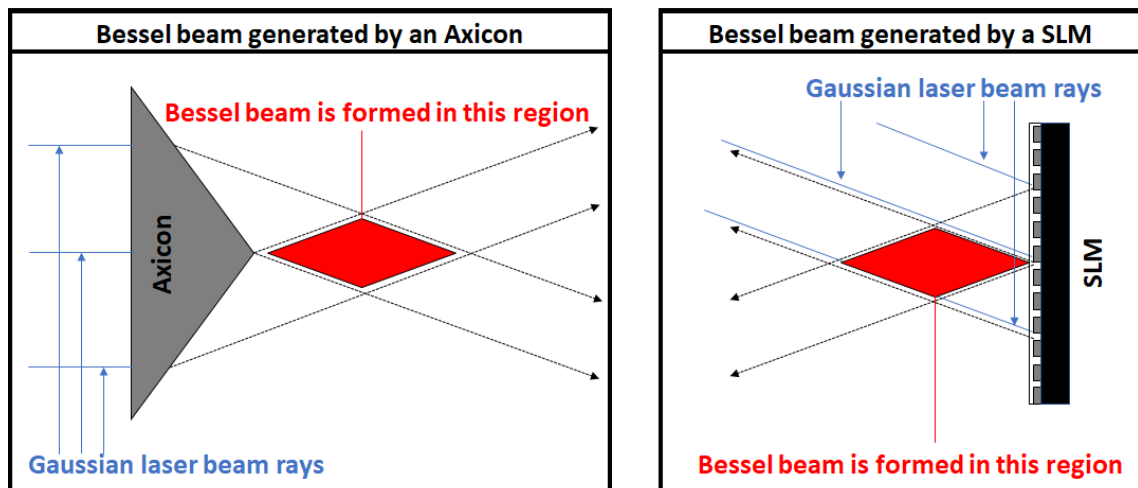
These five positions for interpolation are defined in the XZ plane.



In the plots illustrated above, the height adjustment occurring for the 3D stage stepping and continuous modes is shown. The coordinates are always kept the same for the X axis, while in the Z axis, due to embryo surface undulations, are adjusted to maintain the embryo surface in focus. The black dot indicates the X0 and Z0 starting coordinates for the first 3D stack acquired (in addition the Z0 can be adjusted). In the graph above, the dots mark the five positions marked along the embryo, while the dashed and filled lines show the stage motion. In the Z axis the black Z0, Z1, Z2, Z3 and Z4 and the blue dots are the height positions before height adjustment, while the red dots and Z0, Z1, Z2, Z3 and Z4 are the new height positions after adjustment, updated for the next 3D stack acquisition. The lines in green and red presented on the plots above represent the embryo surface profile before and after height adjustment, respectively.

### A.3 Bessel beam generated with an SLM

Bessel beams can be generated through Gaussian beam modulation. Two ways to perform this modulation are the use of an axicon or a Spatial Light Modulator (SLM). In the present case a SLM is used most importantly due to its flexibility in forming Bessel beams with the chance of changing some of the modulation parameters which cannot be done with one axicon. The SLM is slightly tilted in relation to the Gaussian laser beam rays, between 10-20° angle, so as to not send the beam back to the source, thus avoiding more complex set-ups involving beam splitters.



The SLM is a device that contains a liquid crystal display used to modulate light. The SLM used in this project comprises 512\*512 pixels in a chip with a dielectric coating, working within the 450-600 nm wavelength range. The SLM can modulate the light phase, intensity or both. In the present case, to generate the Bessel beam the SLM modulates the laser beam incident light by applying a conical phase mask to it.

The SLM treats and outputs the incident light with two inseparable contributions: diffraction and resulting pixels hologram. The incident light falls on the 2D matrix of pixels each with coordinate  $(x, y)$ . The SLM hologram is programmed with a phase shift described by

$$\text{Hologram}(x, y) = e^{i\theta(x,y)} + C .$$

With  $(x, y)$  indicating the pixel position on the pixels matrix,  $\theta(x, y)$  indicates the phase shift and  $C$  is a constant offset.

In the far field, the rays that originate the Bessel beams form a ring and the unmodulated light creates a bright spot in the middle of the ring. In order to separate the ring from the unmodulated light, a linear phase ramp is added to the hologram as follows,

$$\theta(x, y) = \overbrace{a\sqrt{x^2 + y^2}}^{\text{Conical term}} + \underbrace{bx}_{\text{Linear shift term}}$$

The undesired SLM diffraction orders and unmodulated light are then spatially separated and blocked with a pinhole as illustrated by the microscope set-up in Figure 5.1, in section 5.1 of this document.